

## A NEW SAMPLE OF OBSCURED AGNS SELECTED FROM THE XMM-NEWTON AND AKARI SURVEYS

YUICHI TERASHIMA<sup>1</sup>, YOSHITAKA HIRATA<sup>1</sup>, HISAMITSU AWAKI<sup>1</sup>, SHINKI OYABU<sup>2</sup>, POSHAK GANDHI<sup>3</sup>,  
YOSHIKI TOBA<sup>4</sup>, AND HIDEO MATSUHARA<sup>5</sup>

*Accepted for publication in the Astrophysical Journal*

### ABSTRACT

We report a new sample of obscured active galactic nuclei (AGNs) selected from the *XMM-Newton* serendipitous source and *AKARI* point-source catalogs. We match X-ray sources with infrared (18 and 90  $\mu\text{m}$ ) sources located at  $|b| > 10^\circ$  to create a sample consisting of 173 objects. Their optical classifications and absorption column densities measured by X-ray spectra are compiled and study efficient selection criteria to find obscured AGNs. We apply the criteria (1) X-ray hardness ratio defined by using the 2 – 4.5 keV and 4.5 – 12 keV bands  $> -0.1$  and (2) EPIC-PN count rate (CR) in the 0.2 – 12 keV to infrared flux ratio  $\text{CR}/F_{90} < 0.1$  or  $\text{CR}/F_{18} < 1$ , where  $F_{18}$  and  $F_{90}$  are infrared fluxes at 18 and 90  $\mu\text{m}$  in Jy, respectively, to search for obscured AGNs. X-ray spectra of 48 candidates, for which no X-ray results have been published, are analyzed and X-ray evidence for the presence of obscured AGNs such as a convex shape X-ray spectrum indicative of absorption of  $N_{\text{H}} \sim 10^{22-24} \text{ cm}^{-2}$ , a very flat continuum, or a strong Fe-K emission line with an equivalent width of  $> 700 \text{ eV}$  is found in 26 objects. Six among them are classified as Compton-thick AGNs, and four are represented by either Compton-thin or Compton-thick spectral models. The success rate of finding obscured AGNs combining our analysis and the literature is 92% if the 18  $\mu\text{m}$  condition is used. Of the 26 objects, 4 are optically classified as an H II nucleus and are new “elusive AGNs” in which star formation activity likely overwhelms AGN emission in the optical and infrared bands.

*Keywords:* galaxies: active, infrared: galaxies, X-rays: galaxies

### 1. INTRODUCTION

Multiwavelength observations have been finding various populations of active galactic nuclei (AGN). The population of obscured AGNs, which constitute a large fraction of AGNs (e.g., Fabian 2004, Gilli et al. 2007), among various classes, are believed to be important in various aspects including the origin of the Cosmic X-ray background (XRB; e.g., Gilli et al. 2007), connection between obscuring matter and star formation activity in the host galaxies (e.g., Wada & Norman 2002), and evolutionary paths of AGNs (e.g., Sanders et al., 1988, Hopkins et al. 2006, Alexander & Hickox 2012). Modern large area surveys at various wavebands are indeed utilized to find a large number of hidden AGNs and to elucidate their nature.

Obscured AGNs are found by X-ray emission transmitted through obscuring matter, optical line emission from extended and ionized regions, infrared emission from dust heated by central AGNs, and so on. Hard X-ray surveys are one effective way to find obscured AGNs because the photoelectric cross section decreases as X-ray energy increases, and transmitted X-rays can be observed. Indeed, more than a dozen of Compton-thick AGNs, which are absorbed by a hydrogen column density greater than  $1.5 \times 10^{24} \text{ cm}^{-2}$ , show transmitted hard X-rays above

10 keV (Comastri 2004 and references therein; Burlon et al. 2011). The all-sky and sensitive hard X-ray surveys conducted by the *Swift* Burst Alert Telescope (BAT) and *INTEGRAL* provide an unprecedented opportunity to search for the heavily absorbed population. While obscured AGNs have been found in these surveys, the number of Compton-thick sources are not as many as expected from other studies using, e.g., optical emission-line-selected samples (Gilli et al. 2007) or prediction from the synthesis models of the XRB (Burlon et al. 2011). This bias is due to the attenuation of X-rays even at energies above 10 keV for Compton-thick cases (Wilman & Fabian 1999, Ikeda et al. 2009, Murphy & Yaqoob 2009, Brightman & Nandra 2011a). Burlon et al. (2011) estimated a correction factor of about four for Compton-thick fraction in their *Swift*/BAT sample. Thus, hard X-rays are still biased against heavily absorbed AGNs.

Infrared emission from warm dust heated by the central source is also employed to find obscured AGNs. Mid-infrared (MIR) emission indeed traces the power of the AGNs regardless of whether they are type 1 or 2, and the attenuation of MIR in type 2 AGNs is not large (Horst et al. 2008, Gandhi et al. 2009, Ichikawa et al. 2012, Matsuta et al. 2012). A weakness of utilizing infrared emission, however, is that emission from dust heated by stars cannot be separated if spatial resolution is not sufficiently high, and therefore the infrared-selected sample contains non-negligible fraction of non-AGN galaxies. For example, 13 and 18 out of 126 galaxies selected at 12  $\mu\text{m}$  are optically classified as H II and H II/AGN composite galaxies, respectively (Brightman & Nandra 2011b).

The combination of X-ray and infrared selection is a useful way to select a heavily obscured AGN population

<sup>1</sup> Department of Physics, Ehime University, Bunkyo-cho, Matsuyama, Ehime 790-8577, Japan

<sup>2</sup> Department of Physics, Nagoya University, Furo-cho, Chikusa-ku, Nagoya, Aichi 464-8602, Japan

<sup>3</sup> School of Physics & Astronomy, University of Southampton, Highfield, Southampton, SO17 1BJ, UK

<sup>4</sup> Research Center for Space and Cosmic Evolution, Ehime University, Bunkyo-cho, Matsuyama, Ehime 790-8577, Japan

<sup>5</sup> Institute of Space and Astronautical Science, 3-1-1 Yoshinodai, Chuo-ku, Sagami-hara, Kanagawa 252-5210, Japan

and is applied to deep (Fiore et al. 2008, 2009) or wide surveys (Mateos et al. 2012, Severgnini et al. 2012, Rovilos et al. 2014) to overcome the biases in the selections using only hard X-ray or infrared emission. The X-ray to infrared flux ratios, X-ray hardness, infrared colors, and so on are utilized in these selections. Among the techniques employed, we extend the method used by Severgnini et al. (2012). They used 25  $\mu\text{m}$  fluxes ( $F_{25}$ ) measured in the *IRAS* Point Source Catalog (PSC) and X-ray data taken from the *XMM-Newton* serendipitous source catalog (2XMM catalog; Watson et al. 2009) and made a diagnostic plot of X-ray hardness ratio (HR4) and X-ray to infrared flux ratio ( $F(2-12 \text{ keV})/\nu_{25}F_{25}$ ), where HR4 is defined by using X-ray count rates (CRs) in 2–4.5 keV CR(2–4.5 keV) and in 4.5–12 keV CR(4.5–12 keV) as

$$\text{HR4} = \frac{\text{CR}(4.5 - 12 \text{ keV}) - \text{CR}(2.0 - 4.5 \text{ keV})}{\text{CR}(4.5 - 12 \text{ keV}) + \text{CR}(2.0 - 4.5 \text{ keV})}.$$

They defined the region for candidates of Compton-thick AGNs as  $F(2-12\text{keV})/\nu_{25}F_{25} < 0.02$  and  $\text{HR4} > -0.2$ , and built a sample consisting of 43 candidates. For absorbed sources, the X-ray to infrared ratio becomes small since X-rays below 12 keV are attenuated by photoelectric absorption. Absorbed sources show flatter X-ray spectra and therefore larger values of hardness ratios are expected. Thus, their criteria are expected to work to select heavily absorbed sources. About 84% of the objects in their sample are confirmed as Compton-thick AGNs and 20% are newly discovered ones. Thus, the combination of wide field survey data in the infrared and X-ray bands is promising in the search for heavily obscured AGNs.

In this paper, we combine the infrared all-sky survey data obtained with *AKARI* (Murakami et al. 2007) and the 2XMM catalog. We construct diagnostic diagrams to classify activity in galaxies and to search for obscured AGNs. We selected 48 candidates for obscured AGNs and analyzed their X-ray spectra. This paper is organized as follows. Section 2 describes the selection method of X-ray and infrared sources. Diagnostic diagrams to classify the selected sources are presented in Section 3. Results of X-ray spectral analysis are shown in section 4. Section 5 discusses the results and summaries are given in Section 6. We adopt  $H_0 = 70 \text{ km s}^{-1}$ ,  $\Omega_M = 0.3$ , and  $\Omega_\Lambda = 0.7$  throughout this paper.

## 2. THE SAMPLE

### 2.1. *XMM-Newton* and *AKARI* catalogs

We combine two large area survey data in the X-ray and infrared bands. We used the *XMM-Newton* Serendipitous source catalog Data Release 3 (2XMMi-DR3), which contains 262902 unique X-ray sources. The median X-ray flux in 0.2–12 keV is  $2.5 \times 10^{-14} \text{ erg s}^{-1}\text{cm}^{-2}$ . The typical positional uncertainty is  $1.1''$  ( $1\sigma$ ) (Watson et al. 2009). The entries listed in this catalog (CRs in 0.2–12 keV and HR4) are used to create diagnostic diagrams and select candidates for obscured AGNs. The data from EPIC-PN, which has a larger effective area than those of EPIC-MOS, was used throughout the analysis. We use sources located at the Galactic latitude  $|b| > 10^\circ$  in 2902 observations with usable PN data. Among these observations, 2686 and 216 observations

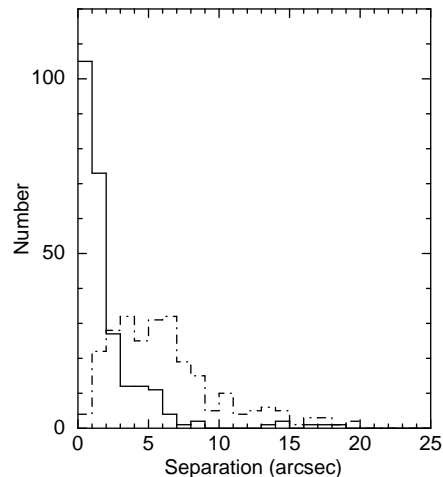


**Figure 1.** Distribution of the separation between the X-ray and infrared positions. Solid line: 18  $\mu\text{m}$  sources. Dotted-dashed line: 90  $\mu\text{m}$  sources.

are taken with full window and large window modes, respectively. There are 2062 and 139 unique fields taken with the full window and large window modes, respectively. The total number of unique EPIC-PN sources at  $|b| > 10^\circ$  is 150799. In the following analysis, sources with EPIC-PN counts in 0.2–12 keV greater than 60 counts (60851 unique sources) are used.

*AKARI* Point Source Catalogs (PSCs) were used as infrared data. *AKARI* surveyed most of the sky with the two instruments, the Infrared Camera (IRC; Onaka et al. 2007, Ishihara et al. 2010) and the Far-Infrared Surveyor (FIS; Kawada et al. 2007). The bandpasses of the IRC are centered at 9 and 18  $\mu\text{m}$ , while the band centers of the FIS are 65, 90, 140, and 160  $\mu\text{m}$ . We used 18 and 90  $\mu\text{m}$  measurements as mid- and far-infrared data. The 18  $\mu\text{m}$  is chosen to avoid silicate features, which may affect continuum measurements, in the 9  $\mu\text{m}$  bandpass of the IRC. The 90  $\mu\text{m}$  band is used among the far-infrared bands because this band is most sensitive. We use only data with the quality flag of FQUAL = 3, which means flux measurements are most reliable (Yamamura et al. 2010). There are 43865 (18  $\mu\text{m}$ ) and 62326 (90  $\mu\text{m}$ ) sources with FQUAL = 3 located at  $|b| > 10^\circ$ .

### 2.2. Cross Correlation of the X-ray and Infrared Catalogs

We compared the positions of X-ray sources in the 2XMM-DR3 and infrared sources in the *AKARI* PSCs and made a list of X-ray and infrared sources. We first listed FIS sources within  $20''$  of the X-ray source positions. If there are multiple sources within the circular region around an X-ray source, the source closest to the X-ray position is assumed to be a counterpart and is used in the following analysis. If one source is observed more than twice with *XMM-Newton*, only the data with the largest number of counts in 0.2–12 keV is used. We then matched the IRC and X-ray sources in a similar way using a matching radius of  $10''$ . Finally, the FIS and IRC source lists are combined. The combined list contains 253 sources. The histograms of the separation between the X-ray and infrared positions are shown in Figure 1 for the 18 and 90  $\mu\text{m}$  sources. The separations for the 18  $\mu\text{m}$  sources are more concentrated within a small ra-

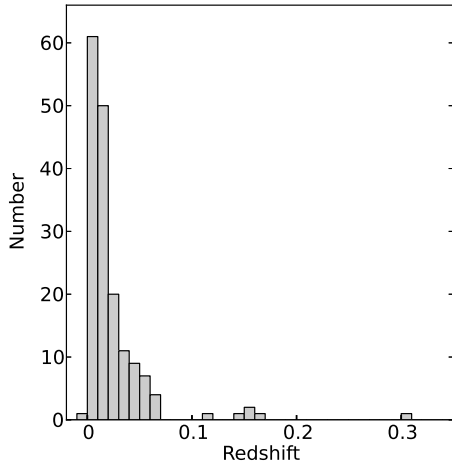


**Figure 2.** Distribution of redshifts for the matched sample using X-ray, 18, and 90  $\mu\text{m}$  data shown in Table 1.

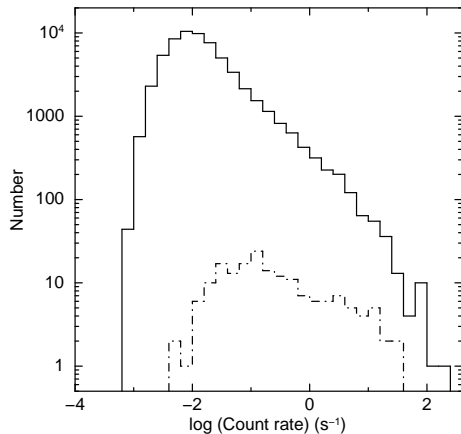


**Figure 3.** Distribution of X-ray count rates in 0.2–12 keV. Solid line: all the EPIC-PN sources located at  $|b| > 10^\circ$  with 0.2–12 keV counts greater than 60. Dotted-dashed line: 173 objects in our sample after matching with the 18  $\mu\text{m}$  and 90  $\mu\text{m}$  sources and excluding Galactic and ultraluminous X-ray sources.

dus from the X-ray positions compared to the 90  $\mu\text{m}$  sources as expected from the positional accuracy of the IRC and FIS sources ( $3\sigma \approx 6''$  and  $18''$ , respectively, for faint sources).

We searched for the most probable counterpart of the X-ray sources using the NASA/IPAC Extragalactic Database (NED) and SIMBAD Astronomical Database. Stars, H II regions, planetary nebulae, young stellar objects, and ultraluminous X-ray sources are excluded from the sample, resulting in 173 objects. The sample thus obtained is summarized in Table 1, where the *XMM* source name, alternative name, redshift, infrared flux densities, X-ray CRs in 0.2–12 keV, and hardness ratios (HR4) are shown. Redshifts are available for 171 of the 173 sources. Their distribution is shown in Figure 2 as a histogram. The distribution of X-ray CRs in 0.2–12 keV for all the EPIC-PN sources located at  $|b| > 10^\circ$  with 0.2–12 keV counts greater than 60 and the 171 objects in our sample is shown in Figure 3. Comparison of these histograms indicates that X-ray brighter objects tend to

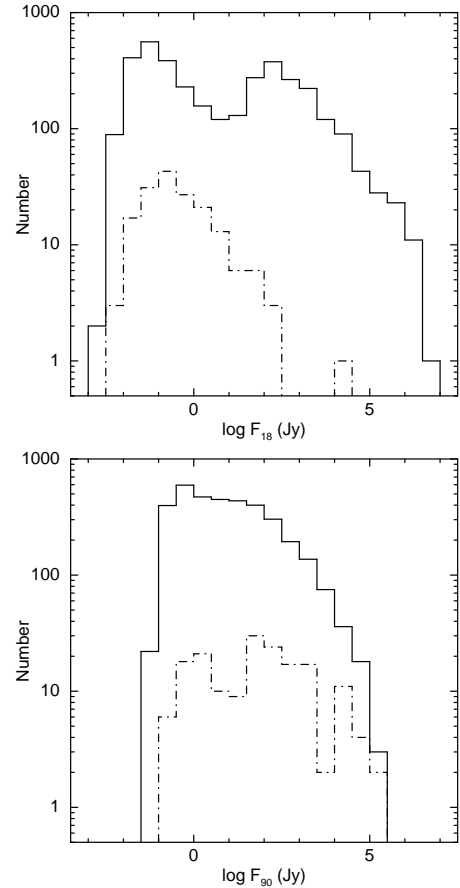


**Figure 4.** (Upper) Distribution of 18  $\mu\text{m}$  flux densities. (Lower) Distribution of 90  $\mu\text{m}$  flux densities. Solid line: nearest neighbor 18  $\mu\text{m}$  sources to 90  $\mu\text{m}$  sources within  $20''$  located at  $|b| > 10^\circ$ . Dotted-dashed line: 173 objects in our sample after matching with the X-ray sources and excluding the Galactic and ultraluminous X-ray sources.

have a possible infrared counterpart detected both in the 18 and 90  $\mu\text{m}$  bands. None of X-ray sources fainter than 0.004 counts  $\text{s}^{-1}$  in 0.2–12 keV are matched with infrared sources. We also compared distributions of infrared flux densities. The solid histograms in Figure 4 are distributions of infrared flux densities for 90  $\mu\text{m}$  sources having 18  $\mu\text{m}$  source(s) within  $20''$  and their nearest neighbor 18  $\mu\text{m}$  sources (3535 objects in total) located at  $|b| > 10^\circ$  with  $\text{FQUAL} = 3$ . The dotted-dashed histograms are those for the 173 objects matched with EPIC-PN sources. A clear difference before and after matching with X-ray sources is shown as the double peak structure in the histogram for the 18  $\mu\text{m}$  sources. The peak at a higher infrared flux density is likely to be composed of Galactic sources because the peak is more enhanced if we use objects at low Galactic longitude (e.g.,  $10^\circ < b < 15^\circ$ ) and because the peak disappeared after excluding Galactic sources in our selection procedure. The distribution of 90  $\mu\text{m}$  fluxes for X-ray-matched objects are flatter than that for all the 90  $\mu\text{m}$  sources with nearby 18  $\mu\text{m}$  sources. This fact indicates that objects brighter at 90  $\mu\text{m}$  tend to have a greater probability of being matched with an X-ray source.

We summarize the X-ray and infrared luminosities for the X-ray-IR matched sample in Table 2. The distribu-

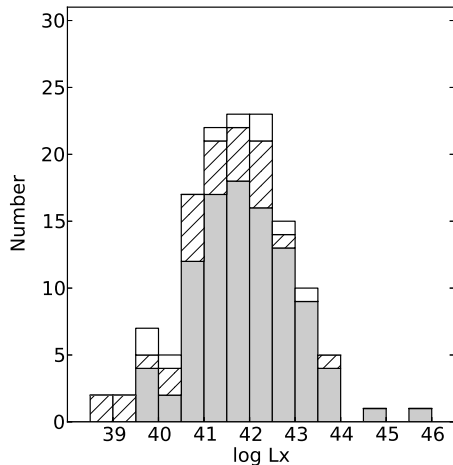


**Figure 5.** Distribution of observed X-ray luminosities in the 2–10 keV band for objects showing AGN activity for the matched sample using X-ray, 18, and 90  $\mu\text{m}$  data shown in Table 1 (shaded histogram), the 90  $\mu\text{m}$  sample (hatched histogram), and the 18  $\mu\text{m}$  (open histogram) sample.

tion of the luminosities are shown in Figures 5 and 6 as shaded histograms. Distances to nearby objects with a redshift parameter smaller than 0.003 are taken from the literature shown in Table 2, except for Mrk 59 for which a redshift-independent distance is not available. Distances to objects at  $z > 0.003$  and Mrk 59 are calculated from source redshifts and the assumed cosmology. Observed X-ray luminosities in the 2–10 keV band (source rest frame) are obtained from the literature or our analysis presented in section 4 if X-ray spectra clearly show the presence of an AGN. Most X-ray fluxes or luminosities are taken from the literature, like for absorption column densities. References are given in Table 2 only if a reference different from that for  $N_{\text{H}}$  is used. When we use published fluxes in 2–10 keV to calculate luminosities, we made a simple  $K$ -correction by assuming a simple power law with a photon index of 1.8. Since most of the objects in our samples are at a low redshift ( $z < \sim 0.3$ ), the assumption on the spectral shape only slightly affects the correction. If a photon index of 1.4 is assumed instead, the luminosity would be lower by 10% at  $z = 0.3$ . This amount is much smaller for lower redshift sources. In some cases, we obtained observed luminosities from the literature and converted them to our assumed cosmology. Infrared luminosities ( $\nu L_{\nu}$  for 18 and/or 90  $\mu\text{m}$ ) are calculated from the *AKARI* measurement of infrared fluxes. We applied a  $K$ -correction by assuming a template spectral energy distribution for Seyfert 2s by Poletta et al. (2007). Again, because of low redshifts for our sample, the amount of the correction is relatively small. A correction factor is at most about 10% for a 18  $\mu\text{m}$  luminosity at  $z = 0.3$ .

We compiled optical classifications from the literature or spectra in the archives. The sources are classified into Seyfert, Low-Ionization Nuclear Emission line Region (LINER), H II nucleus, transition between LINER and H II, BL Lac object, or normal galaxy. Seyfert, LINER, H II, and, transition objects are defined based on the location of the optical emission line ratios ( $[\text{N II}]\lambda 6584/\text{H}\alpha$ ,

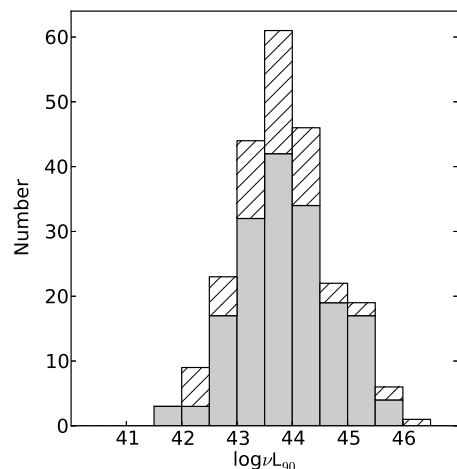
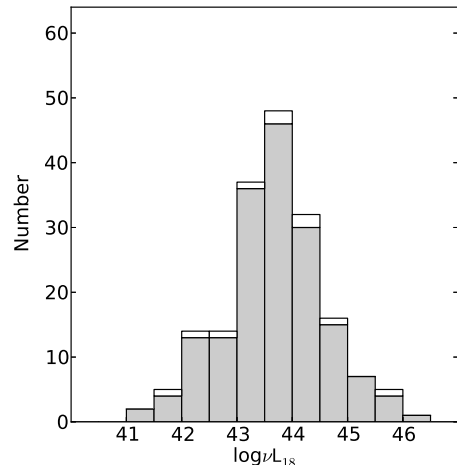


**Figure 6.** Distribution of infrared luminosities  $\nu L_{\nu}$  at 18  $\mu\text{m}$  (upper) and 90  $\mu\text{m}$  (lower) for the matched sample using X-ray, 18, and 90  $\mu\text{m}$  data shown in Table 1 (shaded histogram), the 90  $\mu\text{m}$  sample (hatched histogram), and the 18  $\mu\text{m}$  (open histogram) samples.

$[\text{S II}]\lambda\lambda 6716, 6730/\text{H}\alpha$ , and  $[\text{O III}]\lambda 5007/\text{H}\beta$ ) on the excitation diagrams. Among various definitions of the boundary among the classes (Baldwin et al. 1981, Veilleux & Osterbrock 1987, Ho et al. 1997, Kewley et al. 2006) we adopted criteria of Ho et al. (1997) because many objects in our sample are contained in the Ho et al. sample in which stellar absorption lines were carefully treated in measuring emission line fluxes. Some objects are in the boundary region of two activity classes on the excitation diagrams, or use of different emission lines results in different classifications. For such ambiguous cases, both activity classes are shown such as Seyfert/LINER. The types (1, 1.2, 1.5, 1.8, 1.9, and 2) of Seyferts, LINERs, and transition objects are also shown if available in the literature. The classifications for some objects are not published in the literature, and we classified their optical spectra from the archives of the Sloan Digital Sky Survey, the 6dF Galaxy survey, or the Updated Zwicky Catalog (Falco et al. 1999), if available. If optical spectra show only absorption lines, they are classified as a normal galaxy. No classifications are available

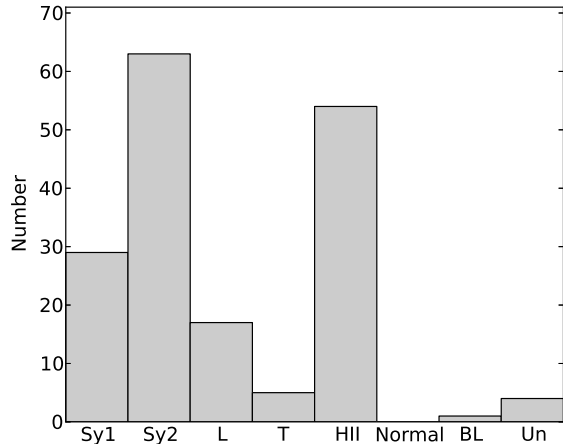


**Figure 7.** Summary of optical classifications for the matched sample using X-ray, 18, and 90  $\mu\text{m}$  data shown in Table 1. Sy1: Seyfert 1, 1.2, and 1.5; Sy2: Seyfert 1.8, 1.9, and 2; L: LINER; T: transition object between LINER and HII nucleus; HII: HII nucleus; Normal: normal galaxy; BL: BL Lac object; Un: Unclassified.

for some of the objects in the sample. They are denoted as “unclassified.” These classifications are shown in Table 1 and summarized as histograms in Figure 7. In the histograms, Seyfert 1, 1.2, and 1.5 are treated as “Seyfert 1”, while Seyfert 1.8, 1.9, and 2 are regarded as “Seyfert 2.”

Since one of our aims is to search for obscured AGNs, we compiled absorption column densities ( $N_{\text{H}}$ ) measured using X-ray spectra from the literature, as shown in Table 1.  $N_{\text{H}}$  values are shown for Seyferts and LINERs in which X-ray emission is dominated by AGNs. Some galactic nuclei classified as H II show evidence for the presence of an AGN. Their  $N_{\text{H}}$  values are also shown. If there are multiple published results, we put priority on the results of systematic analysis of a large sample, and results based on better quality of data. For objects showing a signature of heavy absorption exceeding  $\sim 10^{24} \text{ cm}^{-2}$ , we use results based on wide-band spectra covering hard X-rays above 10 keV whenever possible. Objects showing a strong Fe-K emission line with an equivalent width (EW) exceeding 700 eV and/or a very flat spectral slope are regarded as  $N_{\text{H}} > 10^{24} \text{ cm}^{-2}$  even if only X-ray spectra below 10 keV are available. The boundary of the EW (700 eV) was chosen based on analysis of X-ray spectra for a large sample of AGNs (Guainazzi et al. 2005a; Fukazawa et al. 2011) and theoretical predictions (Awaki et al. 1991; Leahy & Creighton 1993; Ghisellini et al. 1994; Ikeda et al. 2009; Murphy & Yaqoob 2009; Brightman, & Nandra 2011a). If an  $N_{\text{H}}$  value is not explicitly presented in the literature and if X-ray spectral shape does not show a clear signature of absorption,  $N_{\text{H}}$  is regarded as small as noted in Table 1.

### 3. DIAGNOSTIC DIAGRAMS

#### 3.1. Hardness and X-ray/Infrared Ratio

We first made a diagnostic diagram using the hardness ratio HR4 and the ratio between the X-ray CR in 0.2–12 keV and the infrared (18 or 90  $\mu\text{m}$ ) flux density.

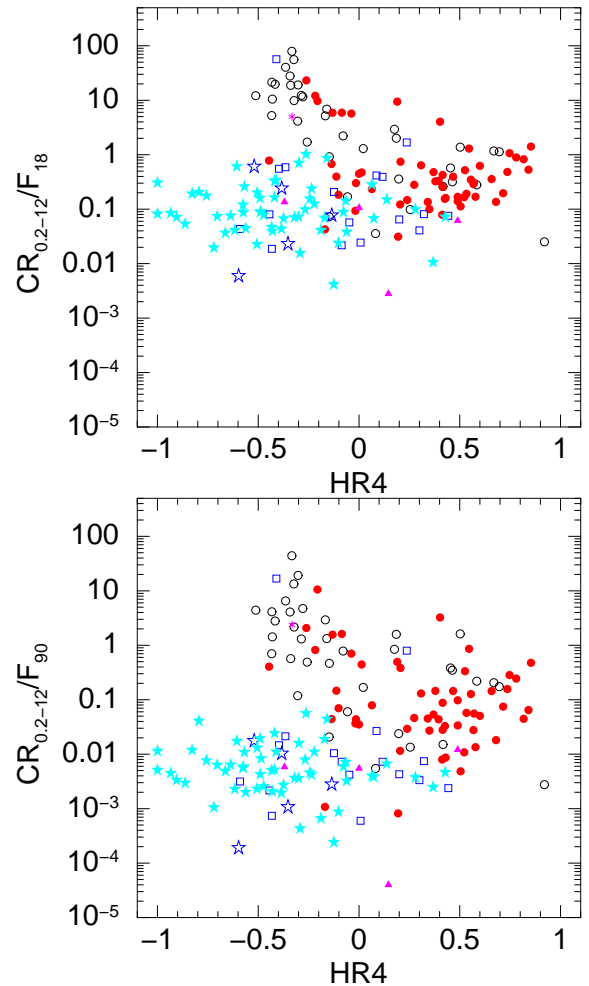


**Figure 8.** Hardness ratio (HR4) versus count rate ( $\text{CR}_{0.2-12}$ ) / infrared flux ( $F_{18}$  or  $F_{90}$ ) ratio diagram. Different symbols represent optical classifications; open circles: Seyfert 1, filled circles: Seyfert 2, open squares: LINER, open stars: transition object, filled stars: H II nucleus, asterisk: BL Lac object, filled triangles: unclassified. (Left) Diagram using 18  $\mu\text{m}$  flux as infrared flux. (Right) Diagram using 90  $\mu\text{m}$  flux as infrared flux.

These diagrams are essentially the same as that used by Severgnini et al. (2012). We used X-ray CRs instead of X-ray fluxes because X-ray CRs are values directly derived from observational data without any assumptions on the X-ray spectral shape. Our diagrams are shown in the left and right panels of Figure 8 for 18  $\mu\text{m}$  and 90  $\mu\text{m}$ , respectively. Different symbols are used to represent optical classifications of the activity. Seyfert 1, 1.2, and 1.5 are denoted as “Seyfert 1”, while Seyfert 1.8, 1.9, and 2 are shown as “Seyfert 2” in the diagrams.

Seyfert 1s are located in the upper left part of the diagram, while Seyfert 2s tend to be located in the lower right. The larger values of hardness ratios and lower X-ray counts relative to infrared fluxes of Seyfert 2s are due to the suppression of lower energy X-rays via photoelectric absorption. H II galaxies are located in the lower left side. The location of H II galaxies indicates that X-rays are relatively weak compared to AGNs at a given infrared power. In order to examine the effect of absorption, we defined three groups sorted by  $N_{\text{H}}$  and plotted them using different symbols in Figure 9. The ordinate and abscissa are same as in Figure 8. The open circles,

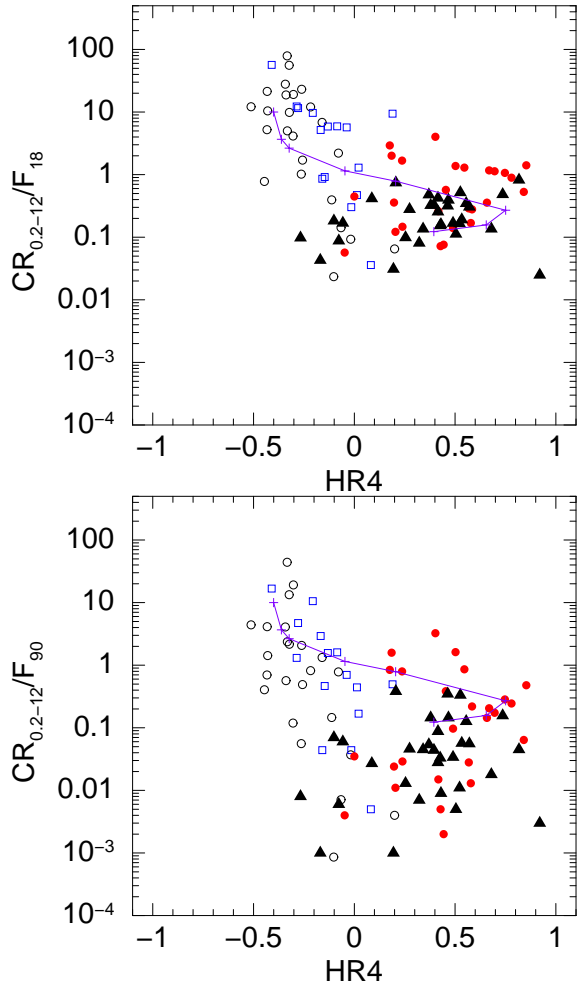


**Figure 9.** Hardness ratio (HR4) versus count rate ( $CR_{0.2-12}$ ) / infrared flux ( $F_{18}$  or  $F_{90}$ ) diagram same as Figure 2 but only AGNs with measured X-ray spectra are plotted. Different symbols represent  $N_H$  measured from X-ray spectra; open circles:  $N_H < 10^{22}$   $\text{cm}^{-2}$ , open squares:  $10^{22} < N_H < 10^{23}$   $\text{cm}^{-2}$ , filled circles:  $10^{23} < N_H < 10^{24}$   $\text{cm}^{-2}$ , filled triangles:  $N_H > 10^{24}$   $\text{cm}^{-2}$ . The solid lines are tracks expected for various column densities. EPIC-PN count rate (0.2–12 keV) to infrared flux (18  $\mu\text{m}$  or 90  $\mu\text{m}$ ) ratio of 10 is assumed at  $N_H = 0$   $\text{cm}^{-2}$ . The plus symbols are marked at  $N_H = (0, 0.5, 1, 5, 10, 50, 100, 150) \times 10^{22}$   $\text{cm}^{-2}$  from the upper-left most to the lowest most point. See the text for details of the assumed spectral model.

open squares, filled circles, and filled triangles represent the groups of  $N_H < 10^{22}$   $\text{cm}^{-2}$ ,  $N_H = 10^{22-23}$   $\text{cm}^{-2}$ ,  $N_H = 10^{23-24}$   $\text{cm}^{-2}$ , and  $N_H > 10^{24}$   $\text{cm}^{-2}$ , respectively. As expected, objects with lower and higher  $N_H$  tend to be located at around the upper left and lower right part of the diagrams, respectively.

We made tracks of expected hardness ratios and X-ray/infrared ratios for various values of  $N_H$ . A power-law spectrum with a photon index of 1.8 was assumed as incident emission. One percent of the incident emission is assumed to appear as scattered emission keeping the spectral shape. The Galactic absorption of  $2 \times 10^{20}$   $\text{cm}^{-2}$  is assumed as a representative value. The expected values were calculated for various intrinsic column densities from  $N_H = 0$  to  $1.5 \times 10^{24}$   $\text{cm}^{-2}$ . The track thus calculated is shown as the solid line in Figure 9, where the values of  $CR_{0.2-12}/F_{18}$  and  $CR_{0.2-12}/F_{90}$  are assumed to be 10 when  $N_H = 0$   $\text{cm}^{-2}$ . The plus signs

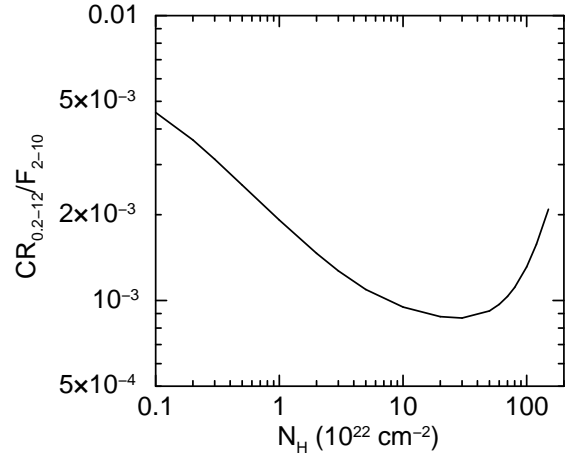


**Figure 10.** Flux to count rate conversion factor for various  $N_H$  values. The expected count rates in 0.2–12 keV for a source with a flux of  $10^{-14}$   $\text{erg s}^{-1} \text{cm}^{-2}$  in 2–12 keV are shown. See the text for details of the assumed spectral model.

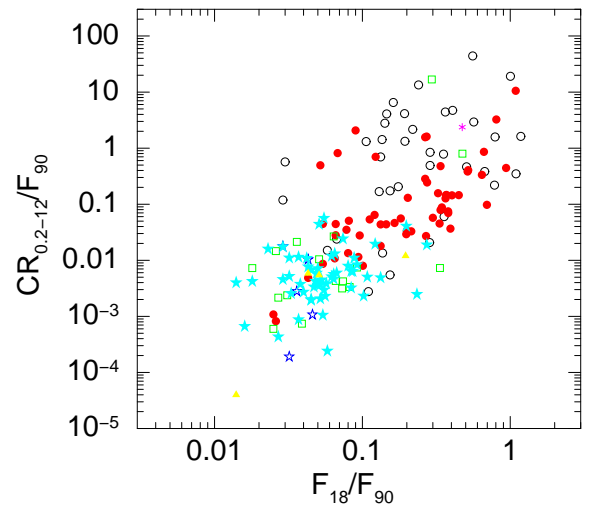


**Figure 11.** Count rate ( $CR_{0.2-12}$ ) / infrared flux ( $F_{90}$ ) ratio versus infrared flux ratio ( $F_{18}/F_{90}$ ) diagram. The symbols are same as in Figure 8.

are marked at  $N_H = (0, 0.5, 1, 5, 10, 50, 100, 150) \times 10^{22}$   $\text{cm}^{-2}$  from the upper left-most to the lowest point. The trend shows that X-ray counts are suppressed and that hardness ratio becomes larger for larger  $N_H$  values up to  $N_H \sim 5 \times 10^{23}$   $\text{cm}^{-2}$ . If  $N_H$  is larger than  $N_H \sim 5 \times 10^{23}$   $\text{cm}^{-2}$ , the flux from the scattered emission becomes more significant relative to the absorbed power-law emission, and the hardness ratio becomes small. The above considerations suggest that if objects appeared in the lower right part of the diagram, they are candidates for obscured AGNs. Some of the objects in this region have no published X-ray spectra. We study the X-ray spectra of such candidates for obscured AGNs selected from that region ( $CR_{0.2-12}/F_{90} < 0.1$  or  $CR_{0.2-12}/F_{18} < 1$ ) and  $HR4 > -0.1$  in section 4.

A disadvantage of using CRs instead of fluxes is that they depend on the instrument used in observations. We calculate the conversion factors from X-ray fluxes to observed CRs. The same spectral shape used to derive the track shown in Figure 9 is assumed. The on-axis response for the EPIC-PN and an integration radius of  $60''$ , which

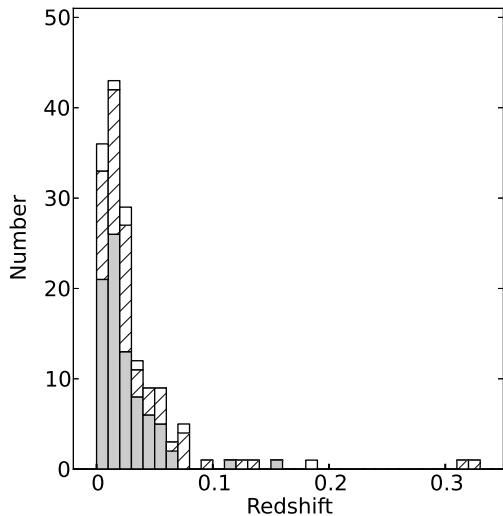


**Figure 12.** Distribution of redshifts for the  $18 + 90 \mu\text{m}$  (shaded histogram),  $90 \mu\text{m}$  (hatched histogram), and  $18 \mu\text{m}$  (open histogram) samples.

contains 95% of the total flux, are used. The expected CRs for an observed flux in 2–12 keV of  $10^{-14} \text{ erg s}^{-1} \text{ cm}^{-2}$  are shown as a function of the absorption column density in Figure 10.

### 3.2. Infrared Color and X-ray/Infrared ratio

Figure 11 shows a diagram  $\text{CR}_{0.2-12}/F_{90}$  versus infrared flux ratios ( $F_{18}/F_{90}$ ). This diagram supplements Figure 8 in dividing AGNs and H II nuclei. H II nuclei show smaller  $\text{CR}_{0.2-12}/F_{90}$  and  $F_{18}/F_{90}$  ratios compared to AGNs and are located in the lower left part of the diagram; most H II nuclei have ratios  $\text{CR}_{0.2-12}/F_{90} < 0.05$  and  $F_{18}/F_{90} < 0.2$ , while only several AGNs are found in this region. AGNs tend to show warmer infrared colors compared to H II nuclei, and the distributions of the color for Seyfert 1 and Seyfert 2 are almost identical. These results imply that the dust in AGNs are warmer than those in H II nuclei because of the presence of a hard heating source, confirming earlier studies (e.g., Wu et al. 2009). Comparison between type 1 and type 2 AGNs shows that Mid-IR emission from warm dust near the central engine is visible in both types of AGNs. Thus, we confirmed earlier results based on ground-based observations (Gandhi et al. 2009), or a combination of *AKARI* and hard X-ray surveys (Ichikawa et al. 2012, Matsuta et al. 2012).

## 4. X-RAY SPECTRA

### 4.1. The Sample and Data Reduction

As described in section 3.1, objects in the lower right part of the diagram HR4 versus CR/infrared flux ratio are candidates for obscured AGNs. In order to explore the nature of the candidates, we compiled X-ray results from the literature and analyzed X-ray spectra of objects for which no published results are available.

We first select objects satisfying ( $\text{CR}_{0.2-12}/F_{90} < 0.1$  or  $\text{CR}_{0.2-12}/F_{18} < 1$ ) and  $\text{HR4} > -0.1$  from the matched sample using X-ray, 18, and  $90 \mu\text{m}$ . This sample consists of 85 objects and is denoted as the  $18 + 90 \mu\text{m}$  sample hereafter. In addition to this sample, we selected

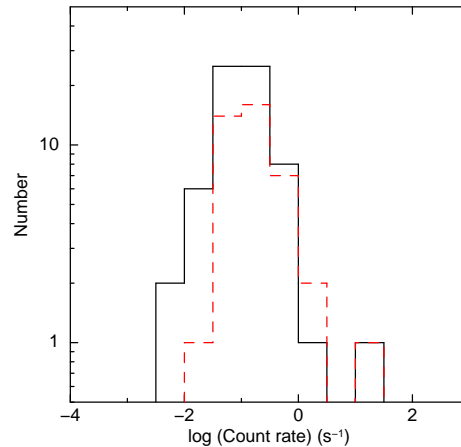


**Figure 13.** Distribution of X-ray count rates in the 0.2–12 keV band for  $18 \mu\text{m} + 90 \mu\text{m}$  sample (solid histogram) and Severgnini et al.'s sample (dashed histogram).

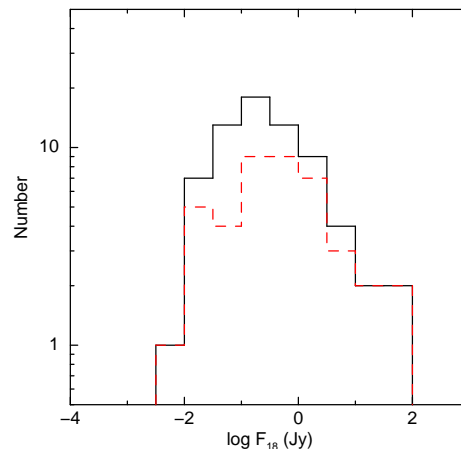


**Figure 14.** Distribution of flux densities at  $18 \mu\text{m}$  for objects satisfying the condition  $\text{CR}_{0.2-12}/F_{18} < 1$  in  $18 \mu\text{m} + 90 \mu\text{m}$  sample (solid histogram) and Severgnini et al.'s sample (dashed histogram).

objects satisfying  $\text{CR}_{0.2-12}/F_{90} < 0.1$  and  $\text{HR4} > -0.1$ , where we required the condition  $\text{FQUAL} = 3$  only for  $90 \mu\text{m}$  data to increase the size of the sample. 84 objects are selected by these conditions. The list of objects in this  $90 \mu\text{m}$  sample is shown in Table 3. We also selected objects with  $\text{FQUAL} = 3$  at  $18 \mu\text{m}$ ,  $\text{FQUAL} \neq 3$  at  $90 \mu\text{m}$ , and  $\text{HR4} > -0.1$ . This  $18 \mu\text{m}$  sample consisting of 10 objects is shown in Table 4. The probable counterparts, redshifts, optical classifications, and absorption column densities determined from X-ray spectra taken from the literature are shown in the tables. Redshifts are available for 83, 62, and 9 objects in the  $18 + 90 \mu\text{m}$ ,  $90 \mu\text{m}$ , and  $18 \mu\text{m}$  samples, respectively. The distributions of the redshifts are shown in Figure 12. We excluded stellar and off-nuclear sources from the sample as in the sample shown in Table 1. We inspected the X-ray data of objects with no published X-ray results as candidates for detailed studies. Then the following cases were excluded; objects located in bright diffuse emission of a cluster of galaxies or an early-type galaxy, in the outskirts of the point spread function of a bright source, on or near the gap between CCD chips, in crowded X-ray source regions such as star-forming regions.

The X-ray and infrared luminosities for the 90 and

18 $\mu$ m samples are summarized in Table 2 and Figures 5 and 6, in which both results taken from the literature and our own analysis presented in this section are shown. The  $K$ -corrections and references for X-ray data and distances are treated in the same manner for the sample presented in section 2.2.

We retrieved the data for the sample from the *XMM-Newton* Science Archive and examined their spectra. The *XMM-Newton* Science Analysis Software (SAS) version 13.0.0 and the calibration files as of 2013 May were used in the data reduction and analysis. We first made light curves of a region that does not contain bright sources in 10–12 keV to examine background stability and time intervals with high background rates were excluded. We extracted source spectra from a circular region centered at the source position with a radius of 4''–60''. The extraction radii were determined to achieve good signal to noise ratio and to avoid nearby sources. Background spectra were made from an off-source region in the same CCD chip and subtracted from the source spectra. After data screening and background subtraction, net source counts in 0.2–12 keV for some objects were found to be lower than 60 counts because of the reduced exposure time. Such objects were excluded from the following analysis since their photon statistics are not sufficient to create spectra of reasonable quality. The final sample consisting of 48 objects for X-ray spectral analysis and the observation log are summarized in Table 5. The infrared sample from which these objects are taken and Hubble type taken from the HyperLeda database (Paturel et al. 2003) are also shown in Table 5.

The response matrix file and ancillary response file were made by using the SAS. The spectra were binned so that each bin contains at least one count. More channels are binned in the figures shown below for presentation purposes. A maximum-likelihood method using the modified version of  $C$  statistic (Cash 1979) was employed to fit background-subtracted spectra. Spectral fits were performed with XSPEC version 12.8.0. The errors represent the 90% confidence level for one parameter of interest. Errors are not shown for the cases that the value of  $C$  statistic is much worse than that for the best-fit model.

The Galactic absorption was applied to all the models examined below. The Galactic absorption column densities (Kalberla et al. 2005) were obtained by the FTOOL `nh` and shown in Table 5. `phabs` or `zphabs` in XSPEC were used as a photoelectric absorption model. We examined the presence of an Fe-K emission line at around 6.4 keV by adding a Gaussian component. The line center energy was left free if the photon statistics were sufficient to constrain the energy, otherwise 6.4 keV was assumed. The line width was fixed at a Gaussian  $\sigma$  of 10 eV. For objects with a known redshift, all the model components except for the Galactic absorption were assumed to be emitted or absorbed at the source redshift. If a redshift is previously unknown and an Fe-K emission line is visible in our X-ray spectra, the source redshift was treated as a free parameter and was determined from the line, whose central energy was assumed to be 6.4 keV in the source rest frame. The redshifts for the X-ray analysis sample range from 0.00218 to 0.188 with a median of 0.020, where redshifts determined by an Fe-K line are included. We assumed a redshift of  $z = 0$  for all the other cases.

Fe line parameters are not shown if the photon statistics around 6.4 keV are not sufficient and if no meaningful constraints on the line is obtained. The results of the spectral fits described below are summarized in Tables 6 and 7. The adopted model is marked with an asterisk in Table 6. In these tables, spectral parameters for the best-fit models and models with fewer model components are shown for comparison. The observed fluxes and luminosities corrected for absorption (for objects with a known redshift) in the 2–10 keV band were derived for the best-fit spectral model and models giving a similar quality of fits to the best fit.

## 4.2. Results

We first summarize measurements of absorption column densities taken from the literature, and then provide detailed results of our own spectral analysis for the 48 objects, for which no X-ray results have been published so far. The 48 objects analyzed are divided into three groups (1) objects with absorbed spectrum, (2) objects showing very flat continuum and/or strong Fe-K fluorescent line, and (3) objects showing unabsorbed spectrum, and explained in turn.

### 4.2.1. X-ray Results Taken from the Literature

We compiled the results of X-ray spectral fits for our samples from the literature. Since our aim is to find obscured AGNs by combining X-ray and infrared data, we tabulated absorption column densities ( $N_{\text{H}}$ ) derived from X-ray spectra in Tables 1, 3, and 4 for the 18 + 90  $\mu$ m, 90  $\mu$ m, and 18  $\mu$ m samples, respectively. The  $N_{\text{H}}$  values are classified into three classes “Unabsorbed”, “Compton-thin”, and “Compton-thick” for objects with  $N_{\text{H}} < 10^{22}$   $\text{cm}^{-2}$ ,  $10^{22} < N_{\text{H}} < 1.5 \times 10^{24}$   $\text{cm}^{-2}$ , and  $N_{\text{H}} > 1.5 \times 10^{24}$   $\text{cm}^{-2}$ , respectively. If only a lower limit on  $N_{\text{H}}$  of  $1 \times 10^{24}$   $\text{cm}^{-2}$  is presented, such sources are regarded as Compton-thick. These classifications are shown in the “X-ray Class” column in Tables 1, 3, and 4. The classifications of X-ray absorption are available for 72, 22, and 9 objects for the 18 + 90  $\mu$ m, 90, and 18  $\mu$ m samples, respectively.

### 4.2.2. Absorbed Spectrum

X-ray spectra of 16 of the 48 objects we analyzed show convex shape, which is a signature of absorbed emission, implying the presence of an obscured AGN, at energies above  $\sim 2$  keV. Their spectra are shown in Figure 15. We fitted their spectra by a power-law model absorbed by neutral matter. First the photon index was treated as a free parameter, and then a model with a photon index fixed at 1.8 was examined. The result for a free photon index is shown if a meaningful constraint on the index is obtained.

The spectrum of 2MASX J05430955–0829274 is well fitted with this absorbed power-law model accompanied by an emission line at 6.4 keV. The rest of the objects show additional emission at energies below a few keV. We tried to model this emission by power law, APEC thermal plasma (Smith et al. 2001), or a combination of both. For the models with one power-law component, the photon index was left free or fixed at 1.8. The photon indices of the heavily absorbed power law, which dominates hard emission, and the additional power law representing the soft part of the spectra were fixed at 1.8 for



models containing two power-law components. A common photoelectric absorption model, which represent the absorption in the host galaxies, was applied to both of the power-law components. The APEC component was assumed to be absorbed only by the Galactic column. The spectra of the two objects 2MASX J05052442–6734358 and NGC 5689 are represented by the two power-law model. Other objects show excess emission around 0.6–1.0 keV, which implies the presence of Fe-L emission lines from hot plasma, and the APEC model was used to express this feature. An APEC + absorbed power-law model describes the spectra of UGC 959 and IC 5264. The spectra of the rest of the objects were fitted with a combination of two power-law and APEC components. IRAS 03156–1307 required two temperature APEC components in addition to the two power-law components.

The best-fit column densities for the heavily absorbed power-law component are  $N_{\text{H}} \approx 2 \times 10^{22} - 1.4 \times 10^{24} \text{ cm}^{-2}$ , which is a range expected for obscured AGNs. The column densities of the two objects IRAS 01356–1307 and NGC 2611 exceed  $1 \times 10^{24} \text{ cm}^{-2}$  and the effect of Compton scattering cannot be neglected. Therefore, we multiplied the `cabs` model in XSPEC ( $e^{-\sigma_{\text{T}} N_{\text{H}}}$ ), where  $\sigma_{\text{T}}$  is the Thomson scattering cross section. Although the energy dependence of the cross section is not taken into account, this model approximates the shape of the continuum transmitted through Compton-thick matter (Ikeda et al. 2009). This model affects only the normalization of the heavily absorbed power-law component.

The results of the spectral fits are summarized in Table 6, and the adopted models and data/model ratios are shown in Figure 15. If two or more models provide similar  $C$  statistics, we adopt models with the best-fit photon index in the range of 1.5–2.1, which is typical for X-ray spectra of AGNs. The results of spectral fits to the Fe-K line are shown in Table 7. The improvement of the  $C$  statistic by adding a Gaussian line is also shown in Table 7. An Fe-K emission line is seen in the spectra of 2MASX J05052442–6734358, 2MASX J05430955–0829274, and ESO 205–IG003. A hint of Fe-K emission is seen in SDSS J085312.35+162619.4. The photon statistics are poor around 6.4 keV in IRAS 03136–1307 and Fe line parameters are not shown for this object. The improvement of the  $C$  statistic for other objects is small for one additional parameter (normalization of a Gaussian).

#### 4.2.3. Flat Continuum and Strong Fe-K Emission Line

Ten objects show a flat continuum at energies above a few keV and/or a strong Fe-K emission line at around 6.4 keV. The spectral shape is much flatter than that typically observed in AGNs and implies that the spectrum is a combination of heavily absorbed and less absorbed power laws with typical photon indices for AGNs (two power-law model) or that the spectrum is reflection-dominated. Therefore, we examined continuum models for these two cases. We assumed a common photon index of 1.8 for the two power-law model. The `pexrav` model in XSPEC was used to represent a continuum reflected from cold matter (Magdziarz & Zdziarski 1995). The incident spectrum is assumed to be a power law with a photon index of 1.8 and an exponential cutoff at 300 keV. The reflection scaling factor (`rel_refl`) was set to  $-1$  to represent reflected emission alone. The inclination

angle of the reflector was assumed to be  $60^\circ$ , where the inclination of  $0^\circ$  corresponds to face on.

The spectrum of 2MASX J05391963–0726190 is fitted either by a pure reflection model or a two power-law model. A pure reflection model does not describe the spectra of IRAS 00517+4556, 2XMM J052555.5–661038, and 2XMM J184540.6–630522. The continuum of 2XMMi J184540.6–630522 is fitted by a flat power-law model or a combination of reflection and slightly absorbed power law. A combination of reflection and virtually unabsorbed power law or a two power-law model represent the spectra of IRAS 00517+4556 and 2XMMi J052555.5–661038.

The six objects, NGC 1402, IC 614, 2MASX J11594382–2006579, NGC 6926, 2MASX J23404437–1151178, and NGC 7738, show excess emission around 0.6–1.0 keV suggesting the presence of emission from optically thin plasma. We used an APEC plasma model to represent this feature. An APEC + reflection model describes the continua of IC 614, 2MASX J11594382–2006579, and NGC 6926. An APEC + absorbed power-law model also provided a similar quality of fit to 2MASX J11594382–2006579. 2MASX J23404437–1151178 and NGC 7738 require an additional power-law component, where we assumed a common  $N_{\text{H}}$  for the reflection and power-law components since the quality of the data is not sufficient to constrain  $N_{\text{H}}$  values for these components separately. The spectrum of NGC 1402 is not very flat, and a combination of APEC and lightly absorbed power law represents the shape of the continuum.

The six objects, NGC 1402, IC 614, 2XMMi J184540.6–630522, NGC 6926, 2MASX J23404437–1151178, and NGC 7738, show an emission line at around 6.4 keV in the source rest frame with an EW in the range of 1.1–4.6 keV. An Fe-K line at 6.4 keV is not detected in other objects except for a weak hint of a line in NGC 4713. An emission-line-like excess at around 7.0 keV is seen in the spectrum of IRAS 12596–1529. If this line is assumed to be from H-like Fe at 6.97 keV, the  $C$  statistic is improved by  $\Delta C = 5.5$  for one additional parameter (normalization of a Gaussian). 2MASX J11594382–2006579 shows a line-like emission at  $\approx 5.8$  keV. If this emission is an Fe-K line at 6.4 keV in the source rest frame, the redshift is estimated to be  $0.112^{+0.019}_{-0.018}$ , though the improvement of the fit is only  $\Delta C = 3.0$  for two additional parameters (normalization of a Gaussian and source redshift). Limits on the EW of Fe-K line at 6.4 keV were derived for objects with sufficient counts around 6.4 keV.

The results of the spectral fits are summarized in Tables 6 and 7. The observed spectra, adopted models, and data/model ratios are shown in Figure 16. If two or more models give fits of similar quality, we adopt one or two models as the most appropriate ones satisfying the following conditions: (1) the best-fit photon index is in the range of 1.5–2.1 and (2) the constraint on the EW on an Fe-K fluorescent line at 6.4 keV is consistent with the best-fit  $N_{\text{H}}$  as observed in obscured AGNs (Guainazzi et al. 2005a, Fukazawa et al. 2011).

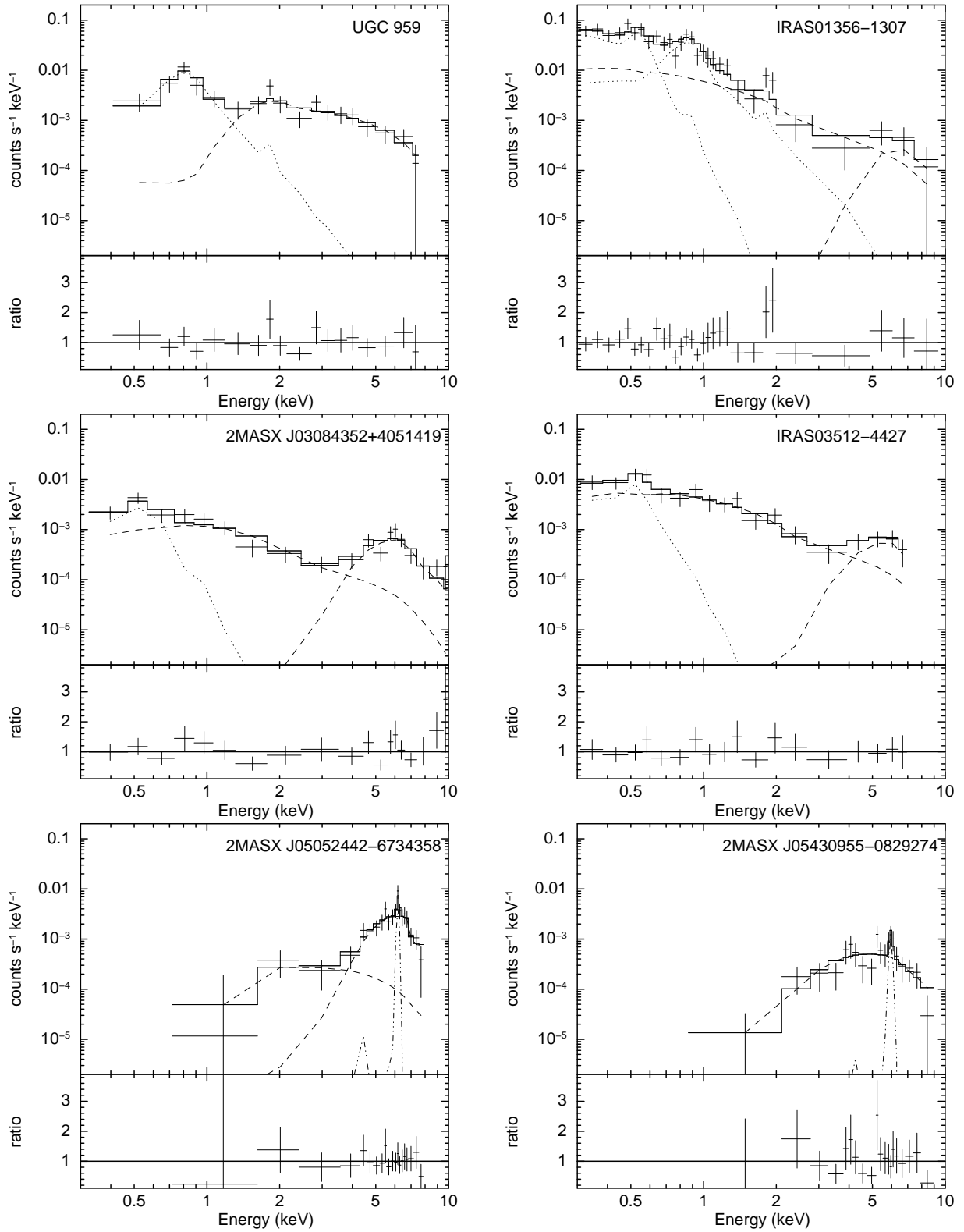


**Figure 15.** EPIC-PN spectra of objects showing absorbed continuum. (Upper panel) Data (crosses) and adopted best-fit model (solid histogram). Spectral components are shown as dashed, dotted, dot-dot-dot-dashed lines. (Lower panel) Data/Model ratio.

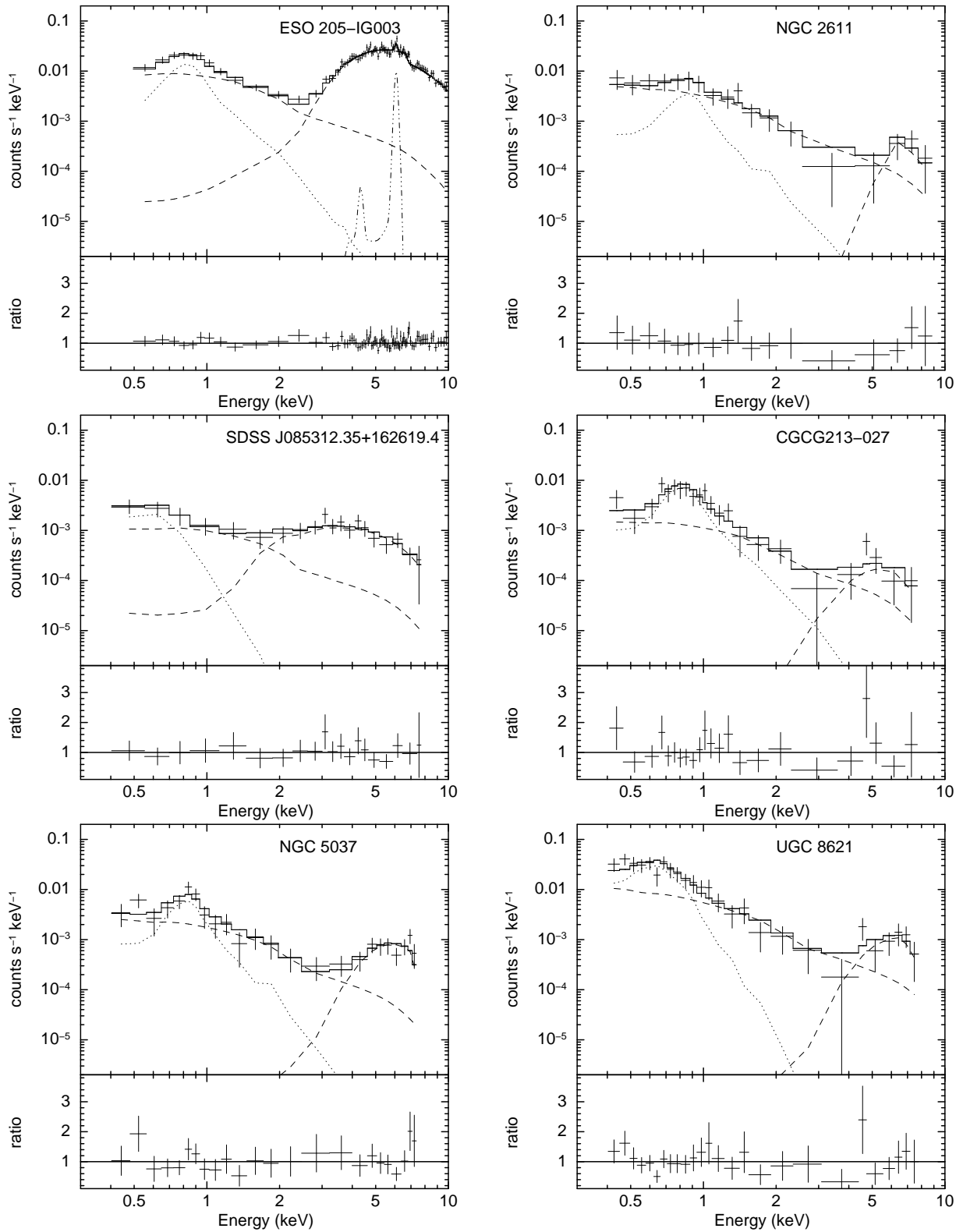


Figure 15. Continued.

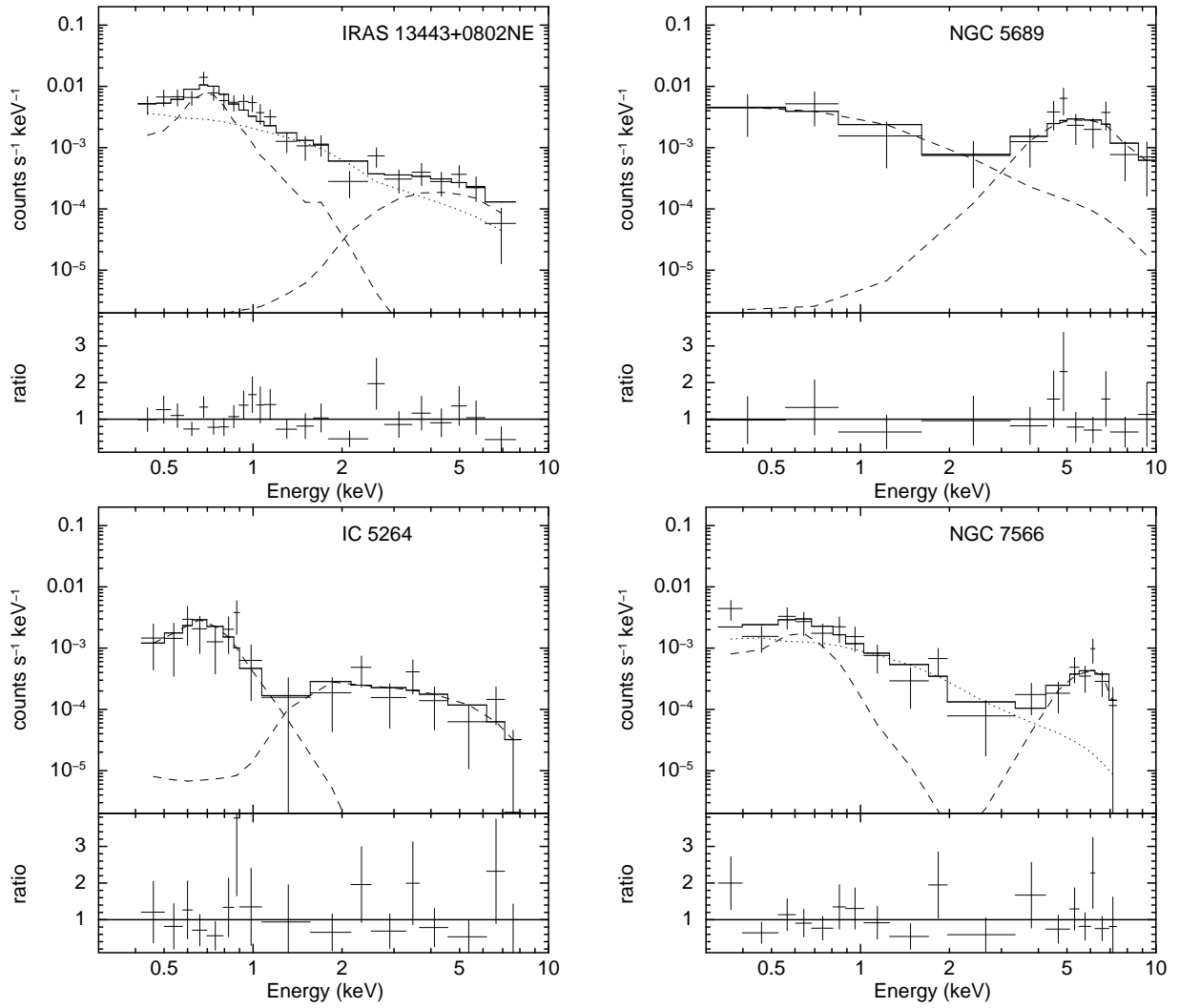


Figure 15. Continued.

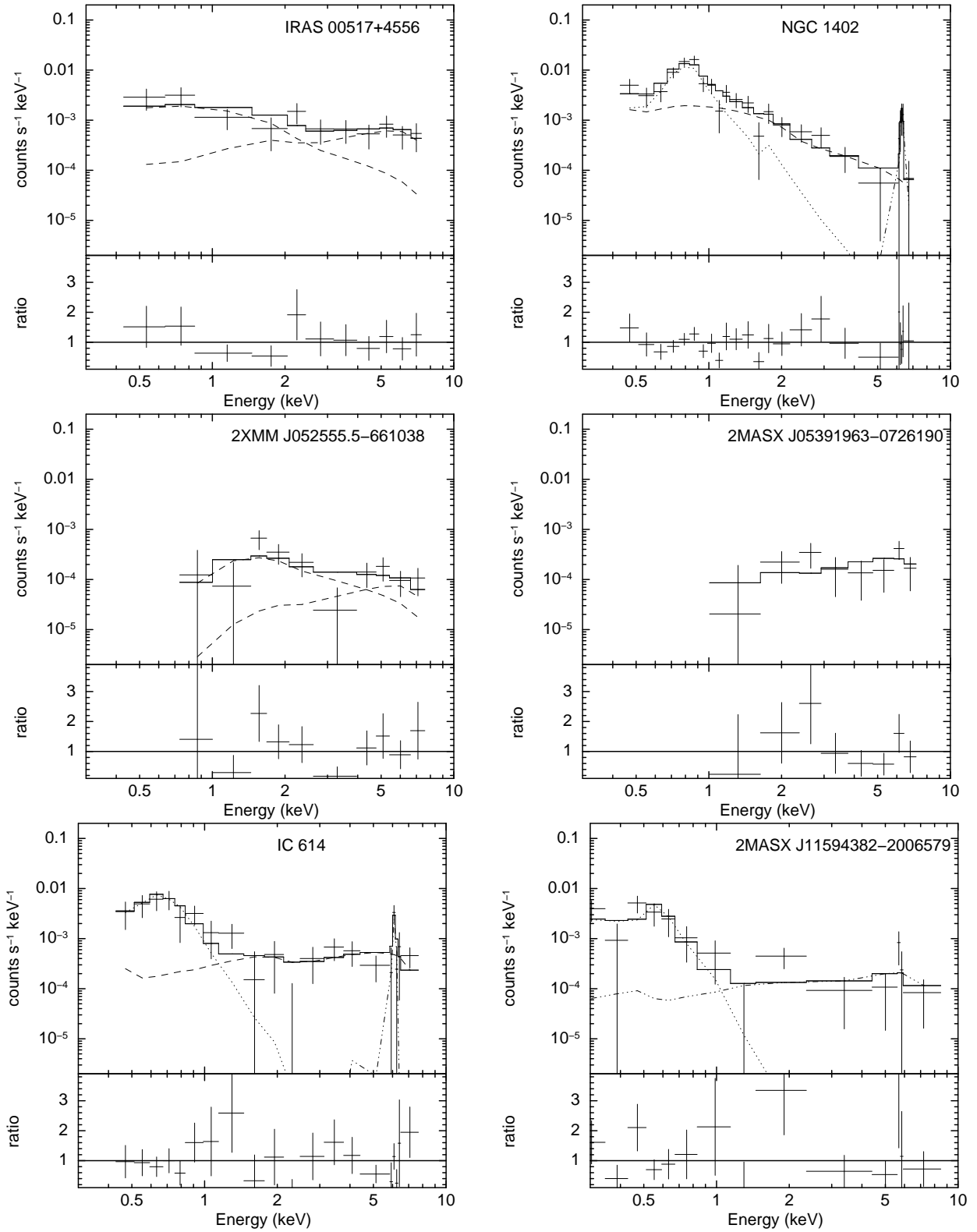


Figure 16. EPIC-PN spectra of objects showing flat continuum and/or strong Fe-K emission.

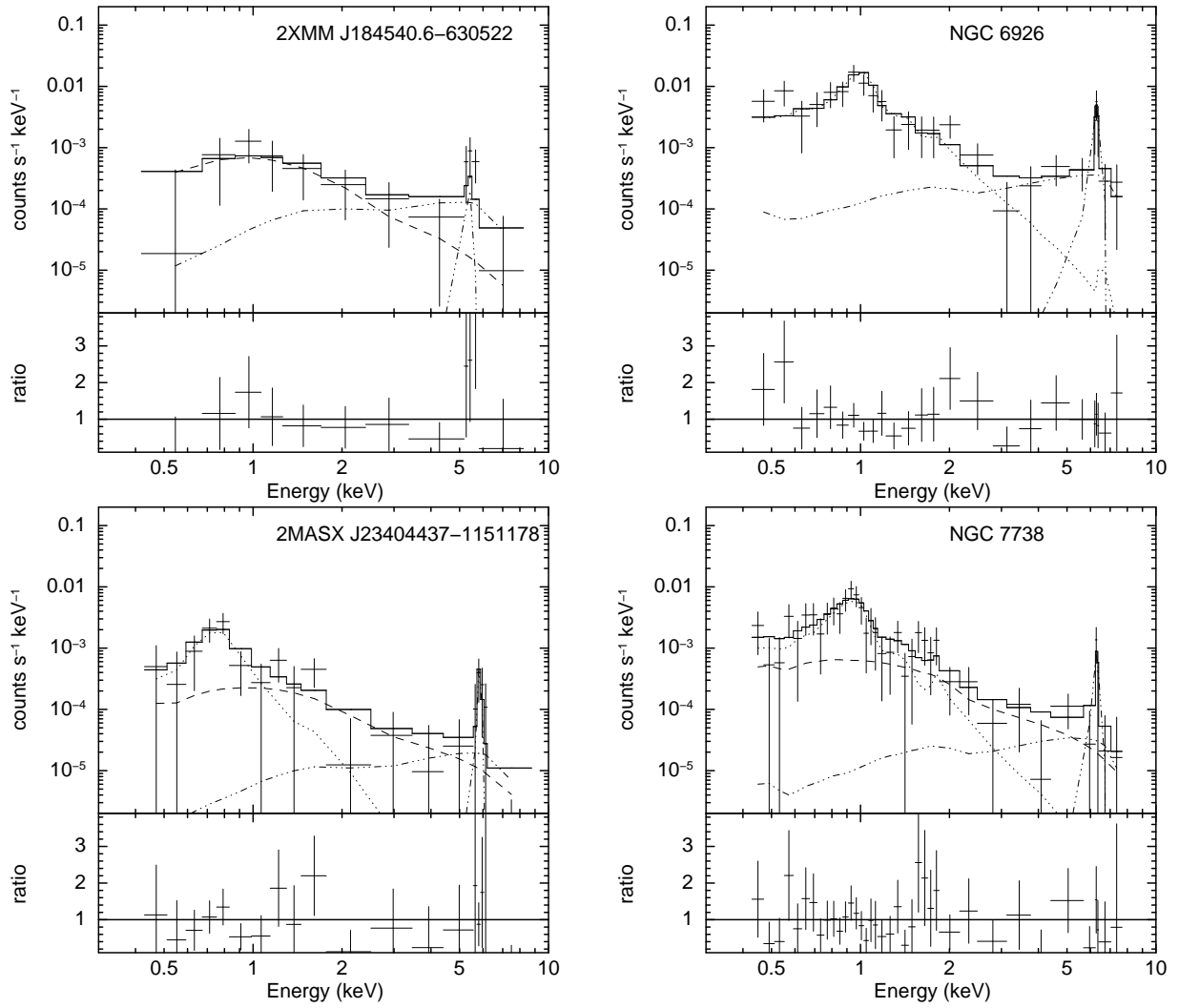


Figure 16. Continued.

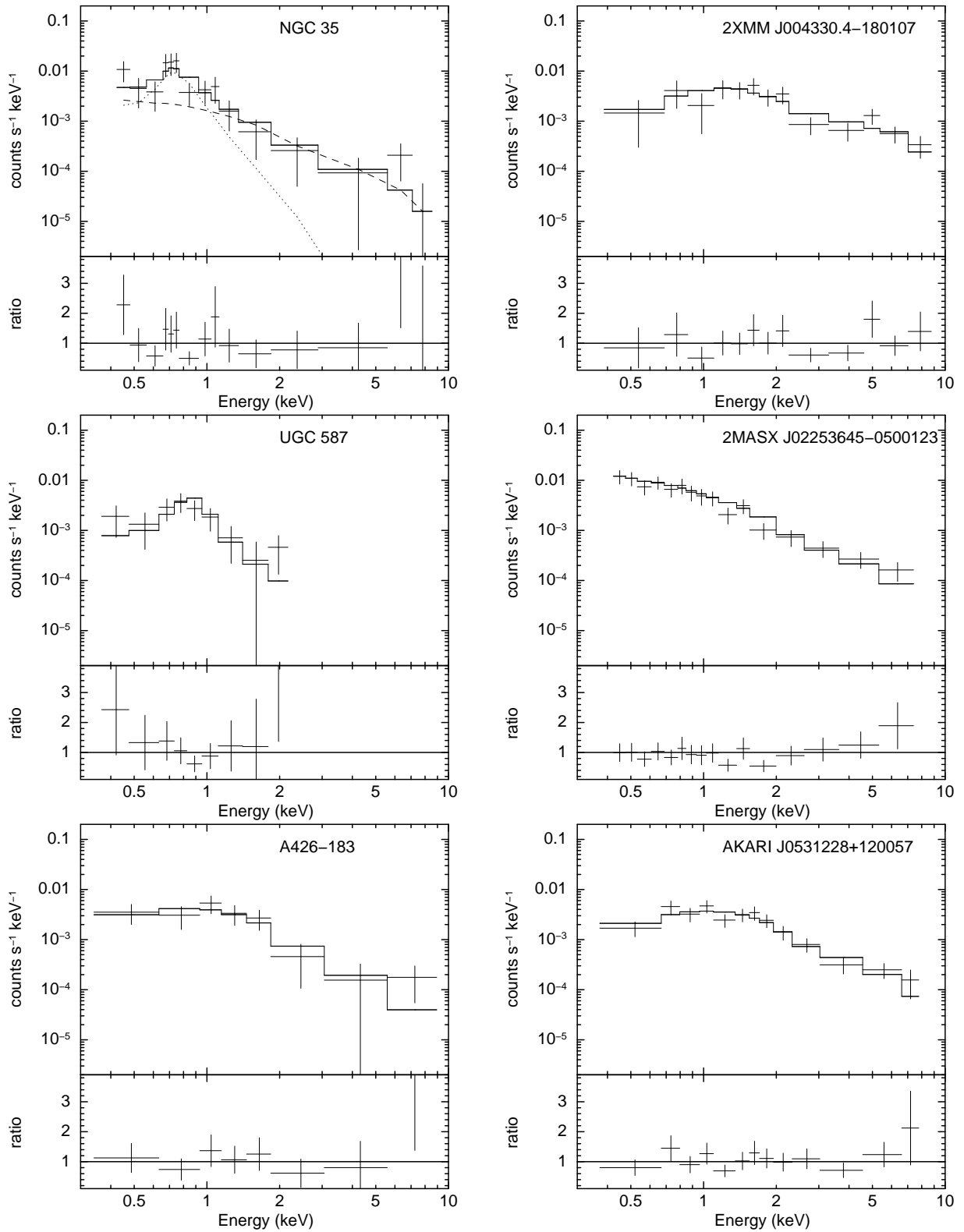


Figure 17. EPIC-PN Spectra of unabsorbed objects.

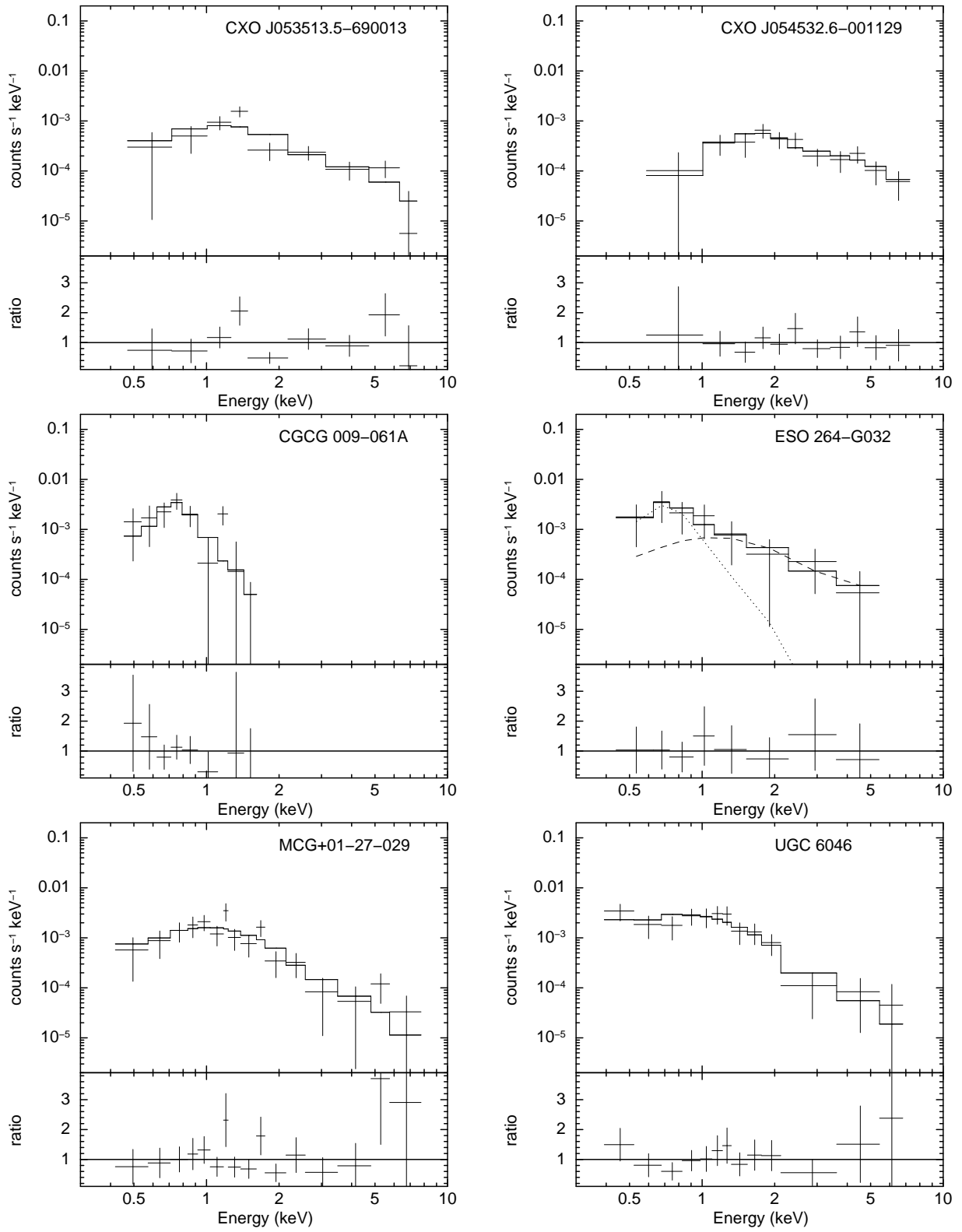


Figure 17. Continued



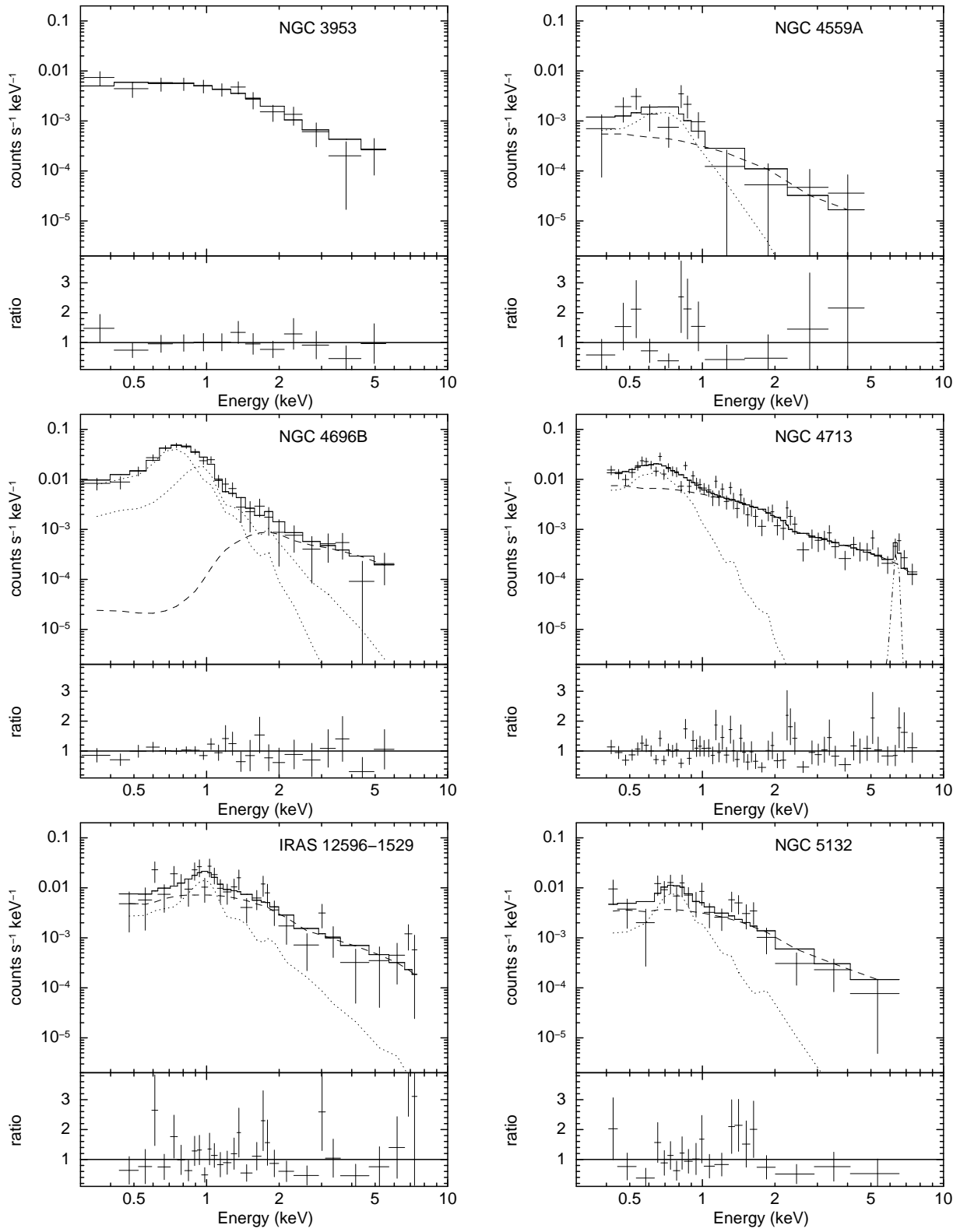


Figure 17. Continued

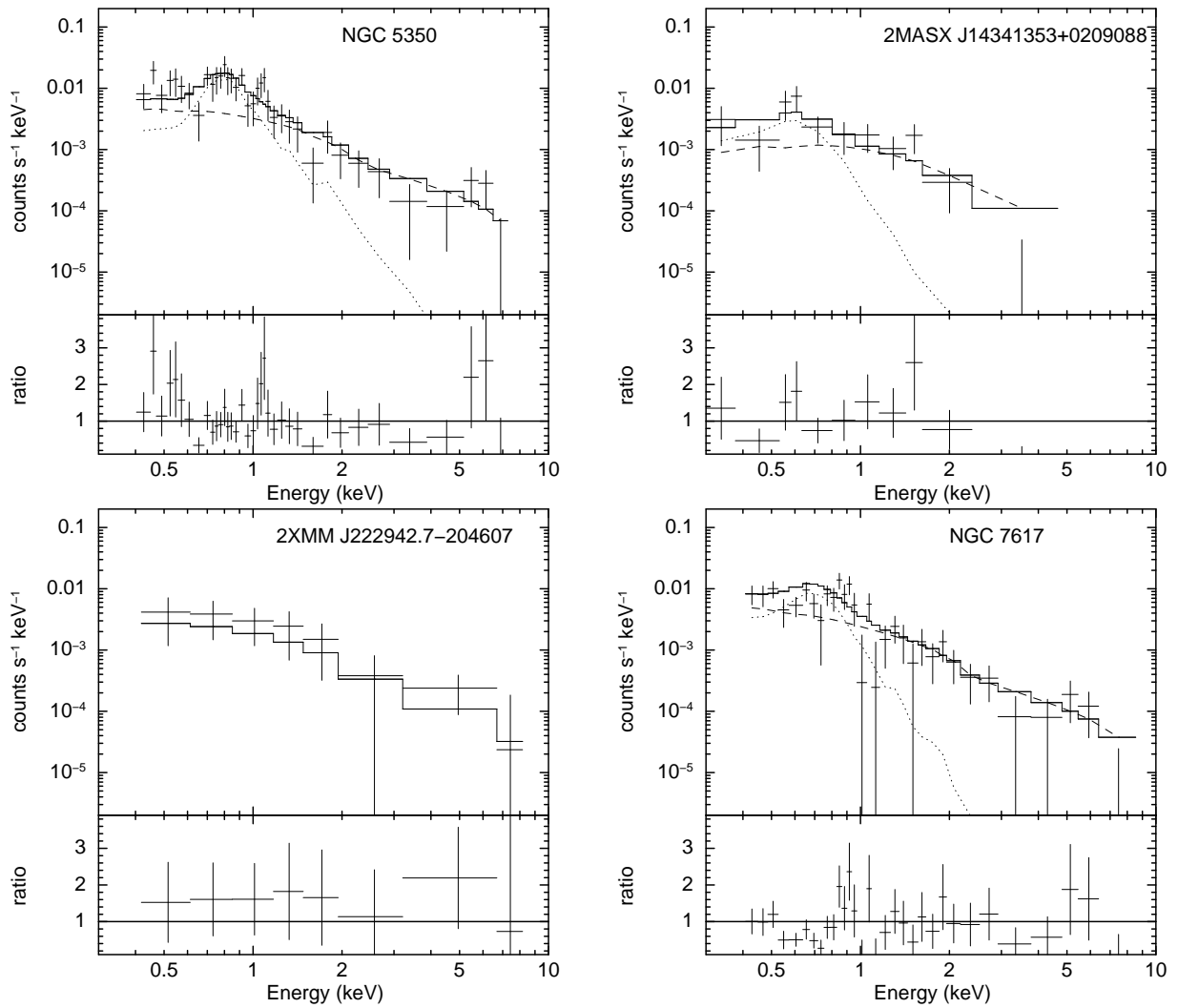


Figure 17. Continued

#### 4.2.4. Unabsorbed Spectrum

The rest of the objects do not show a signature of heavy absorption. We applied an absorbed power-law model to the spectra. The photon index  $\Gamma$  was first treated as a free parameter. If the photon index was not well constrained,  $\Gamma = 1.8$  was assumed. Good fits were obtained for 12 objects (2XMM J004330.4–180107, 2MASX J02253645–0500123, A426[BM99]183, AKARI J0531228+120057, 2XMMi J053512.2–690009, CXO J054532.6–001129, MCG +01–27–029, UGC 6046, NGC 3953, NGC 5132, 2XMM J222942.7–204607, and NGC 7617). An APEC plasma model was also examined instead of power law, and similar quality of fits were obtained for A426[BM99]183, AKARI J0531228+120057, 2XMMi J053512.2–690009, UGC 6046, NGC 3953, and 2XMM J222942.7–204607. The spectra of UGC 587 and CGCG 009–061A appear very soft, and an APEC model with a temperature of 0.3–1 keV provided a good description of the data.

The single-component models do not fit the spectra of eight objects (NGC 35, ESO 264–G032, NGC 4559A, NGC 4696B, NGC 4713, IRAS 12596–1529, NGC 5350, and 2MASX J14341353 +0209088). Although the spectra of NGC 5132 and NGC 7617 are fitted by a power-law model, the resulting photon indices are very steep (3.3 and 2.8, respectively) and may indicate the presence of a soft component. We therefore examined a two component-model consisting of APEC plasma and absorbed power law with a fixed photon index of 1.8. This model describes the spectra of all but NGC 4696B. The addition of a second APEC component well fits the spectrum of NGC 4696B.

Two objects (NGC 4713 and IRAS 12596–1529) show a hint of an emission line at 6–7 keV. The improvements of the  $C$  statistic are 5.3 and 5.5 for one additional parameter (normalization of a Gaussian) if the line center energies of 6.4 keV and 6.97 keV were assumed for NGC 4713 and IRAS 12596–1529, respectively. Other objects do not show an Fe-K emission line feature. The upper limits on the EW of a Gaussian line at 6.4 keV were derived for objects with sufficient photon statistics around an Fe-K line and summarized in Table 7. The results of the fits are summarized in Table 6. The observed spectra and the adopted models are shown in Figure 17.

## 5. DISCUSSION

### 5.1. Selection of Obscured AGNs

We made diagnostic diagrams using X-ray CRs, X-ray hardness, and infrared fluxes, which can be used to select candidates for obscured AGNs. By accumulating the published results of X-ray spectral analysis, we found that the regions satisfying ( $CR_{0.2-12}/F_{18} < 1.0$  or  $CR_{0.2-12}/F_{90} < 0.1$ ) and  $HR4 > -0.1$  are the loci for obscured AGNs. We analyzed the X-ray spectra of 48 objects with X-ray counts greater than 60, for which no X-ray spectra are published. Of these, 26 show a signature of absorbed X-ray spectra. Their classifications of X-ray absorption as Compton-thin or Compton-thick are summarized in Table 6. The 16 objects analyzed in section 4.2.2 show a spectral curvature indicative of the continuum absorbed by  $N_H \approx 10^{22-24} \text{ cm}^{-2}$ . Their best-fit  $N_H$  values are in the

range of  $3 \times 10^{22} - 1.4 \times 10^{24} \text{ cm}^{-2}$ , which are typically observed in Seyfert 2 galaxies. The two objects showing the largest best-fit  $N_H$  ( $1.05 \times 10^{24} \text{ cm}^{-2}$  for IRAS 01356–1307 and  $1.4 \times 10^{24} \text{ cm}^{-2}$  for NGC 2611) are regarded as Compton-thin in the discussion below since these  $N_H$  values are slightly below the boundary of Compton-thin/thick column densities ( $1.5 \times 10^{24} \text{ cm}^{-2}$ ; Comastri 2004). Note, however, that the boundary value of  $N_H$  between Compton-thin/thick depends on the assumed abundance of the absorber (Yaqoob et al. 2010). The 10 objects analyzed in section 4.2.3 show a flat continuum and/or a strong Fe-K emission line. Six of these objects are most likely to be Compton-thick AGNs judging from their flat continuum and strong Fe-K emission line. The Fe-K emission line is not significant in four (IRAS 00517+4556, 2MASX J05255807–6610523, 2MASX J05391963–0726190, and 2MASX J11594382–2006579) of the 10 objects, and their flat continuum could be interpreted as either a reflection-dominated spectrum or a combination of mildly absorbed ( $4 \times 10^{22} - 4 \times 10^{23} \text{ cm}^{-2}$ ) and less absorbed components. These objects are tentatively regarded as Compton-thick in the following discussion and denoted as “Thick?” in the X-ray class column of Table 6. Thus, 26 objects in total are most likely obscured AGNs, for which X-ray signatures of the presence of AGNs are reported for the first time in this paper. The 22 objects analyzed in section 4.2.4, on the other hand, show no clear evidence for the presence of obscured AGNs.

By combining the X-ray results taken from the literature and our own analysis, Table 8 summarizes the number of objects in the 18 + 90  $\mu\text{m}$ , 90, and 18  $\mu\text{m}$  samples, objects with X-ray measurements of absorption column densities, and unabsorbed/Compton-thin/Compton-thick objects. Usable X-ray data are available for 84% of the combined sample. Among the 151 objects with X-ray measurements, 113 (75%) are absorbed by Compton-thin or Compton-thick matter. If only sources securely detected at 18  $\mu\text{m}$  are used, 82 of 89 objects (92%) are absorbed.

The MIR band is better for detecting emission from warm dust heated by an AGN compared to the far-infrared band. Therefore, we first discuss the success rate to find obscured AGNs selected by the criteria using 18  $\mu\text{m}$  data. Among our *XMM+AKARI* sample, 79 objects satisfy the conditions  $CR_{0.2-12}/F_{18} < 1.0$  and  $HR4 > -0.1$ . The absorption column densities of 44 and 29 objects among them are in  $N_H = 1 \times 10^{22} - 1.5 \times 10^{24} \text{ cm}^{-2}$  and larger than  $1.5 \times 10^{24} \text{ cm}^{-2}$ , respectively. The detection rate of AGNs absorbed by  $N_H > 10^{22} \text{ cm}^{-2}$  is  $73/79 \approx 92\%$ , which demonstrates the efficiency of our criteria finding obscured AGNs.

Severgnini et al. (2012) applied a similar selection technique to the sample derived from the *IRAS* point source and 2XMM catalogs. They used the conditions of  $F(2 - 12 \text{ keV})/\nu_{25} F_{25} < 0.02$  and  $HR4 > -0.2$  and selected 43 candidates for Compton-thick AGNs. Of the 43 AGNs, 40 are in common with our sample of obscured AGNs. Two objects (IRAS 04507+0358 and 3C321) are not selected in our sample since EPIC-PN data are not available for them. One object (NGC 5194) has an  $HR4$  value of  $-0.11$  that is slightly smaller than our adopted

boundary ( $\text{HR4} > -0.1$ ) but satisfies Severgnini et al.’s criterion ( $\text{HR4} > -0.2$ ).

In Severgnini et al.’s sample, 32 of 43 are confirmed to be Compton-thick AGNs. The classification of Compton thickness for four objects are model-dependent, and seven are Compton-thin. If the conversion between *IRAS* 25  $\mu\text{m}$  and *AKARI* 18  $\mu\text{m}$  flux densities of equation (3) in Ichikawa et al. (2012) is assumed, their criterion translates into  $\text{CR}_{0.2-12}/F_{18} < 0.24$  and 0.64 for assumed  $N_{\text{H}}$  of  $5 \times 10^{23} \text{ cm}^{-2}$  and  $1 \times 10^{22} \text{ cm}^{-2}$ , respectively, where the same spectral shape as in section 3.1 was used. Thus, our criteria ( $\text{CR}_{0.2-12}/F_{18} < 1.0$ ) cover X-ray brighter objects relative to MIR fluxes, and this might result in the smaller Compton-thick fraction (44/79) derived for our sample.

Another difference between Severgnini et al.’s and our selection criteria is the limited X-ray and infrared flux levels. Severgnini et al. selected objects with an X-ray flux in 4.5–12 keV larger than  $1 \times 10^{-13} \text{ erg s}^{-1} \text{ cm}^{-2}$ . This flux corresponds to  $7 \times 10^{-14} \text{ erg s}^{-1} \text{ cm}^{-2}$  in 2–10 keV, if  $N_{\text{H}} = 5 \times 10^{23} \text{ cm}^{-2}$  and the spectral shape used in section 3.1 are assumed. The fluxes in 2–10 keV of all but one in our sample are larger than this flux. The flux of one object (2MASX J05391963–0726190) is  $\sim 4 \times 10^{-14} \text{ erg s}^{-1} \text{ cm}^{-2}$  in 2–10 keV, which is only slightly below the flux limit. We also compared the distributions of X-ray count rates in 0.2–12 keV. The solid histogram in Figure 13 is the distribution for 68 obscured AGN candidates satisfying the 18 or 90  $\mu\text{m}$  criteria selected from Table 1. The distribution of the CRs for the Compton-thick candidates in Severgnini et al. (2012) is shown as a dashed histogram in the same figure. Our sample contains more X-ray fainter objects compared to Severgnini et al.’s sample. Therefore, the X-ray flux limit likely explains the difference in the Compton-thick fraction in part. The distributions of 18  $\mu\text{m}$  fluxes for the 70 objects satisfying the condition  $\text{CR}_{0.2-12}/F_{18} < 1$  in the 18 + 90  $\mu\text{m}$  sample and Severgnini et al.’s Compton-thick candidates are also compared in Figure 14. We compiled 18  $\mu\text{m}$  fluxes measured with *AKARI* IRC for the latter. Six sources do not have 18  $\mu\text{m}$  data, and their *IRAS* 25  $\mu\text{m}$  fluxes are converted to 18  $\mu\text{m}$  fluxes by using the equation (3) in Ichikawa et al. (2012). Although the lower bounds of the distribution are similar, our sample contains a somewhat larger number of objects at fainter infrared fluxes. In summary, the combination of the larger numbers of X-ray faint or infrared faint objects compared to Severgnini et al.’s is likely to be a reason why we were able to find new obscured AGNs not included in Severgnini et al.’s sample.

We also used criteria using far infrared fluxes at 90  $\mu\text{m}$ ,  $\text{CR}_{0.2-12}/F_{90} < 0.1$  and  $\text{HR4} > -0.1$ . The contribution from cold dust heated by stellar processes in the host galaxy is likely to be significant in the far infrared band unless an AGN overwhelms the emission from the host galaxy. Therefore, a low  $\text{CR}_{0.2-12}/F_{90}$  ratio does not necessarily mean that X-ray emission is weak relative to the infrared because of the heavy absorption of an AGN. We thus expect the criteria using far infrared are less efficient to select obscured AGNs compared to the MIR selection. On the other hand, the combination of X-ray hardness and a low X-ray/IR ratio provides us with a chance to find AGNs buried in starburst

activity. There are 83 objects satisfying the conditions  $\text{CR}_{0.2-12}/F_{90} < 0.1$ ,  $\text{HR4} > -0.1$ , and not securely detected in the 18  $\mu\text{m}$  band. The presence of AGNs absorbed by a column density greater than  $10^{22} \text{ cm}^{-2}$  is reported for 31 objects in the literature or in this paper. The  $N_{\text{H}}$  values for 21 and 10 objects are in the range of  $1 \times 10^{22} - 1.5 \times 10^{24} \text{ cm}^{-2}$  and larger than  $1.5 \times 10^{24} \text{ cm}^{-2}$ , respectively, where three objects classified as “Thick?” are regarded as Compton-thick. There is no indication of absorption in excess of  $10^{22} \text{ cm}^{-2}$  in 31 objects. No  $N_{\text{H}}$  measurements are available for the rest of the objects (19 objects). Therefore, the detection rate of obscured AGNs using the far infrared criteria is 31/62=50% for the sample with  $N_{\text{H}}$  measurements.

The 22 objects analyzed in section 4.2.4 show no clear evidence for the presence of an obscured AGN. This result apparently contradicts our selection using hard X-ray spectra measured by the hardness ratio of  $\text{HR4} > -0.1$ . A possible reason for this contradiction is the faintness of the sources in the hard X-ray band. The net counts in the 4.5–12 keV for 15 among the 22 objects are less than 42 according to the 2XMMi catalog. The uncertainties of the hardness ratios are very large for such faint objects and sources with an unobserved spectrum could be chosen by our criteria. In one case (UGC 587), almost no photons are seen above 2 keV in our X-ray spectrum, but the 4.5–12 keV count in the 2XMMi catalog is 110 counts. This case is likely to be due to a combination of very low real X-ray counts and uncertainties in background estimation. The 4.5–12 keV counts for rest of the objects are in the range of 120–250 and their  $\text{HR4}$  values are around 0.0, which is relatively soft among the objects selected by our criteria. The inspection of their spectra indicates that the  $\text{HR4}$  values are reliable and consistent with the observed unabsorbed spectra within the errors.

## 5.2. Obscured AGNs Outside the Selection Criteria

While our selection criteria efficiently select obscured AGNs as discussed in the previous subsection, there are some obscured AGNs located outside our criteria in Figure 9. We examine the nature of these outliers using the 18 + 90  $\mu\text{m}$  sample. None of 29 objects absorbed by  $N_{\text{H}} > 10^{24} \text{ cm}^{-2}$  are located in the region  $\text{CR}_{0.2-12\text{keV}}/F_{18} < 1$ . Of the 26 objects in the range of  $N_{\text{H}} = 10^{23-24} \text{ cm}^{-2}$ , 9 have  $\text{CR}_{0.2-12\text{keV}}/F_{18} > 1$ . This ratio scatters from object to object, and the number of objects with  $\text{CR}_{0.2-12\text{keV}}/F_{18} > 1$  depends on the choice of the boundary. We set the criteria to efficiently select more absorbed objects ( $> 10^{24} \text{ cm}^{-2}$ ), which resulted in missing some moderately absorbed objects ( $N_{\text{H}} = 10^{23-24} \text{ cm}^{-2}$ ) in our criteria.

Seven out of 29 sources absorbed by  $N_{\text{H}} > 10^{24} \text{ cm}^{-2}$  and 12 out of 26 absorbed by  $N_{\text{H}} = 10^{23-24} \text{ cm}^{-2}$  are outside our criteria using 90  $\mu\text{m}$  data. Inspection of Figure 9 (left and right) clearly shows that scatters in X-ray to infrared ratios are much larger if 90  $\mu\text{m}$  data are used. A possible reason is that there is a wide range of the contribution of infrared emission from relatively cold dust heated by sources other than AGNs depending on the nature of host galaxies. While the scatters naturally worsen the success rate to find obscured AGNs, there is a higher probability of finding AGN activity hidden behind starbursts.

Among 55 sources with  $N_{\text{H}} > 10^{23} \text{ cm}^{-2}$ , three objects do not satisfy the condition  $\text{HR4} > -0.1$ . In these objects (NGC 3690,  $\text{HR4} = -0.267$ ; Mrk 1,  $\text{HR4} = -0.101$ ; NGC 2623,  $\text{HR4} = -0.169$ ), there is a considerable contribution from soft thermal emission to the band pass used to calculate HR4, where the 2.0–4.5 keV band is used as the soft band. Since their absorption column densities are above  $10^{24} \text{ cm}^{-2}$ , their X-ray spectra of AGN component below 10 keV are reflection-dominated and the low-energy cutoff due to photoelectric absorption is not clearly seen. The combination of the significant contribution of soft thermal emission and the absence of absorbed direct emission results in the relatively small HR4 values. If starburst activity coexists with obscured AGNs, soft thermal emission from starburst contributes to X-rays. In the infrared band, emission from cool dust associated with star formation activity results in smaller X-ray to 90  $\mu\text{m}$  ratios. Such cases tend to be missed if our criteria are applied.

### 5.3. *Optically Elusive AGNs*

There are several objects classified as an H II nucleus showing a relatively large hardness ratio. In the 18 + 90  $\mu\text{m}$  sample, the hardness ratios HR4 of nine objects (IRAS 01173+1405, NGC 695, NGC 3877, IRAS 12550–2929, IRAS 12596–1529, NGC 5253, IRAS 20551–4250, IRAS 23128–5919, and NGC 7738) are greater than  $-0.1$ . The presence of an AGN is known in NGC 695, IRAS 12550–2929, IRAS 20551–4250, and IRAS 23128–5919 (Brightman & Nandra 2011a, Severgnini et al. 2012) and the latter three show significant absorption. A signature of the presence of a Compton-thick AGN is clearly seen in our spectrum of NGC 7738. All of these AGNs satisfy the conditions  $\text{CR}_{0.2-12}/F_{18} < 1$  and  $\text{CR}_{0.2-12}/F_{90} < 0.1$ .

Fifteen objects classified as H II nuclei in the 90  $\mu\text{m}$  sample have  $\text{HR4} > -0.1$ . Obscured AGNs are found in NGC 1402, SDSS J085312.35+162619.4, IRAS 13443+0802NE, and IC 5264. The former object is Compton-thick and the latter three are Compton-thin. Seven objects show no clear indication of the presence of an obscured AGN (section 4.2.4; IRAS 10190+1322, Teng et al. 2010; NGC 3314, Hudaverdi et al. 2006) and four are excluded from our analysis sample (section 4.1). These AGNs with an optical classification of an H II nucleus are a class of “optically elusive” AGNs. Examples of optically elusive AGNs have been reported from infrared-selected samples. Classical examples are the discovery of Compton-thick AGN in infrared bright starburst galaxies (NGC 4945, Iwasawa et al. 1993; NGC 6240, Iwasawa & Comastri 1998; Arp 299, Della Ceca et al. 2002). Maiolino et al. (2003) compiled a sample of non-Seyfert galaxies selected by infrared luminosity, infrared color, and the presence of a compact radio core. AGNs are found in at least 6 of 13 objects in their sample and AGN fraction becomes higher for more infrared luminous samples. Most of such elusive AGNs are found to be Compton-thick. Brightman and Nandra (2011a) found clear evidence for AGNs in four H II-like objects in the 12  $\mu\text{m}$  selected sample. Two of them (Arp 299 and ESO 148–IG002) are Compton-thick. Our results, together with these previous findings, demonstrate the efficacy of a combination of infrared and X-ray selection to find hidden AGNs in galaxies with significant star for-

mation activity.

We examined infrared color ( $F_{18}/F_{90}$ ) for the elusive AGNs in the 18 and 90  $\mu\text{m}$  sample. The  $F_{18}/F_{90}$  ratios are in the range from 0.038 to 0.067. This color is typical for H II nuclei and much colder than usual Seyferts (Figure 11). The cold infrared color also supports that these AGNs are hidden behind star formation activity. Reliable intrinsic X-ray luminosities are available for Compton-thin objects. The logarithm of intrinsic luminosities in 2–10 keV are 41.6 and 42.3 for NGC 695 and IRAS 20551–4250, respectively. These luminosities are relatively low for Seyfert nuclei, and could be easily overwhelmed by star formation activity in optical and infrared.

## 6. SUMMARY

We cross-correlated 18 and 90  $\mu\text{m}$  sources in the *AKARIPSC* and X-ray sources in the 2XMMi-DR3 catalog, and made a sample of infrared/X-ray-selected galaxies. As the parent sample of X-ray sources, we used objects located at  $|b| > 10^\circ$  and with EPIC-PN counts in 0.2–12 keV greater than 60 counts (60851 unique sources). Infrared sources at  $|b| > 10^\circ$  with reliable flux measurements at 18  $\mu\text{m}$  and/or 90  $\mu\text{m}$  (FQUAL=3) are used. There are 43865 and 62326 18 and 90  $\mu\text{m}$  sources, respectively, satisfying these criteria. The matched sample combining 18, 90  $\mu\text{m}$ , and X-ray sources consist of 173 objects. Most of them are at a low redshift; the highest redshifts is 0.31 and 90% of objects are at a redshift smaller than 0.05.

The sample was divided into various activity classes and groups of various absorption column densities derived from X-ray spectra. Diagnostic diagrams using X-ray hardness (HR4) and X-ray CR to infrared flux density ratios were made using 173 objects in the matched sample of 18  $\mu\text{m}$ , 90  $\mu\text{m}$ , and X-ray sources. AGNs obscured by a column density greater than  $10^{23} \text{ cm}^{-2}$  are located in the lower right part of the diagrams HR4 versus  $\text{CR}_{0.2-12}/F_{18}$  and HR4 versus  $\text{CR}_{0.2-12}/F_{90}$ . We selected objects in the region  $\text{HR4} > -0.1$  and  $\text{CR}_{0.2-12}/F_{90} < 0.1$  without published X-ray results to search for obscured AGNs. An object not detected in the 90  $\mu\text{m}$  band and having  $\text{HR4} > -0.1$  and  $\text{CR}_{0.2-12}/F_{18} < 1$  was also selected as a candidate obscured AGN. We analyzed X-ray spectra of 48 objects in total after excluding Galactic sources, sources in complex fields, or sources with very low X-ray counts after data screening.

X-ray spectra of 26 among the 48 objects (54%) show clear evidence for the presence of absorbed AGNs. 16 objects (33%) show a continuum absorbed by a column density ranging from  $3 \times 10^{22} \text{ cm}^{-2}$  to  $1.4 \times 10^{24} \text{ cm}^{-2}$ . Six objects (13%) show a strong Fe-K emission line and a flat continuum, indicating the presence of a Compton-thick AGN. The spectra of four objects are explained by either Compton-thin or Compton-thick AGN. 22 objects (46%) show no clear evidence for the presence of an obscured AGN. These objects are either very faint in hard X-rays or hardness ratio is modest ( $\text{HR4} \approx 0$ ).

Reliable constraints on X-ray absorption are available for 151 among 179 objects, satisfying the conditions  $\text{HR4} > -0.1$  and ( $\text{CR}_{0.2-12}/F_{18} < 1$  or  $\text{CR}_{0.2-12}/F_{90} < 0.1$ ). 113 objects show clear evidence for the presence of absorbed AGNs, resulting in the success rate of 75%. If only objects satisfying the 18  $\mu\text{m}$  condition are used, the

detection rate of absorbed AGN becomes 92%.

At least seven objects with an optical classification of an H II nucleus show evidence for the presence of obscured AGNs, four of which are reported for the first time in this paper. These “optically elusive” AGNs have cold infrared color ( $F_{18}/F_{90}$ ) typical for H II nuclei. Their optical classifications and infrared colors are consistent with the idea that the star formation activity overwhelms their AGN in the optical and infrared wavelengths.

The authors thank an anonymous referee for constructive comments that improved the clarity of the paper. This research is based on observations obtained with *XMM-Newton*, an ESA science mission with instruments and contributions directly funded by ESA Member States and NASA, and *AKARI*, a JAXA project with the participation of ESA. This research made use of the NASA/IPAC Extragalactic Database (NED) which is operated by the Jet Propulsion Laboratory, California Institute of Technology, under contract with the National Aeronautics and Space Administration, and the HyperLeda database (<http://leda.univ-lyon1.fr>).

Facilities: *XMM-Newton*, *AKARI*

## REFERENCES

- Adams, T. F., & Weedman, D. W. 1975, *ApJ*, 199, 19
- Afonso, J., et al. 2005, *ApJ*, 624, 135
- Akylas, A., & Georgantopoulos, I. 2009, *A&A*, 500, 999
- Alexander, D. M., & Hickox, R. C. 2012, *New AR*, 56, 93
- Awaki, H., Anabuki, N., Fukazawa, Y., et al. 2008, *PASJ*, 60, S293
- Awaki, H., Koyama, K., Inoue, H., & Halpern, J. 1991, *PASJ*, 43, 195
- Awaki, H., Terashima, Y., Higaki, Y., & Fukazawa, Y. 2009, *PASJ*, 61, S317
- Baan, W. A., Salzer, J. J., & Lewinter, R. D. 1998, *ApJ*, 509, 633
- Baldwin, J. A., Phillips, M. M., & Terlevich, R. 1981, *PASP*, 93, 5
- Benedict, G. F., McArthur, B. E., Feast, M. W., et al. 2009, *AJ*, 133, 1810
- Bettoni, D., & Buson, L. M. 1987, *A&AS*, 67, 341
- Boller, Th., Trümper, J., Molendi, S., et al. 1993, *A&A*, 279, 53
- Bose, S., & Kumar, B. 2014, *ApJ*, 782, 98
- Brightman, M., & Nandra, K. 2011a, *MNRAS*, 413, 1206
- Brightman, M., & Nandra, K. 2011b, *MNRAS*, 414, 3084
- Buchanan, C. L., McGregor, P. J., Bicknell, G. V., & Dopita, M. A. 2006, *AJ*, 132, 27
- Burlon, D., Ajello, M., Greiner, J., et al. 2011, *ApJ*, 728, 58
- Buttiglione, S., et al. 2009, *A&A*, 495, 1033
- Cappi, M., et al. 2006, *A&A*, 446, 459
- Cash, W. 1979, *ApJ*, 228, 939
- Churazov, E., Forman, W., Jones, C., & Böhringer, H. 2003, *ApJ*, 590, 225
- Comastri, A. 2004, in “Supermassive Black Holes in the Distant Universe”, Ed. A. J. Berger (Kluwer Academic), 245
- Corbett, E. A., Kewley, L., Appleton, P. N., et al. 2003, *ApJ*, 583, 670
- Corral, A. et al. 2011, *A&A*, 530, A42
- Cortes, J. R., Kenney, J. D. P., & Hardy, E. 2008, *ApJ*, 683, 78
- Coziol, R., Brinks, E., & Bravo-Alfaro, H. 2004, *AJ*, 128, 68
- Coziol, R., Demers, S., Pena, M., & Barneoud, R. 1994, *AJ*, 108, 405
- Coziol, R., Iovino, A., & de Carvalho, R. R. 2000, *ApJ*, 120, 47
- Dalcanton, J. J., Williams, B. F., Seth, A. C., et al. 2009, *ApJS*, 183, 67
- de Grijp, M. H. K., Keel, W. C., Miley, G. K., Goudfrooij, P., & Lub, J. 1992, *A&AS*, 96, 389
- Della Ceca, R., Ballo, L., Tavecchio, F., et al. 2002, *ApJ*, 581, L9
- De Rosa, A., Bassani, L., Ubertini, P., et al. 2008, *A&A*, 483, 749
- De Rosa, A., Panessa, F., Bassani, L., et al. 2012, *MNRAS*, 420, 2087
- Djorgovski, S., de Carvalho, R. R., & Thompson, D. J. 1990, *AJ*, 99, 1414
- Eguchi, S., et al. 2011, *ApJ*, 729, 31
- Ekhholm, T., Lanoix, P., Teerikorpi, P., Fouqué, P., & Paturel, G. 2000, *A&A*, 355, 835
- Evans, D. A., Lee, J. C., Turner, T. J., Weaver, K. A., & Marshall, H. L. 2007, *ApJ*, 671, 1345
- Fabian, A. C. 2004, in *Carnegie Observatories Astrophysics Series, Vol. 1: Coevolution of Black Holes and Galaxies*, ed. L. C. Ho (Cambridge: Cambridge Univ. Press), 446
- Fabian, A. C., Kara, E., Walton, D. J., et al. 2013, *MNRAS*, 429, 291
- Falco, E. E., et al. 1999, *PASP*, 111, 438
- Fiore, F., Grazian, A., Santini, P., et al. 2008, *ApJ*, 672, 94
- Fiore, F., Puccetti, S., Brusa, M., et al. 2009, *ApJ*, 693, 447
- Franceschini, A., Braito, V., Persic, M., et al. 2003, *MNRAS*, 343, 1181
- Fraquelli, H. A., Storchi-Bergmann, T., Binette, L., & 2000, *ApJ*, 532, 867
- Fukazawa, Y., Hiragi, K., Mizuno, M., et al. 2011, *ApJ*, 727, 19
- Gallo, L. C., Lehmann, I., Pietsch, W., et al. 2006, *MNRAS*, 365, 688
- García-Marín, M., Colina, L., Arribas, S., Alonso-Herrero, A., & Mediavilla, E. 2006, *ApJ*, 650, 850
- Gandhi, P., Horst, H., Smette, A., et al. 2009, *A&A*, 502, 457
- Ghisellini, G., Haardt, F., & Matt, G. 1994, *MNRAS*, 267, 743
- Gilli, R., Comastri, A., & Hasinger, G. 2007, *A&A*, 463, 79
- Gilmour, R., Best, P., & Almaini, O. 2009, *MNRAS*, 392, 1509
- Gonçalves, A. C., Véron-Cetty, M.-P., & Véron, P. 1999, *A&AS*, 135, 437
- González-Martín, O., Masegosa, J., Márquez, I., Guainazzi, M., & Jiménez-Bailón, E. 2009, *A&A*, 506, 1107
- Greene, J. E., Peng, C. Y., Kim, M., et al. 2010, *ApJ*, 721, 26
- Greenhill, L. J., Tilak, A., & Madejski, G. 2008, *ApJ*, 686, L13
- Greenhill, L. J., Ellingsen, S. P., Norris, R. P., et al. 2002, *ApJ*, 565, 836
- Guainazzi, M., Matt, G., & Perola, G. C. 2005a, *A&A*, 444, 119
- Guainazzi, M., Piconcelli, E., Jiménez-Bailón, E., & Matt, G. 2005b, *A&A*, 429, L9
- Guainazzi, M., Rodríguez-Pascual, P., Fabian, A. C., Iwasawa, K., & Matt, G. 2004, *MNRAS*, 355, 297
- Harrison, F. A., Eckart, M. E., Mao, P. H., Helfand, D. J., & Stern, D. 2003, *ApJ*, 596, 944
- Hiroi, K., Ueda, Y., Hayashida, M., et al. 2013, *ApJS*, 207, 36
- Ho, L. C., Filippenko, A. V., & Sargent, W. L. W. 1997, *ApJS*, 112, 315
- Hopkins, P. F., Hernquist, L., Cox, T. J., et al. 2006, *ApJS*, 163, 1
- Horst, H., Gandhi, P., Smette, A., & Duschl, W. J. 2008, *A&A*, 479, 389
- Huchra, J. P., Wyatt, W. F., & Davis, M. 1982, *AJ*, 87, 1628
- Hudaverdi, M., Kunieda, H., Tanaka, T., et al. 2006, *PASJ*, 58, 931
- Hunt, L. K., & Malkan, M. A. 2004, *ApJ*, 616, 707
- Ichikawa, K., Ueda, Y., Terashima, Y., et al. 2012, *ApJ*, 754, 45
- Ikeda, S., Awaki, H., & Terashima, Y. 2009, *ApJ*, 692, 608
- Ishihara, D., Onaka, T., Kataza, H., et al. 2010, *A&A*, 514, A1
- Izotov, Y. I., Dyak, A. B., Chaffe, F. H., et al. 1996, *ApJ*, 458, 524
- Iwasawa, K., Koyama, K., Awaki, H., et al. 1993, *ApJ*, 409, 155
- Iwasawa, K., & Comastri, A. 1998, *MNRAS*, 297, 1219
- Jacobs, B. A., Rizzi, L., Tully, R. B., et al. 2009, *AJ*, 138, 332
- Jenkins, L. P., Roberts, T. P., Ward, M. J., & Zezas, A. 2005, *MNRAS*, 357, 109
- Jensen, J. B., Tonry, J. L., Barris, B. J., et al. 2003, *ApJ*, 583, 712
- Jiménez-Bailón, E., Loiseau, N., Guainazzi, M., et al. 2007, *A&A*, 469, 881
- Kalberla, P. M. W., Burton, W. B., Hartmann, D., et al. 2005, *A&A*, 440, 775
- Kawada, M., Baba, H., Barthel, P. D., et al. 2007, *PASJ*, 59, S389
- Keel, W. C., Kennicutt, R. C., Jr., Hummel, E., & van der Hulst, J. M. 1985, *AJ*, 90, 708
- Kewley, L. J., Groves, B., Kauffmann, G., & Heckman, T. 2006, *MNRAS*, 372, 961
- Kewley, L. J., Heisler, C. A., Dopita, M. A., & Lumsden, S. 2001, *ApJS*, 132, 37
- LaMassa, S. M., Heckman, T. M., Ptak, A., et al. 2009, *ApJ*, 705, 568
- LaMassa, S. M., Yaqoob, T., Ptak, A. F., et al. 2014, *ApJ*, 787, 61
- Landi, R., Masetti, N., Morelli, L., et al. 2007, *ApJ*, 669, 109

- Leahy, D. A., & Creighton, J. 1993, MNRAS, 263, 314
- Levenson, N. A., Heckman, T. M., Krolik, J. H., Weaver, K. A., & Życki, P. T. 2006, ApJ, 648, 111
- Lewis, K. T., Sambruna, R. M., Angelakis, E., et al. 2011, AJ, 142, 9
- Lipari, S., Tsvetanov, Z., & Macchetto, F. 1997, ApJS, 111, 369
- Maia, M. A. G., Machado, R. S., & Willmer, C. N. A. 2003, AJ, 126, 1750
- Maiolino, R., Comastri, A., Gilli, R., et al. 2003, MNRAS, 344, L59
- Magdziarz, P., & Zdziarski, A. A. 1995, MNRAS, 273, 837
- Malizia, A., Landi, R., Bassani, L., et al. 2007, ApJ, 668, 81
- Markowitz, A., Takahashi, T., Watanabe, S., et al. 2007, ApJ, 665, 209
- Martínez, M. A., Del Olmo, A., Cozoi, R., & Perea, J. 2010, AJ, 139, 1199
- Mateos, S., Alonso-Herrero, A., Carrera, F. J., et al. 2012, MNRAS, 426, 3271
- Matsuta, K., Gandhi, P., Dotani, T., et al. 2012, ApJ, 753, 104
- Matt, G., Bianchi, S., D'Ammando, F., & Martocchia, A. 2004, A&A, 421, 473
- Mauch, T., & Sadler, E. M. 2007, MNRAS, 375, 931
- Masetti, N., Mason, E., Morelli, L., et al. 2008, A&A, 482, 113
- Masetti, N., Pretorius, M. L., Plazzi, E., et al. 2006, A&A, 449, 1139
- McQuinn, K. B. W., Skillman, E. D., Cannon, J. M., et al. 2010, ApJ, 721, 297
- Miller, P., Rawlings, S., Saunders, R., & Eales, S. 1992, MNRAS, 254, 93
- Moran, E. C., Halpern, J. P., & Helfand, D. J. 1996, ApJS, 106, 341
- Morris, S. L., & Ward, M. J. 1988, MNRAS, 230, 639
- Mouhcine, M., Ferguson, H. C., Rich, R. M., Brown, T. M., & Smith, T. E. 2005, ApJ, 633, 810
- Murakami, H., Baba, H., Barthel, P., et al. 2007, PASJ, 59, S369
- Murayama, T., Taniguchi, Y., & Iwasawa, K. 1998, AJ, 115, 460
- Murphy, K. D., & Yaqoob, T. 2009, MNRAS, 397, 1549
- Nandra, K., & Iwasawa, K. 2007, MNRAS, 382, 1
- Noguchi, K., Terashima, Y., & Awaki, H. 2009, ApJ, 705, 454
- Onaka, T., Matsuhara, H., Wada, T., et al. 2007, PASJ, 59, S401
- Osterbrock, D. E., & Phillips, M. M. 1977, PASP, 89, 251
- Panessa, F., Bassani, L., De Rosa, A. et al. 2008, A&A, 483, 151
- Panessa, F., Wolter, A., Pellegrini, S., et al. 2005, ApJ, 631, 707
- Parisi, P., Masetti, N., Jiménez-Bailón, E., et al. 2012, A&A, 545, A101
- Parodi, B. R., Saha, A., Sandage, A. & Tammann, G. A. 2000, ApJ, 540, 634
- Pastoriza, M. G. 1979, ApJ, 234, 837
- Patrick, A. R., Reeves, J. N., Porquet, D., et al. 2012, MNRAS, 426, 2522
- Paturel, G., Petit, C., Prugniel, Ph., et al. 2003, A&A, 412, 45
- Pereira-Santaella, M., Alonso-Herrero, A., Santos-Lleo, M., et al. 2011, A&A, 535, A93
- Pfefferkorn, F., Boller, Th., & Rafanelli, P. 2001, A&A, 368, 797
- Phillips, M. M., Feldman, F. R., Marshall, F. E., & Wamsteker, W. 1979, A&A, 76, L14
- Piconcelli, E., Bianchi, S., Miniutti, G., et al. 2008, A&A, 480, 671
- Piconcelli, E., Fiore, F., Nicastro, F., et al. 2007, A&A, 466, 855
- Pietsch, W., Bischoff, K., Boller, Th., et al. 1998, A&A, 333, 48
- Poletta, M., Tajer, M., Maraschi, L., et al. 2007, ApJ, 663, 81
- Ponti, G., Gallo, L. C., Fabian, A. C., et al. 2010, MNRAS, 406, 2591
- Pounds, K. A., Reeves, J. N., King, A. R., & Page, K. L. 2004, MNRAS, 350, 10
- Prieto, A., Vitores, A., Wamsteker, W., et al. 1986, A&A, 168, 253
- Rasmussen, J., Bai, L., Ponman, T. J., et al. 2012, ApJ, 747, 31
- Ricci, C., Beckmann, V., Audard, M., & Courvoisier, T. J.-L. 2010, A&A, 518, A47
- Ricci, C., et al. 2014, ApJ, 795, 147
- Ricci, T. V., Steiner, J. E., & Menezes, R. B. 2014, MNRAS, 440, 2442
- Rivers, E., Markowitz, A., Rothschild, R., et al. 2014, ApJ, 786
- Rodriguez, J., Tomsick, J. A., & Bodaghee, A. 2010, A&A, 517, 14
- Rovilos, E., Georgantopoulos, I., Akylas, A., et al. 2014, MNRAS, 438, 494
- Ruiz, A., Carrera, F. J., & Panessa, F. 2007, A&A, 471, 775
- Saez, C., Brandt, W. N., Gallagher, S. C., et al. 2012, ApJ, 759, 42
- Sanders, D. B., Soifer, B. T., Elias, J. H., et al., 1988, ApJ, 328, L35
- Sargent, W. L. W. 1972, ApJ, 173, 7
- Schulz, R., Encrenaz, T., Stuewe, J. J., et al. 1994, A&A, 288, 425
- Seta, H., Isobe, N., Tashiro, M. S., et al. 2009, PASJ, 61, 1011
- Severgnini, P., Caccianiga, A., & Della Ceca, R. 2012, A&A, 542, A46
- Shu, X. W., Yaqoob, T., & Wang, J. X. 2011, ApJ, 738, 147
- Shuder, J. M. 1980, ApJ, 240, 32
- Shuder, J. M., & Osterbrock, D. E. 1981, ApJ, 250, 55
- Singh, V., Shastri, P., & Risaliti, G. 2011, A&A, 532, A84
- Smith, R. K., Brickhouse, N. S., Liedahl, D. A., & Raymond, J., C. 2001, ApJ, 556, L91
- Springob, C. M., Masters, K. L., Haynes, M. P., Giovanelli, R., & Marinoni, C. 2009, ApJS, 182, 474
- Storchi-Bergmann, Th., Bica, E., Kinney, A., & Bonatto, C. 1997, MNRAS, 290, 231
- Storchi-Bergmann, Th., Kinney, A. L., & Challis, P. 1995, ApJS, 98, 103
- Sun, M., & Murray, S. S. 2002, ApJ, 577, 139
- Teng, S. H., & Veilleux, S. 2010, ApJ, 725, 1848
- Terashima, Y., Iyomoto, N., Ho, L. C., & Ptak, A. F. 2002, ApJS, 139, 1
- Terry, J. N., Paturel, G., and Ekholm, T. 2002, A&A, 393, 57
- Thornton, C. E., Barth, A. J., Ho, L. C., & Greene, J. E. 2009, ApJ, 705, 1196
- Tilak, A., Greenhill, L. J., Done, C., & Madejski, G. 2008, ApJ, 678, 701
- Trinchieri, G., Iovino, A., Pompei, E., et al. 2008, A&A, 484, 195
- Tully, R. B., Rizzi, L., Shaya, E. J., et al. 2009, AJ, 138, 323
- Ueda, Y., Ishisaki, Y., Takahashi, T., Makishima, K., & Ohashi, T. 2005, ApJS, 161, 185
- Veilleux, S., Kim, D.-C., & Sanders, D. B. 1999, ApJ, 522, 113
- Veilleux, S., Kim, D.-C., Sanders, D. B., et al. 1995, ApJS, 98, 171
- Veilleux, S., & Osterbrock, D. E. 1987, ApJS, 63, 295
- Véron-Cetty, M.-P., & Véron, P. 1986a, A&AS, 65, 241
- Véron-Cetty, M.-P., & Véron, P. 1986b, A&AS, 66, 335
- Véron-Cetty, M.-P., & Véron, P. 2001, A&A, 374, 92
- Wada, K., & Norman, C. A. 2002, ApJ, 566, L21
- Wang, J., Zhou, X. L., & Wei, J. Y. 2013, ApJ, 768, 176
- Watson, M., Schröder, A. C., Fyfe, D., et al. 2009, A&A, 493, 339
- Wilman, R. J., & Fabian, A. C. 1999, MNRAS, 309, 862
- Winter, L. M., Mushotzky, R. F., Terashima, Y., & Ueda, Y. 2009, ApJ, 701, 1644
- Winter, L. M., Veilleux, S., McKernan, B., & Kallman, T. R. 2012, ApJ, 745, 107
- Wu, P.-F., Tully, R.B., Rizzi, L. et al. 2014, AJ, 148, 7
- Wu, H., Zou, Z. L., Xia, X. Y., & Deng, Z. G. 1998, A&AS, 132, 181
- Wu, Y., Charmandaris, V., Huang, J., Spinoglio, L., & Tommasin, S. 2009, ApJ, 701, 658
- Yamamura, I., Makiuti, S., Ikeda, N., et al., 2010, VizieR On-line Data Catalog
- Yaqoob, T., Murphy, K., Miller, L., & Turner, T. J. 2010, MNRAS, 401, 411
- Yoshii, Y., Kobayashi, Y., Minezaki, T., Koshida, S., & Peterson, B. A. 2014, ApJ, 784, L11
- Zuan, T.-T., Kewley, L. J., & Sanders, D. B. 2010, ApJ, 709, 884
- Zezas, A., Ward, M. J., & Murray, S. S. 2003, ApJ, 594, L31
- Zhang, W. M., Soria, R., zhang, S. N., et al. 2009, ApJ, 699, 281

**Table 1**  
XMM + AKARI 18  $\mu\text{m}$  and 90  $\mu\text{m}$  Sample

XMM name	Other name	Redshift	CR ( $\text{s}^{-1}$ )	HR4	$F_{18}$ (Jy)	$F_{90}$ (Jy)	CR/ $F_{18}$	CR/ $F_{90}$	Class	Ref	$N_{\text{H}}$ ( $10^{22} \text{ cm}^{-2}$ )	X-ray Class	Ref
(1)	(2)	(3)	(4)	(5)	(6)	(7)	(8)	(9)	(10)	(11)	(12)	(13)	(14)
2XMM J004847.1+315724	NGC 262/Mrk 348	0.0150	2.389	0.402	0.593	0.736	4.031	3.2486	Sy2	1	$13.1^{+0.7}_{-1.3}$	Thin	1
2XMMi J005329.8–084604	NGC 291	0.0190	0.034	0.522	0.204	3.135	0.166	0.0108	Sy2	2	$>100^b$	Thick	2
2XMM J005334.9+124136	Mrk 1502	0.0589	8.677	–0.512	0.714	1.964	12.144	4.4174	Sy1	1	$\dots^a$	Un	1
2XMMi J005356.2–703804	IRAS 00521–7054	0.0689	0.281	0.013	0.595	0.635	0.472	0.4431	Sy2	1	$7.2\pm 0.3$	Thin	3
2XMM J010516.8–582615	ESO 113–G010	0.0257	4.071	–0.416	0.207	1.460	19.663	2.7877	Sy1.8	3	$<0.0072$	Un	4
2XMM J011127.5–380500	NGC 424	0.0118	0.411	0.463	1.293	1.181	0.318	0.3481	Sy1.8	4	$199^{+32}_{-40}$	Thick	5
2XMM J011607.1+330522	NGC 449/Mrk 1	0.0159	0.097	–0.101	0.531	1.395	0.183	0.0698	Sy2	1	$>100^b$	Thick	6
2XMM J012732.4+191044	Mrk 359	0.0174	5.229	–0.342	0.187	1.282	27.917	4.0794	Sy1	1	$\dots^a$	Un	7
2XMM J013331.1+354006	NGC 591/Mrk 1157	0.0152	0.108	0.370	0.226	2.024	0.479	0.0536	Sy2	5	$>100^b$	Thick	8
2XMMi J013805.3–125210	IRAS 01356–1307	0.0402	0.068	0.064	0.291	0.860	0.234	0.0790	Sy2	1	$\dots$	$\dots$	$\dots$
2XMM J014357.7+022059	Mrk 573	0.0172	0.406	0.206	0.545	1.059	0.744	0.3833	Sy2	1	$>100^b$	Thick	8
2XMM J015002.6–072548	IRAS 01475–0740	0.0177	0.318	–0.446	0.408	0.784	0.779	0.4050	Sy2	1	$0.211^{+0.055}_{-0.006}$	Un	1

**References.** — Optical classification: (1) de Grijp et al. 1992; (2) Kewley et al. 2001; (3) Pietsch et al. 1998; (4) Murayama et al. 1998; (5) Veilleux & Osterbrock 1987; (6) Veilleux et al. 1999; (7) Ho et al. 1997; (8) Veilleux et al. 1995; (9) Gonçalves et al. 1999; (10) Shuder & Osterbrock 1981; (11) Schulz et al. 1994; (12) Yuan et al. 2010; (13) Adams & Weedman 1975; (14) Wu et al. 1998; (15) Shuder 1980; (16) Prieto et al. 1986; (17) Maia et al. 2003; (18) Masetti et al. 2006; (19) Miller et al. 1992; (20) Landi et al. 2007; (21) Boller et al. 1993; (22) Gallo et al. 2006; (23) Pastoriza 1979 ; (24) Masetti et al. 2008; (25) Buchanan et al. 2006; (26) Moran et al. 1996 ; (27) Phillips et al. 1979; (28) Véron-Cetty & Véron 1986a ; (29) Véron-Cetty & Véron 1986b ; (30) Morris & Ward 1988 ; (31) Huchra et al. 1982 ; (32) Brightman & Nandra 2011b; (33) Coziol et al. 2000; (34) Burlon et al. 2011; (35) Martínez et al. 2010; (36) Djorgovski et al. 1990; (37) 6dF; (38) Pereira-Santaella et al. 2011; (39) Sargent 1972; (40) Keel et al. 1985; (41) Storchi-Bergmann et al. 1995; (42) Baan et al. 1998; (43) García-Marín et al. 2006; (44) Corbett et al. 2003; (45) Izotov et al. 1996;  
X-ray: (1) Brightman & Nandra 2011a; (2) LaMassa et al. 2009; (3) Ricci et al. 2014a; (4) Gallo et al. 2006; (5) Burlon et al. 2011; (6) Singh et al. 2011; (7) Fukazawa et al. 2011 (8) Guainazzi et al. 2005a; (9) Teng & Veilleux 2010; (10) Winter et al. 2009; (11) Severgnini et al. 2012; (12) Churazov et al. 2003; (13) Pfefferkorn et al. 2001; (14) Evans et al. 2007; (15) Awaki et al. 2008; (16) Awaki et al. 2009; (17) Panessa et al. 2008; (18) Saez et al. 2012; (19) Maiolino et al. 2003; (20) Tilak et al. 2008; (21) Greenhill et al. 2008; (22) Malizia et al. 2007; (23) LaMassa et al. 2014; (24) Pounds et al. 2004; (25) González-Martín et al. 2009; (26) Terashima et al. 2002; (27) Fabian et al. 2013; (28) Noguchi et al. 2009; (29) Rodríguez et al. 2010; (30) Guainazzi et al. 2004; (31) De Rosa et al. 2008; (32) Hiroi et al. 2013; PKS1549-79 (33) Ricci et al. 2010; (34) Piconcelli et al. 2007; (35) Singh et al. 2011; (36) Pereira-Santaella et al. 2011; (37) Trinchieri et al. 2008 (38) Jiménez-Bailón et al. 2007; (39) Franceschini et al. 2003; (40) Panessa et al. 2005; (41) Della Ceca et al. 2002; (42) Seta et al. 2009;

**Note.** — Column 1: XMM name; Column 2: Alternative name; Column 3: Redshift; Column 4: EPIC-PN count rate in the 0.2–12 keV band; Column 5: Hardness ratio HR4; Column 6: Flux density at 18  $\mu\text{m}$  in units of Jy; Column 7: Flux density at 90  $\mu\text{m}$  in units of Jy; Column 8: EPIC-PN count rate in 0.2–12 keV to 18  $\mu\text{m}$  flux density ratio; Column 9: EPIC-PN count rate in 0.2–12 keV to 90  $\mu\text{m}$  flux density ratio; Column 10: Optical classification. Sy — Seyfert, L — LINER, T — transition object, HII — HII nucleus, BL Lac — BL Lac object, Unclass — unclassified, 1 — type 1, 2 — type 2, and a fractional number denotes intermediate types; Column 11: Reference for optical classification; Column 12: Absorption column density in units of  $10^{22} \text{ cm}^{-2}$ ; Column 13: Classification of absorption measured with X-ray. Un — unabsorbed or slightly absorbed ( $N_{\text{H}} < 10^{22} \text{ cm}^{-2}$ ), Thin — Compton-thin ( $N_{\text{H}} = 10^{22} - 1.5 \times 10^{24} \text{ cm}^{-2}$ ), Thick — Compton-thick ( $N_{\text{H}} > 1.5 \times 10^{24} \text{ cm}^{-2}$ ). If only lower limit of  $N_{\text{H}} = 10^{24} \text{ cm}^{-2}$  is obtained, such objects are regarded as Compton-thick; Column 14: Reference for absorption column density.

<sup>a</sup> X-ray spectrum shows no evidence for significant absorption.

<sup>b</sup> Compton-thick candidates judged from a large Fe-K line EW ( $> 700 \text{ eV}$ ) and/or flat continuum.

<sup>c</sup> There are two IRC sources corresponding to NGC 3690E and NGC 3690W. The nucleus of NGC 3690W is likely to be an obscured AGN (Zezas et al. 2003), and the 18 $\mu\text{m}$  flux of NGC 3690W is shown. FIS does not resolve the two sources and the 90 $\mu\text{m}$  flux is for the single FIS source.

<sup>d</sup> Compton thin candidates in Severgnini et al. (2012).

(This table is available in its entirety in a machine-readable form in the online journal. A portion is shown here for guidance regarding its form and content.)



**Table 2**  
X-ray and infrared luminosities.

Name	$\log L_X$	Ref	$\log \nu L_\nu$ (18 $\mu\text{m}$ )	$\log \nu L_\nu$ (90 $\mu\text{m}$ )	Note	Ref
(1)	(2)	(3)	(4)	(5)	(6)	(7)
NGC 262/Mrk 348	43.149	...	43.702	43.092	...	...
NGC 291	41.007	...	43.447	43.929	...	...
Mrk 1502	43.599	...	45.009	44.733	...	...
IRAS 00521-7054	43.408	...	45.074	44.384	...	...
ESO 113-G010	42.580	...	43.722	43.864	...	...
NGC 424	41.398	...	43.829	43.087	...	...
NGC 449/Mrk 1	40.659	...	43.705	43.421	...	...
Mrk 359	40.542	...	43.332	43.464	...	...
NGC 591/Mrk 1157	41.013	...	43.294	43.543	...	...
IRAS 01356-1307	...	...	44.271	44.031	...	...
Mrk 573	41.267	...	43.786	43.371	...	...
IRAS 01475-0740	41.737	...	43.686	43.265	...	...

**References.** — X-ray — (1) De Rosa et al. 2012; (2) Brightman & Nandra 2011a; (3) Rivers et al. 2014; (4) Patrick et al. 2012; (5) Corral et al. 2011; (6) Ueda et al. 2005; (7) Malizia et al. 2007; (8) Levenson et al. 2006; (9) Winter et al. 2012; (10) Matt et al. 2004; (11) Ponti et al. 2010; (12) Teng et al. 2010; (13) This work; (14) Harrison et al. 2003; (15) Akylas & Gergatopoulos 2009; (16) Shu et al. 2011; (17) Markowitz et al. 2007; Distance — (1) Jensen et al. 2003; (2) Yoshii et al. 2014; (3) Ekholm et al. 2000; (4) Bose & Kumar 2014; (5) Springob et al. 2009; (6) Cortes et al. 2008; (7) Wu et al. 2014; (8) Terry et al. 2002; (9) Dalcanton et al. 2009; (10) Parodi et al. 2000; (11) Jacobs et al. 2009; (12) McQuinn et al. 2010; (13) Takats et al. 2012; (14) Tully et al. 2009; (15) Benedict et al. 2009; (16) Mouhcine et al. 2005

**Note.** — Column 1: Name; Column 2: Logarithm of observed X-ray luminosity in the 2–10 keV band; Column 3: Reference for X-ray luminosity; Column 4: Logarithm of  $\nu L_\nu$  at 18  $\mu\text{m}$ ; Column 5: Logarithm of  $\nu L_\nu$  at 90  $\mu\text{m}$ ; Column 6: Distance of nearby objects used to calculate luminosities. Column 7: Reference for distance.

<sup>a</sup> X-ray spectra are analyzed in this paper, and no clear evidence for the presence of an obscured AGN is found.

(This table is available in its entirety in a machine-readable form in the online journal. A portion is shown here for guidance regarding its form and content.)

**Table 3**  
XMM + AKARI 90  $\mu$ m Sample

XMM name	Other name	Redshift	CR	HR4	$F_{90}$	CR/ $F_{90}$	Class	Ref	$N_{\text{H}}$ ( $10^{22}$ cm $^{-2}$ )	X-ray Class	Ref
(1)	(2)	(3)	(4)	(5)	(6)	(7)	(8)	(9)	(10)	(11)	(12)
2XMM J001106.5–120626	NGC 17/NGC 34/Mrk 938	0.0196	0.087	0.255	17.041	0.005103	Sy2	1	47.0 $^{+30.4}_{-21.2}$	Thin	1
2XMM J001110.4–120114	NGC 35	0.0199	0.016	0.517	1.647	0.009424	Sy1	2	...	...	...
2XMM J002034.9–705526	IRAS 00182–7112	0.327	0.025	0.145	1.064	0.023476	Sy2/L	3	>100 <sup>a</sup>	Thick	2
2XMM J004128.0+252958	NGC 214	0.0151	0.037	0.224	3.261	0.011204	Sy2/L	4	17.3 $^{+13.1}_{-8.0}$	Thin	1
2XMM J012445.0+320957	UGC 959/Mrk 991	0.0351	0.040	–0.088	1.760	0.022500	Sy/L	5	...	...	...
2XMMi J013357.6–362935	NGC 612	0.0298	0.136	0.882	2.604	0.052230	Sy2	6	113 $^{+10}_{-8}$	Thin	3
2XMM J051109.0–342335	ESO 362–G008	0.0157	0.059	0.436	0.671	0.088454	Sy2	7	>100 <sup>b</sup>	Thick	4
2XMMi J081040.3+481233	2MASX J08104028+4812335	0.0776	0.007	0.451	0.614	0.011751	Sy2	8	34 $^{+21}_{-13}$	Thin	5
2XMM J081937.8+210653	UGC 4332	0.0185	0.017	0.689	1.229	0.013501	Sy2	9	... <sup>c</sup>	Un	6
2XMM J094036.4+033437	NGC 2960/Mrk 1419	0.0165	0.028	0.356	1.051	0.026780	Sy2/HII	10	>100 <sup>a</sup>	Thick	7
2XMM J101738.5+214119	NGC 3185	0.00406	0.020	0.233	2.030	0.009795	Sy2	11	<0.2	Un	8
2XMMi J103234.6+650228	NGC 3259	0.00562	0.014	0.163	1.261	0.010738	Sy1	12	4.3	Thin	9
2XMM J114503.8+195825	NGC 3861	0.0170	0.033	0.196	0.667	0.048966	Sy2/L	13	6 $^{+3}_{-2}$	Thin	10
2XMMi J114721.6+522659	Mrk 1457	0.0486	0.046	0.461	0.798	0.057386	Sy2	14	27.5 $^{+15.8}_{-9.3}$	Thin	11
2XMM J125400.8+101112	IRAS 12514+1027	0.319	0.006	0.233	0.788	0.007252	Sy2	9	40 $^{+200}_{-30}$	Thin	12
2XMMi J132348.4+431804	CGCG 218–007	0.0273	0.086	0.892	1.280	0.067179	Sy2	14	43.7 $^{+4.7}_{-7.6}$	Thin	11
2XMM J133739.8+390917	UGC 8621	0.0201	0.033	0.598	1.254	0.026568	Sy2	16	...	...	...
2XMMi J143722.1+363403	NGC 5695/Mrk 686	0.0141	0.035	–0.045	0.730	0.047974	Sy2	14	... <sup>c</sup>	Un	11
2XMM J203306.1–020128	NGC 6926	0.0196	0.079	0.203	9.982	0.007898	Sy2	1	...	...	...
2XMMi J231637.4–021951	NGC 7566	0.0265	0.044	0.693	0.624	0.070063	Sy2	18	...	...	...
2XMM J002126.4–083925	IRAS 00188–0856	0.128	0.005	0.127	2.660	0.001765	L	19	... <sup>c</sup>	Un	13
2XMM J010700.8–801828	ESO 013–G012	0.0168	0.018	–0.075	2.517	0.007030	L	20	... <sup>c</sup>	Un	7
2XMM J040234.4+714222	UGC 2916	0.0151	0.018	0.016	1.593	0.011068	L/Sy2	21	...	...	...
2XMMi J083529.1+250138	NGC 2611	0.0175	0.013	0.183	2.401	0.005347	L	13	...	...	...
2XMM J100259.0+022034	CGCG 036–024	0.0442	0.012	0.708	0.943	0.012687	L	21	...	...	...
2XMM J101805.6+214955	NGC 3190	0.00424	0.057	0.217	4.699	0.012137	L2	11	...	...	...
2XMM J103702.5–273354	NGC 3312	0.00963	0.069	0.426	1.090	0.063618	L	9	... <sup>c</sup>	Un	14
2XMM J110521.8+381402	CGCG 213–027	0.0285	0.024	0.495	1.475	0.016395	L	13	...	...	...
2XMM J115050.9+550836	NGC 3916	0.0191	0.004	0.138	0.872	0.005108	L	13	...	...	...
2XMM J135321.7+402151	NGC 5350/Mrk 1485	0.00774	0.035	0.005	2.734	0.012628	L	22	...	...	...
2XMM J150947.0+570002	NGC 5879	0.00258	0.030	0.474	3.882	0.007652	L2	11	18 $^{+18}_{-13}$	Thin	15
2XMM J033627.6–345832	NGC 1380	0.00626	0.080	0.233	1.511	0.052724	T2	23	... <sup>c</sup>	Un	16
2XMM J115348.5+521943	NGC 3953	0.00351	0.199	–0.020	3.444	0.057765	T2	11	...	...	...
2XMMi J124957.9+051841	NGC 4713	0.00218	0.002	0.014	4.872	0.000494	T2	11	...	...	...
2XMM J005656.8–011236	UGC 587	0.0500	0.030	0.410	0.738	0.041171	HII	13	...	...	...
2XMM J022536.4–050011	2MASX J02253645–0500123	0.0540	0.012	0.301	0.856	0.013848	HII	6	...	...	...
2XMMi J033930.5–183136	NGC 1402/IRAS 03372–1841	0.0143	0.026	0.034	3.285	0.007953	HII/L	24	...	...	...
2XMMi J082326.2–045455	NGC 2585	0.0229	0.012	0.612	2.237	0.005539	HII	25	...	...	...
2XMM J085312.7+162617	SDSS J085312.35+162619.4	0.0638	0.040	0.183	0.830	0.047895	HII	13	...	...	...
2XMM J102142.6+130654	IRAS 10190+1322	0.0766	0.006	–0.067	4.277	0.001427	HII	19	... <sup>c</sup>	Un	13
2XMM J103712.7–274103	NGC 3314	...	0.032	0.055	1.995	0.016232	HII	6	... <sup>c</sup>	Un	14
2XMMi J105650.9+065421	UGC 6046	0.0220	0.011	–0.049	0.617	0.017312	HII	13	...	...	...
2XMM J123653.5+275143	NGC 4559A	0.0251	0.008	0.736	0.817	0.010298	HII	13	...	...	...
2XMM J124119.3+331111	IRAS 12388+3327	0.0949	0.007	0.117	0.798	0.008567	HII	13	...	...	...
2XMMi J134651.1+074716	IRAS 13443+0802NE	0.135	0.012	0.181	1.493	0.007963	HII	19	...	...	...
2XMMi J143413.4+020908	2MASX J14341353+0209088	0.0774	0.005	–0.076	0.707	0.006451	HII	13	... <sup>c</sup>	...	...
2XMMi J222003.2–201852	2MASX J22200323–2018531	0.0514	0.011	0.429	1.025	0.010935	HII	6	...	...	...
2XMM J225653.1–363313	IC 5264	0.00647	0.018	–0.094	0.632	0.028225	HII	6	...	...	...
2XMMi J231505.7–021928	NGC 7546	0.0279	0.005	1.000	0.424	0.011167	HII	6	...	...	...
2XMM J011119.5–455556	ESO 243–G051	0.0216	0.015	0.611	1.040	0.014610	normal	27	...	...	...
2XMM J143529.6+484430	NGC 5689	0.00721	0.028	0.652	0.724	0.038658	normal	21	...	...	...

Table 3 — *Continued*

XMM name	Other name	Redshift	CR	HR4	$F_{90}$	CR/ $F_{90}$	Class	Ref	$N_{\text{H}}$ ( $10^{22} \text{ cm}^{-2}$ )	X-ray Class	Ref
(1)	(2)	(3)	(4)	(5)	(6)	(7)	(8)	(9)	(10)	(11)	(12)
2XMM J004330.4–180107	...	...	0.014	−0.044	0.367	0.037142	Unclass	...	...	...	...
2XMMi J005433.8+461239	IRAS 00517+4556	...	0.013	0.008	0.816	0.015659	Unclass	...	...	...	...
2XMM J005638.9–011740	CGCG 384–040	0.0502	0.009	0.044	1.173	0.007688	Unclass	...	...	...	...
2XMM J015253.9+360310	NGC 710	0.0205	0.051	0.138	2.152	0.023561	Unclass	...	...	...	...
2XMM J022402.5–044137	Arp 54	0.0433	0.015	0.547	0.637	0.024201	Unclass	...	...	...	...
2XMM J030843.4+405142	2MASX J03084352+4051419	...	0.018	0.709	0.470	0.037486	Unclass	...	...	...	...
2XMM J031659.6–441608	IRAS 03152–4427	0.0744	0.030	0.274	0.493	0.061670	Unclass	...	...	...	...
2XMMi J031821.9+410426	Abell 426:[BM99] 183	...	0.010	0.145	0.714	0.014358	Unclass	...	...	...	...
2XMMi J052555.5–661038	...	...	0.002	0.403	6.874	0.000221	Unclass	...	...	...	...
2XMMi J053123.9+120051	AKARI J0531228+120057	...	0.035	−0.069	1.830	0.019367	Unclass	...	...	...	...
2XMMi J053512.2–690009	...	...	0.013	−0.046	7.285	0.001829	Unclass	...	...	...	...
2XMM J054532.6–001131	CXO J054532.6–001129	...	0.005	−0.039	0.559	0.008733	Unclass	...	...	...	...
2XMMi J091836.4–121322	...	...	0.004	0.088	0.383	0.010511	Unclass	...	...	...	...
2XMM J095611.5+693805	CXO J095611.6+693803	...	0.002	0.167	6.359	0.000284	Unclass	...	...	...	...
2XMM J095653.2+694258	SDSS J095654.45+694257.6	...	0.006	0.013	4.899	0.001228	Unclass	...	...	...	...
2XMMi J095908.4+130343	CGCG 064–016	...	0.018	0.055	0.937	0.019106	Unclass	...	...	...	...
2XMMi J101815.0+731720	AKARI J1018190+731723	...	0.009	0.489	0.625	0.014765	Unclass	...	...	...	...
2XMMi J102955.2–031410	CGCG 009–061A	0.0377	0.002	0.286	0.507	0.004120	Unclass	...	...	...	...
2XMMi J104038.0–461855	ESO 264–G032	0.0228	0.011	0.537	0.474	0.022463	Unclass	...	...	...	...
2XMM J104219.6+061209	MCG +01–27–029	0.0276	0.017	0.296	1.015	0.016435	Unclass	...	...	...	...
2XMMi J115943.8–200657	2MASX J11594382–2006579	...	0.023	0.438	0.389	0.059469	Unclass	...	...	...	...
2XMM J123302.1+000016	IRAS 12304+0016	...	0.004	0.543	0.578	0.006639	Unclass	...	...	...	...
2XMMi J124721.7–411415	NGC 4696B	0.0104	0.072	0.026	0.906	0.079320	Unclass	...	...	...	...
2XMM J131459.3–163524	NGC 5037	0.00989	0.031	0.737	1.613	0.018920	Unclass	...	...	...	...
2XMM J132428.8+140533	NGC 5132	0.0244	0.027	−0.012	1.025	0.026722	Unclass	...	...	...	...
2XMMi J184540.6–630522	...	...	0.014	0.411	0.828	0.017253	Unclass	...	...	...	...
2XMM J222942.7–204607	...	...	0.025	0.015	1.375	0.018028	Unclass	...	...	...	...
2XMM J232008.9+080956	NGC 7617	0.0139	0.010	0.176	0.585	0.016701	Unclass	28	...	...	...
2XMM J232431.2+165204	UGC 12582	0.0356	0.007	0.130	0.616	0.011830	Unclass	...	...	...	...
2XMM J234044.2–115119	2MASX J23404437–1151178	...	0.004	0.812	0.496	0.007706	Unclass	...	...	...	...

**References.** — Optical — (1) Veilleux et al. 1995; (2) Coziol et al. 1994; (3) Buchanan et al. 2006; (4) Parisi et al. 2012; (5) Osterbrock & Phillips 1977; (6) 6dF Galaxy Survey; (7) Fraquelli et al. 2000; (8) Lewis et al. 2011; (9) Véron-Cetty & Véron 2001; (10) Greene et al. 2010; (11) Ho et al. 1997; (12) Thornton et al. 2009; (13) SDSS; (14) LaMassa et al. 2009; (15) Brightman & Nandra 2011b; (16) Wang et al. 2013; (17) Corbett et al. 2003; (18) Masetti et al. 2008; (19) Veilleux et al. 1999; (20) Greenhill et al. 2002; (21) Updated Zwicky catalog (22) Coziol et al. 2004; (23) Ricci et al. 2014b; (24) Kewley et al. 2001; (25) Mauch & Sadler 2007; (26) Hunt & Malkan 2004; (27) Afonso et al. 2005; (28) Bettoni & Buson 1987; X-ray — (1) Brightman & Nandra 2011a; (2) Nandra & Iwasawa 2007; (3) Eguchi et al. 2011; (4) Severgnini et al. 2012; (5) Lewis et al. 2011; (6) Rasmussen et al. 2012; (7) Greenhill et al. 2008; (8) Cappi et al. 2006; (9) Thornton et al. 2009; (10) Sun & Murray 2002; (11) LaMassa et al. 2009; (12) Ruiz et al. 2007; (13) Teng et al. 2010; (14) Hudaverdi et al. 2006; (15) Zhang et al. 2009; (16) Gilmour et al. 2009

**Note.** — Column 1: XMM name; Column 2: Alternative name; Column 3: Redshift; Column 4: EPIC-PN count rate in the 0.2–12 keV band; Column 5: Hardness ratio HR4; Column 6: Flux density at 90  $\mu\text{m}$  in units of Jy; Column 7: EPIC-PN count rate in 0.2–12 keV to 90  $\mu\text{m}$  flux density ratio; Column 8: Optical classification, Sy—Seyfert, L — LINER, T — transition object, HII — HII nucleus, normal — normal galaxy, Unclass — unclassified, 1 — type 1, 2 — type 2, and a fractional number denotes intermediate types; Column 9: Reference for optical classification; Column 10: Absorption column density in units of  $10^{22} \text{ cm}^{-2}$ ; Column 11: Classification of absorption measured with X-ray. Un — unabsorbed or slightly absorbed ( $N_{\text{H}} < 10^{22} \text{ cm}^{-2}$ ), Thin — Compton-thin ( $N_{\text{H}} = 10^{22} - 1.5 \times 10^{24} \text{ cm}^{-2}$ ), Thick — Compton-thick ( $N_{\text{H}} > 1.5 \times 10^{24} \text{ cm}^{-2}$ ). If only lower limit of  $N_{\text{H}} = 10^{24} \text{ cm}^{-2}$  is obtained, such objects are regarded as Compton-thick. Column 11: Reference for absorption column density.

<sup>a</sup> Compton-thick candidates judged from a large Fe-K line EW ( $> 700 \text{ eV}$ ) and/or flat continuum.

<sup>b</sup> Compton-thick candidates in Severgnini et al. (2012).

<sup>c</sup> X-ray spectrum shows no evidence for significant absorption.

**Table 4**  
XMM + AKARI 18 $\mu$ m Sample

XMM name	Other name	Redshift	CR (s <sup>-1</sup> )	HR4	$F_{18}$ (Jy)	CR/ $F_{18}$	Class	Ref	$N_{\text{H}}$ (10 <sup>22</sup> cm <sup>-2</sup> )	X-ray Class	Ref
(1)	(2)	(3)	(4)	(5)	(6)	(7)	(8)	(9)	(10)	(11)	(12)
2XMM J030030.5–112456	MCG –02–08–039	0.0299	0.200	0.517	0.371	10.785	Sy2	1	46.9 <sup>+13.1</sup> <sub>-11.9</sub>	Thin	1
2XMMi J100149.4+284709	3C 234	0.185	0.231	0.402	0.274	14.602	Sy1	2	36.9 <sup>+1.9</sup> <sub>-1.8</sub>	Thin	2
2XMM J113240.2+525701	HCG 056B/UGC 06527 NED03	0.0264	0.081	0.730	0.210	19.028	Sy2	3	76 <sup>+21</sup> <sub>-17</sub>	Thin	3
2XMM J121857.5+471814	NGC 4258	0.00149	0.443	0.164	0.449	8.901	Sy1.9	4	14.8 <sup>+4.3</sup> <sub>-3.3</sub>	Thin	4
2XMM J130527.3–492804	NGC 4945	0.00188	0.413	0.312	9.945	0.402	Sy2/L	5	251 <sup>+12</sup> <sub>-11</sub>	Thick	4
2XMM J132527.6–430109	NGC 5128/Centaurus A	0.00183	11.563	0.238	13.148	0.304	Sy2	6	14.1±0.7	Thin	4
2XMM J140700.4+282714	Mrk 668	0.0766	0.076	0.165	0.305	13.097	Sy1	1	>100 <sup>a</sup>	Thick	5
2XMM J224937.0–191627	MCG –03–58–007	0.0315	0.198	0.430	0.629	6.356	Sy2	1	27.5 <sup>+7.9</sup> <sub>-6.2</sub>	Thin	1
2XMM J235122.6+200548	NGC 7770	0.0137	0.030	–0.071	0.255	15.669	HII	8	... <sup>b</sup>	Un	6
2XMMi J050524.3–673435	2MASX J05052442–6734358	...	0.075	0.869	0.155	25.735	Unclass	...	...	...	...

**References.** — Optical classification — (1) de Grijp et al. 1992; (2) Buttiglione et al. 2009; (3) Coziol et al. 2004; (4) Ho et al. 1997; (5) Lipari et al. 1997; (6) Storchi-Bergmann et al. 1997; (7) Kewley et al. 2001; (8) Veilleux et al. 1995; X-ray — (1) Brightman & Nandra 2011a; (2) Piconcelli et al. 2008; (3) Guainazzi et al. 2005b; (4) Fukazawa et al. 2011; (5) Guainazzi et al. 2004; (6) Jenkins et al. 2005

**Note.** — Column 1: XMM name; Column 2: Alternative name; Column 3: Redshift Column 4: EPIC-PN count rate in the 0.2–12 keV band; Column 5: Hardness ratio HR4; Column 6: Flux density at 18  $\mu$ m in units of Jy; Column 7: EPIC-PN count rate in 0.2–12 keV to 18  $\mu$ m flux density ratio; Column 8: Optical classification. Sy — Seyfert, L — LINER, HII — HII nucleus, Unclass — unclassified, 1 — type 1, 2 — type 2, and a fractional number denotes intermediate types; Column 9: Reference for optical classification; Column 10: Absorption column density in units of 10<sup>22</sup> cm<sup>-2</sup>; Column 11: Classification of absorption measured with X-ray. Un — unabsorbed or slightly absorbed ( $N_{\text{H}} < 10^{22}$  cm<sup>-2</sup>), Thin — Compton-thin ( $N_{\text{H}} = 10^{22} - 1.5 \times 10^{24}$  cm<sup>-2</sup>), Thick — Compton-thick ( $N_{\text{H}} > 1.5 \times 10^{24}$  cm<sup>-2</sup>). If only lower limit of  $N_{\text{H}} = 10^{24}$  cm<sup>-2</sup> is obtained, such objects are regarded as Compton-thick.; Column 12: Reference for absorption column density.

<sup>a</sup> Compton-thick candidates judged from a large Fe-K line EW (> 700 eV) and/or flat continuum.

<sup>b</sup> X-ray spectrum shows no evidence for significant absorption.

**Table 5**  
Log of XMM-Newton Observations

Name	IR <sup>a</sup>	Type <sup>b</sup>	Redshift <sup>c</sup>	Galactic $N_{\text{H}}$ ( $10^{22} \text{ cm}^{-2}$ )	ObsID <sup>d</sup>	Net exposure (ksec)
NGC 35	90	Sb	0.019894	0.0220	0150480501	9.2
2XMM J004330.4–180107	90	...	...	0.0180	0112880601	9.0
IRAS 00517+4556	90	...	...	0.107	0501230301	10.4
UGC 587	90	Sbc	0.049991	0.0343	0012440101	23.4
UGC 959 (Mrk 991)	90	Sa	0.035131	0.0525	0201090401	13.6
IRAS 01356–1307	18+90	S0-a	0.040211	0.0157	0502020201	6.8
2MASX J02253645–0500123	90	...	0.053967	0.0231	0111110301	17.7
2MASX J03084352+4051419	90	...	...	0.106	0112880701	44.7
IRAS 03152–4427	90	Sc	0.074421	0.0136	0105660101	16.7
A426[BM99]183	90	...	...	0.128	0405410201	8.1
NGC 1402/IRAS 03372–1841	90	SB0	0.014333	0.0536	0404750101	26.7
2MASX J05052442–6734358	18	...	$0.0367^{+0.0070}_{-0.0067}$	0.186	0402000501	17.4
2XMMi J052555.5–661038	90	...	...	0.120	0505310101	60.2
AKARI J0531228+120057	90	...	...	0.226	0405210101	21.1
2XMMi J053512.2–690009	90	...	...	0.253	0506220101	69.0
2MASX J05391963–0726190	18+90	...	...	0.141	0503560101	35.4
2MASX J05430955–0829274	18+90	...	$0.075^{+0.017}_{-0.016}$	0.149	0503560501	37.2
CXO J054532.6–001129	90	...	...	0.191	0301600101	71.0
ESO 205–IG003	18+90	Sa	0.050468	0.0497	0554500301	34.6
NGC 2611	90	S0-a	0.017532	0.0277	0406740201	14.0
SDSS J085312.35+162619.4	90	...	0.063788	0.0251	0206340101	27.0
IC 614	18+90	Sab	0.034217	0.0376	0305800101	14.0
CGCG 009–061A	90	...	0.03770	0.036	0404840201	37.9
ESO 264–G032	90	SBa	0.022799	0.119	0401791201	10.7
MCG +01–27–029	90	Sc	0.027619	0.0258	0151390101	39.6
UGC 6046	90	SBc	0.022030	0.0283	0200530501	20.5
CGCG 213–027	90	...	0.028474	0.0191	0158970701	27.8
NGC 3953	90	SBa	0.003510	0.0186	0311791401	16.5
2MASX J11594382–2006579	90	...	...	0.0328	0555020201	20.1
NGC 4559A	90	Sa	0.025054	0.0137	0152170501	34.4
NGC 4696B	90	E-S0	0.010377	0.0872	0504360201	28.8
NGC 4713	90	SBcd	0.002183	0.0195	0503610101	52.2
IRAS 12596–1529	18+90	...	0.01592	0.036	0203391001	7.3
NGC 5037	90	Sa	0.006294	0.0517	0152360101	31.8
NGC 5132	90	SB0-a	0.024417	0.0171	0108860701	12.7
UGC 8621	90	Sa	0.020091	0.00761	0204651101	9.0
IRAS 13443+0802NE	90	...	0.135343	0.0193	0405950501	35.8
NGC 5350/Mrk 1485	90	SBbc	0.007742	0.00969	0041180401	16.3
2MASX J14341353+0209088	90	...	0.077367	0.0276	0553790301	14.7
NGC 5689	90	SB0-a	0.007205	0.0296	0110930401	2.7
2XMM J184540.6–630522	90	...	$0.188^{+0.020}_{-0.019}$	0.0688	0405380501	19.0
NGC 6926	90	SBc	0.019613	0.0772	0306050801	8.8
2XMM J222942.7–204607	90	...	...	0.0313	0125911001	10.5
IC 5264	90	Sab	0.006471	0.011	0135980201	23.9
NGC 7566	90	SBa	0.026548	0.0371	0501110101	29.3
NGC 7617	90	S0	0.013916	0.0466	0149240101	33.4
2MASX J23404437–1151178	90	...	$0.097^{+0.016}_{-0.019}$	0.0318	0152200101	40.6
NGC 7738	18+90	SBb	0.022556	0.0345	0211280101	26.9

<sup>a</sup> Infrared sample. “18+90” — 18 + 90  $\mu\text{m}$  sample, 18 — 18  $\mu\text{m}$  sample, 90 — 90  $\mu\text{m}$  sample.

<sup>b</sup> Hubble type taken from the HyperLeda.

<sup>c</sup> The redshift with errors are determined from Fe-K line.

<sup>d</sup> Observation identification number.

**Table 6**  
Results of X-ray Spectral Fits

Name	Model <sup>a</sup>	$N_{\text{H}}$ ( $10^{22}$ cm <sup>-2</sup> )	$\Gamma^{\text{b}}$	$A_{\text{pl}}$	$A_{\text{ref}}$	$kT$ (keV)	$A_{\text{apec}}$	$C/\text{dof}$	$F_{2-10}$	$L_{2-10}$	X-ray class
(1)	(2)	(3)	(4)	(5)	(6)	(7)	(8)	(9)	(10)	(11)	(12)
UGC 959/Mrk 991	zpha(zpo)	0.0	0.95	1.39	...	...	...	136.0/134	...	...	
	apec+zpha(zpo)	$2.4^{+1.9}_{-1.3}$	$1.95^{+0.95}_{-0.82}$	7.90	...	$0.74^{+0.15}_{-0.16}$	0.697	110.0/132	16.7	0.584	
IRAS 01356-1307	apec+zpha(zoo)*	$2.2^{+0.8}_{-1.4}$	1.8f	6.25	...	$0.74^{+0.14}_{-0.16}$	0.675	110.1/133	17.3	0.584	Thin
	apec+zpha(zpo+zpha(zpo))	0.0	1.8f	1.69	...	0.23	2.40	196.7/173	...	...	
	2apec+zpha(zpo+zpha(zpo))*	127	1.8f	7.26	...	...	...	...	...	...	
2MASX J03084352+4051419		0.0 (< 0.44)	1.8f	0.888	...	$0.114^{+0.036}_{-0.023}$	6.94	165.1/171	5.80	1.54	Thin
		105 (> 15)	1.8f	11.7(25.9 <sup>c</sup> )	...	$0.88^{+0.13}_{-0.15}$	1.14	...	...	...	
	apec+pha(po)	0.0	-0.43	0.0840	...	0.23	0.944	221.8/214	...	...	
	apec+pha(po)	18	1.8f	7.77	...	0.25	0.985	268.1/215	...	...	
IRAS 03152-4427	apec+pha(po+pha(po))*	0 (< 0.085)	1.8f	0.464	...	$0.12^{+0.07}_{-0.05}$	1.04	201.7/213	12.7	...	Thin
	apec+zpha(zpo)	$43^{+21}_{-14}$	1.8f	1.94	...	...	...	...	...	...	
	apec+zpha(zpo)	0.0	1.01	0.894	...	0.176	0.792	156.3/152	...	...	
	apec+zpha(zpo)	0.20	1.8f	1.92	...	0.124	1.68	170.0/153	...	...	
2MASX J05052442-6734358	apec+zpha(zpo+zpha(zpo))*	0.044 (< 0.23)	1.8f	1.28	...	$0.14 \pm 0.08$	0.839	146.4/151	13.0	5.54	Thin
	zpha(zpo+zga)	$44^{+51}_{-24}$	1.8f	12.2	...	...	...	...	...	...	
	zpha(zpo+zga)	47	0.99	30.7	...	...	...	149.5/150	...	...	
	zpha(zpo+zpha(zpo+zga))*	59	1.8f	177	...	...	...	149.9/151	...	...	
2MASX J05430955-0829274	zpha(zpo+zga)	$4^{+10}_{-3}$	1.8f	2.19	...	...	...	141.2/149	109	24.6	Thin
	zpha(zpo+zga)	$69^{+23}_{-18}$	1.8f	233	...	...	...	...	...	...	
	zpha(zpo+zga)	$12^{+14}_{-7}$	$1.0^{+1.5}_{-1.1}$	1.61	...	...	...	84.6/93	11.8	2.44	
ESO 205-IG003	zpha(zpo+zga)*	$18^{+9}_{-6}$	1.8f	7.12	...	...	...	85.4/94	10.7	3.15	Thin
	apec+zpha(zpo+zga)	23	1.51	84.4	...	0.84	0.986	264.1/174	...	...	
	apec+zpha(zpo+zpha(zpo+zga))*	0 (< 0.069)	1.8f	1.17	...	$0.80^{+0.19}_{-0.14}$	0.480	155.0/174	180	31.6	Thin
NGC 2611	apec+zpha(zpo)	$27.9^{+1.5}_{-1.4}$	1.8f	163	...	...	...	...	...	...	
	apec+zpha(zpo)	153	2.9	289	...	3.4	1.70	132.6/124	...	...	
	apec+zpha(zpo)	137	1.8f	27.0	...	3.4	1.70	132.6/125	...	...	
	apec+zpha(zpo+zpha(zpo))*	0 (< 0.051)	1.8f	0.446	...	$0.82^{+0.72}_{-0.59}$	0.0914	122.2/123	4.72	2.11	Thin
SDSS J085312.35+162619.4	apec+zpha(zpo+zga)	$140^{+150}_{-80}$	1.8f	29.7(89.8 <sup>c</sup> )	...	...	...	...	...	...	
	apec+zpha(zpo+zga)	$3.1^{+4.5}_{-2.3}$	$1.4^{+1.4}_{-1.0}$	4.88	...	$0.28^{+0.06}_{-0.06}$	0.600	177.6/187	25.2	2.86	
	apec+zpha(zpo+zga)	$4.2^{+1.4}_{-1.1}$	1.8f	9.66	...	$0.29^{+0.05}_{-0.06}$	0.604	177.8/188	23.6	3.03	
	apec+zpha(zpo+zpha(zpo))*	0.084 (< 1.0)	1.8f	0.538	...	$0.23^{+0.15}_{-0.13}$	0.386	171.2/187	24.9	3.50	Thin
CGCG 213-027	apec+zpha(zpo)	$5.3^{+1.9}_{-1.4}$	1.8f	11.0	...	...	...	...	...	...	
	apec+zpha(zpo)	28	1.8f	12.2	...	0.85	1.54	228.9/220	...	...	
	apec+zpha(zpo+zpha(zpo))*	0.0 (< 0.094)	1.8f	1.07	...	$0.80^{+0.23}_{-0.18}$	0.820	201.2/218	14.1	0.764	Thin
NGC 5037	apec+zpha(zpo)	$34^{+30}_{-17}$	1.8f	11.3	...	...	...	...	...	...	
	apec+zpha(zpo)	0.0	-1.3	0.0301	...	0.73	629	232.9/253	...	...	
	apec+zpha(zpo)	27	1.8f	14.6	...	0.78	629	249.5/254	...	...	
	apec+zpha(zpo+zpha(zpo))*	0 (< 0.082)	1.8f	0.519	...	$0.69^{+0.16}_{-0.14}$	0.328	225.3/252	18.3	0.0746	Thin
UGC 8621	apec+zpha(zpo)	$48^{+25}_{-19}$	1.8f	24.1	...	...	...	...	...	...	
	apec+zpha(zpo)	0.0	0.52	0.256	...	0.26	1.30	161.7/174	...	...	
	apec+zpha(zpo)	35	1.8f	8.91	...	0.30	1.41	182.7/175	...	...	
	apec+zpha(zpo+zpha(zpo))*	0 (< 0.060)	1.8f	0.576	...	$0.253^{+0.048}_{-0.033}$	0.960	145.2/173	8.92	0.376	Thin
IRAS 13443+0802NE	apec+zpha(zpo)	$54^{+59}_{-28}$	1.8f	11.7	...	...	...	...	...	...	
	apec+zpha(zpo)	0.0	1.36	0.334	...	0.554	0.229	172.4/200	...	...	
	apec+zpha(zpo+zpha(zpo))*	10	1.8f	0.494	...	0.50	0.186	176.9/201	...	...	
	apec+zpha(zpo+zpha(zpo))*	0.0 (< 0.070)	1.8f	0.358	...	$0.59^{+0.19}_{-0.21}$	0.208	164.7/199	2.38	1.66	Thin

T. HARASHIMA ET AL.

Table 6 — *Continued*

Name	Model <sup>a</sup>	$N_{\text{H}}$ ( $10^{22}$ cm <sup>-2</sup> )	$\Gamma^{\text{b}}$	$A_{\text{pl}}$	$A_{\text{ref}}$	$kT$ (keV)	$A_{\text{apec}}$	$C/\text{dof}$	$F_{2-10}$	$L_{2-10}$	X-ray class (12)
(1)	(2)	(3)	(4)	(5)	(6)	(7)	(8)	(9)	(10)	(11)	(12)
NGC 5689	zpha(zpo)	$13_{-8}^{+24}$	1.8f	0.899	...	...	...	...	...	...	
	zpha(zpo)	0.0	-0.098	0.250	...	...	...	66.3/55	...	...	
	zpha(zpo+zpha(zpo))*	23	1.8f	18.4	...	...	...	73.6/56	...	...	
		0 (< 0.14)	1.8f	0.377	...	...	...	52.9/54	23.0	0.0791	Thin
IC 5264	pha(zpo)	$27_{-12}^{+19}$	1.8f	19.6	...	...	...	...	...	...	
	pha(zpo)	0	1.38	0.240	...	...	...	60.4/62	...	...	
NGC 7566	apec+zpha(zpo)*	$2.7_{-1.4}^{+2.3}$	1.8f	0.807	...	$0.27_{-0.06}^{+0.11}$	0.201	48.4/61	2.24	0.00259	Thin
	apec+zpha(zpo+zga)	0.0	-0.50	0.123	...	0.28	0.936	100.5/98	...	...	
	apec+zpha(zpo+zpha(zpo+zga))*	0.0 (< 0.26)	1.8f	0.669	...	$0.25_{-0.23}^{+0.16}$	0.461	89.2/97	25.0	2.12	Thin
IRAS 00517+4556	pha(po)	$56_{-28}^{+51}$	1.8f	37.9	...	...	...	...	...	...	
	pha(ref)	0.0	0.65	0.379	...	...	...	84.5/72	...	...	
	pha(po+pha(po))	0.0	1.8f	...	70.1	...	...	105.2/73	...	...	
NGC 1402	pha(po+pha(po))	0.0 (< 0.10)	1.8f	0.434	...	...	...	78.9/71	8.34	...	
	pha(po+ref)*	$9_{-6}^{+17}$	1.8f	3.43	...	...	...	79.6/72	9.65	...	Thick
	apec+zpha(zpo+zga)	0.0 (< 0.092)	1.8f	0.382	424	...	...	141.5/163	3.61	0.0168	Thin
	apec+zpha(zpo+zga)*	$0.12$ (< 4.3)	$1.80_{-0.67}^{+0.83}$	0.724	...	$0.685_{-0.077}^{+0.089}$	0.647	141.5/163	3.61	0.0168	Thin
	apec+zpha(ref+zga)	$0.098_{-0.094}^{+0.84}$	1.8f	0.704	...	$0.685_{-0.075}^{+0.089}$	0.638	141.6/164	3.57	0.0166	Thin
2XMMi J052555.5-661038	apec+zpha(zpo+zga)	0.0	1.8f	...	23.8	0.767	0.953	172.7/164	...	...	
	apec+zpha(ref+zga)	$0.120_{-0.117}^{+0.81}$	1.8f	0.728	<8.3	$0.685_{-0.074}^{+0.089}$	0.648	141.5/164	3.63	0.0169	
	pha(po)	0.28 (< 1.9)	$0.8_{-0.8}^{+1.3}$	0.083	...	...	...	123.2/117	1.46	...	
	pha(ref)	0.0	1.8f	...	9.40	...	...	131.0/118	...	...	
2MASX J05391963-0726190	pha(po+pha(po))	$0.73_{-0.62}^{+1.04}$	1.8f	0.209	...	...	...	120.5/116	1.60	...	
	pha(po+ref)*	$44_{-31}^{+480}$	1.8f	1.26	...	...	...	122.0/117	1.43	...	Thick
	pha(po)	0.65 (< 1.8)	1.8f	0.174	4.50	...	...	95.8/90	4.62	...	
	pha(po)	0.95 (< 5.3)	$-0.1_{-1.5}^{+1.7}$	0.542	...	...	...	99.0/91	2.80	...	
	pha(ref)*	$4.9_{-2.6}^{+12.1}$	1.8f	1.16	...	...	...	96.0/91	3.86	...	Thick
IC 614	pha(po+pha(po))	$2.9_{-1.8}^{+4.0}$	1.8f	0.643	...	...	...	94.2/89	4.18	...	
	apec+zpha(zpo+zga)	$110_{-104}^{+220}$	1.8f	12.0 (27.7 <sup>c</sup> )	...	...	...	...	...	...	
	apec+zpha(zpo+zga)	0.0 (< 1.6)	$-0.37_{-0.96}^{+0.85}$	0.142	...	$0.270_{-0.048}^{+0.060}$	0.964	89.4/101	25.7	0.651	
	apec+zpha(zpo+zga)	8.9	1.8f	6.84	...	0.284	1.03	96.0/102	...	...	
2MASX J11594382-2006579	apec+zpha(zpo+zpha(zpo+zga))	0.017 (< 1.3)	1.8f	0.457	...	$0.258_{-0.066}^{+0.089}$	0.707	89.1/100	18.2	0.923	
	apec+zpha(ref+zga)*	$15_{-8}^{+26}$	1.8f	8.49	...	...	...	90.6/102	21.2	0.548	Thick
	apec+zpha(ref+zga)*	0 (< 1.2)	1.8f	...	85.9	$0.267_{-0.049}^{+0.065}$	0.951	83.4/66	6.34	...	
	apec+zpha(po)	0.0 (< 4.9)	$-0.2_{-1.0}^{+1.1}$	0.556	...	$0.147_{-0.045}^{+0.070}$	0.733	84.8/67	3.83	...	
2XMMi J184540.6-630522	apec+zpha(po)	$3.9_{-2.6}^{+7.9}$	1.8f	1.49	...	$0.164_{-0.045}^{+0.055}$	0.632	83.7/67	5.47	...	Thick?
	apec+zpha(ref)*	0 (< 2.9)	1.8f	...	27.8	$0.158_{-0.045}^{+0.057}$	0.657	61.3/55	7.39	6.51	
	zpha(zpo+zga)	0.070 (< 0.89)	$1.02_{-0.78}^{+1.29}$	0.554	...	...	...	60.8/55	8.10	7.43	Thick
NGC 6926	zpha(zpo+zga)	0.22 (< 0.93)	1.8f	0.833	17.0	...	...	93.0/89	4.41	0.038	
	apec+zpha(zpo+zga)	0.0 (< 54)	$1.3_{-3.9}^{+0.8}$	3.21	...	$1.29_{-0.35}^{+0.38}$	0.700	94.0/90	3.70	0.032	
	apec+zpha(zpo+zga)	0.0 (< 52)	1.8f	5.13	...	$1.17_{-0.24}^{+0.37}$	0.517	94.4/90	5.16	0.0445	Thick
2MASX J23404437-1151178	apec+zpha(ref+zga)*	0 (< 2.5)	1.8f	...	15.7	$1.30_{-0.17}^{+0.38}$	1.24	91.5/89	4.87	0.042	
	apec+zpha(zpo+zga)	0 (< 2.5)	1.8f	0.321	9.40	$1.22_{-0.26}^{+0.32}$	0.739	64.8/80	...	...	
	apec+zpha(zpo+zpha(zpo+zga))	3.2	1.8f	1.88	...	0.74	0.115	59.0/79	1.18	1.30	
		$74.4f^d$	1.8f	1.58	...	$0.68_{-0.24}^{+0.20}$	0.0851	...	...	...	

X-RAY AND IR SELECTION OF OBSCURED AGNS

Table 6 — Continued

Name	Model <sup>a</sup>	$N_{\text{H}}$ ( $10^{22}$ cm <sup>-2</sup> )	$\Gamma^{\text{b}}$	$A_{\text{pl}}$	$A_{\text{ref}}$	$kT$ (keV)	$A_{\text{apec}}$	$C/\text{dof}$	$F_{2-10}$	$L_{2-10}$	X-ray class
(1)	(2)	(3)	(4)	(5)	(6)	(7)	(8)	(9)	(10)	(11)	(12)
NGC 7738	apec+zpha(ref+zga)	0.0	1.8f	...	3.07	0.71	0.113	63.3/80	0.959	0.204	
	apec+zpha(zpo+ref+zga)*	0.19 (<1.90)	1.8f	0.0938	1.41	$0.68^{+0.20}_{-0.25}$	0.0860	59.8/79	0.861	0.194	Thick
	apec+zpha(zpo+zga)	0.062 (< 4.7)	$1.4^{+1.5}_{-1.3}$	0.399	...	$1.04^{+0.16}_{-0.15}$	0.821	64.8/96	3.62	0.0419	
	apec+zpha(zpo+zga)	0.16 (< 3.1)	1.8f	0.528	...	$1.03^{+0.16}_{-0.15}$	0.798	65.1/97	3.11	0.0365	
	apec+zpha(ref+zga)	0 (< 15)	1.8f	...	14.3	$1.14^{+0.15}_{-0.16}$	1.26	69.7/97	4.28	0.0485	
	apec+zpha(zpo+ref+zga)*	0 (< 2.9)	1.8f	0.439	4.87	$1.04^{+0.17}_{-0.14}$	0.824	64.8/96	3.75	0.0434	Thick
NGC 35	zpha(zpo)	0.23	4.1	1.50	...	...	...	64.7/54	...	...	
	apec	...	...	...	...	0.41	0.591	69.5/55	...	...	
	apec+zpha(zpo)*	0 (<0.83)	1.8f	0.312	...	$0.41^{+0.17}_{-0.12}$	0.380	58.3/53	1.06	0.0094	
2XMM J004330.4–180107	pha(po)*	$0.21^{+0.25}_{-0.18}$	$1.41^{+0.46}_{-0.43}$	1.31	...	...	...	101.3/111	8.32	...	
	apec	...	...	...	...	64 <sup>e</sup>	5.60	107.6/112	...	...	
UGC 587	zpha(zpo)	0.0 (<0.11)	1.8f	0.619	...	...	...	68.8/78	1.98 <sup>f</sup>	0.116 <sup>f</sup>	
	apec*	...	...	...	...	$0.95^{+0.24}_{-0.27}$	0.496	65.7/78	0.070 <sup>f</sup>	0.0050 <sup>f</sup>	
2MASX J02253645–0500123	zpha(zpo)*	0 (<0.037)	$1.98^{+0.23}_{-0.21}$	1.39	...	...	...	98.0/123	3.34	0.232	
	apec	...	...	...	...	4.7	4.35	115.8/124	...	...	
A426[BM99]183	pha(po)*	0.084 (< 0.57)	$2.3^{+2.8}_{-0.9}$	1.00	...	...	...	63.9/92	1.52	...	
	apec	...	...	...	...	$2.3^{+3.1}_{-0.7}$	1.96	62.0/93	1.18	...	
AKARI J0531228+120057	pha(po)*	0 (<0.13)	$1.83^{+0.44}_{-0.24}$	2.70	...	...	...	113.4/143	8.84	...	
	apec	...	...	...	...	$4.8^{+2.5}_{-1.4}$	8.97	110.6/143	8.59	...	
2XMMi J053512.2-690009	pha(po)*	0 (< 0.25)	$1.41^{+0.61}_{-0.39}$	0.862	...	...	...	158.7/180	5.47	...	
	apec	...	...	...	...	43 (> 6)	4.43	159.3/181	6.05	...	
CXO J054532.6–001129	pha(po)*	$0.78^{+1.11}_{-0.61}$	$1.54^{+0.92}_{-0.70}$	0.563	...	...	...	146.4/151	2.74	...	
	apec	...	...	...	...	64 <sup>e</sup>	1.59	159.3/152	...	...	
CGCG 009–061A	zpha(zpo)	0.0 (< 0.072)	1.8f	0.169	...	...	...	74.1/86	0.552 <sup>f</sup>	0.0182 <sup>f</sup>	
	apec*	...	...	...	...	$0.47^{+0.25}_{-0.26}$	0.101	71.8/86	0.0022 <sup>f</sup>	0.000081 <sup>f</sup>	
ESO 264–G032	zpha(zpo)	0.11 (< 0.83)	$2.9^{+4.5}_{-1.3}$	0.507	...	...	...	35.4/42	0.352	0.00438	
	apec	...	...	...	...	$2.6^{+4.2}_{-1.1}$	0.854	35.0/43	0.520	0.00646	
	apec+zpha(zpo)*	0.18 (<2.2)	1.8f	0.228	...	$0.30^{+0.63}_{-0.12}$	0.257	33.2/41	0.746	0.00902	
MCG +01–27–029	zpha(zpo)*	$0.34^{+0.30}_{-0.22}$	$2.5^{+1.4}_{-0.9}$	2.04	...	...	...	104.5/109	2.32	0.0429	
	apec	...	...	...	...	15 (> 4.2)	3.04	110.7/110	4.27	0.0741	
UGC 6046	zpha(zpo)*	$0.25^{+0.32}_{-0.22}$	$2.9^{+1.8}_{-1.1}$	1.29	...	...	...	77.9/85	0.854	0.00998	
	apec	...	...	...	...	$3.3^{+3.1}_{-1.2}$	1.64	79.7/86	1.29	0.0145	
NGC 3953	zpha(zpo)*	0.045 (< 0.17)	$1.78^{+0.65}_{-0.43}$	0.734	...	...	...	138.7/153	2.61	0.000713	
	apec	...	...	...	...	$8.7^{+23.3}_{-3.6}$	2.32	140.2/154	3.24	0.000883	
NGC 4559A	zpha(zpo)	0.0	1.8f	0.373	...	...	...	44.9/58	...	...	
	apec	...	...	...	...	$0.30^{+0.12}_{-0.07}$	0.373	42.3/58	0.0012	0.000020	
	apec+zpha(zpo)*	0 (< 26)	1.8f	0.162	...	$0.29^{+0.68}_{-0.11}$	0.244	38.7/56	0.542	0.00773	
NGC 4696B	apec+zpha(zpo)	0.008	1.8f	0.721	...	0.46	2.27	353.0/355	...	...	
	2apec+zpha(zpo)*	$1.6^{+4.0}_{-1.5}$	1.8f	0.844	...	$0.338^{+0.057}_{-0.033}$	2.36	331.2/353	2.71	0.00748	
	apec	...	...	...	...	$1.00^{+0.23}_{-0.16}$	1.01	...	...	...	
NGC 4713	zpha(zpo+zga)	0.0	2.1	0.962	...	...	...	368.0/349	...	...	
	apec	...	...	...	...	4.4	3.07	491.5/351	...	...	
IRAS 12596–1529	apec+zpha(zpo+zga)*	0.0 (<0.071)	$1.57^{+0.19}_{-0.18}$	0.581	...	$0.243^{+0.024}_{-0.023}$	0.499	318.1/347	3.08	0.000324	
	zpha(zpo)	$0.21^{+0.18}_{-0.14}$	$2.4^{+0.3}_{-0.6}$	2.73	...	...	...	131.5/144	3.50	0.0207	
	apec	...	...	...	...	$4.1^{+4.0}_{-1.4}$	4.35	132.0/145	4.17	0.0242	



Table 6 — Continued

Name	Model <sup>a</sup>	$N_{\text{H}}$ ( $10^{22} \text{ cm}^{-2}$ )	$\Gamma^{\text{b}}$	$A_{\text{pl}}$	$A_{\text{ref}}$	$kT$ (keV)	$A_{\text{apec}}$	$C/\text{dof}$	$F_{2-10}$	$L_{2-10}$	X-ray class (12)
(1)	(2)	(3)	(4)	(5)	(6)	(7)	(8)	(9)	(10)	(11)	(12)
NGC 5132	apec+zpha(zpo+zga)* <sup>g</sup>	$0.14^{+0.29}_{-0.11}$	1.8f	1.16	...	$1.24^{+0.46}_{-0.34}$	0.731	119.4/142	4.88	0.0283	
	zpha(zpo)	$0.27^{+0.28}_{-0.16}$	$3.3^{+1.6}_{-0.9}$	3.12	...	...	...	75.5/102	1.20	0.0177	
	apec	...	...	...	...	3.4	3.54	87.3/103	...	...	
NGC 5350	apec+zpha(zpo)*	0.069 (< 0.30)	1.8f	0.931	...	$0.55^{+0.40}_{-0.23}$	0.329	75.6/101	3.10	0.0423	
	zpha(zpo)	0.23	3.8	2.61	...	...	...	144.2/142	...	...	
	apec	...	...	...	...	2.6	3.24	184.8/143	...	...	
2MASX J14341353+0209088	apec+zpha(zpo)*	0 (< 0.030)	1.8f	0.577	...	$0.62^{+0.17}_{-0.19}$	0.484	132.2/141	2.02	0.00269	
	zpha(zpo)	0.19 (< 0.55)	$3.4^{+2.3}_{-1.4}$	0.561	...	...	...	53.9/50	0.017	0.0280	
	apec	...	...	...	...	2.2	0.763	58.4/51	...	...	
2XMM J222942.7–204607	apec+zpha(zpo)*	0.069 (< 0.55)	1.8f	0.204	...	$0.25^{+0.29}_{-0.10}$	0.164	53.9/49	0.617	0.0894	
	pha(po)*	0 (< 1.3)	$1.7^{+1.4}_{-0.9}$	0.261	...	...	...	11.0/141	1.01	...	
	apec	...	...	...	...	5.4 (> 1.6)	0.875	11.1/142	1.04	...	
NGC 7617	zpha(zpo)	0.036 (< 0.23)	$2.8^{+1.3}_{-0.5}$	0.562	...	...	...	210.0/220	0.473	0.00210	
	apec	...	...	...	...	0.91	0.403	259.1/221	...	...	
	apec+zpha(zpo)*	0 (< 0.062)	1.8f	0.281	...	$0.30^{+0.11}_{-0.06}$	0.266	209.9/219	0.96	0.00416	

X-RAY AND IR SELECTION OF OBSCURED AGNS

**Note.** — Column 1: Galaxy Name; Column 2: Spectral Model; Column 3: Absorption column density; Column 4: Photon index of the power-law component; Column 5: Normalization of the power-law component in units of  $10^{-5}$  photons  $\text{cm}^{-2} \text{ s}^{-1}$  at 1 keV; Column 6: Normalization of the reflection component represented by the pexrav model in units of  $10^{-5}$  photons  $\text{cm}^{-2} \text{ s}^{-1}$  at 1 keV; Column 7: Temperature of the apec plasma model; Column 8: Normalization of the apec thermal plasma model in units of  $10^{-19}/(4\pi(D_{\text{A}}(1+z))^2/\int n_{\text{e}}n_{\text{H}}dV)$ , where  $D_{\text{A}}$  is the angular size distance to the source (cm),  $n_{\text{e}}$  is the electron density ( $\text{cm}^{-3}$ ), and  $n_{\text{H}}$  is the hydrogen density ( $\text{cm}^{-3}$ ); Column 9:  $C$  statistic/degree of freedom; Column 10: Observed flux in 2–10 keV in units of  $10^{-14}$  erg  $\text{cm}^{-2} \text{ s}^{-1}$ ; Column 11: Absorption-corrected luminosity in 2–10 keV in units of  $10^{42}$  erg  $\text{s}^{-1}$ ; Column 12: Classification of absorption for adopted spectral model. Thin: Compton-thin ( $N_{\text{H}} = 10^{22} - 1.5 \times 10^{24} \text{ cm}^{-2}$ ). Thick: Compton-thick ( $N_{\text{H}} > 1.5 \times 10^{24} \text{ cm}^{-2}$ ).

<sup>a</sup> pha: photoelectric absorption; po: power law; apec: thermal plasma emission model; ref: reflected emission from cold matter; ga: Gaussian. The first letter of z stands for emission/absorption at the source redshift. \* denotes the adopted model in Figures 15–17.

<sup>b</sup> “f” denotes fixed parameter.

<sup>c</sup> The effect of Compton scattering is approximately taken into account by using the cabs model in XSPEC. The column density is assumed to be same as that for photoelectric absorption.

<sup>d</sup> The absorption column density was not constrained and fixed at the best-fit value.

<sup>e</sup> Pegged at the upper bound allowed in the fit.

<sup>f</sup> Flux and luminosity are derived by extrapolating the result of fit using energies below 2 keV.

<sup>g</sup> Center energy of the Gaussian component is fixed at 6.97 keV.

**Table 7**  
Parameters of Fe-K Emission Line

Name	Model <sup>a</sup>	Line Center <sup>b</sup> (keV)	$A_{\text{Gauss}}$	EW (eV)	$\Delta C$
(1)	(2)	(3)	(4)	(5)	(6)
UGC 959/Mrk 991	apec+zpha(zoo)	6.4f	0.0(< 0.0958)	0 (< 430)	0.0
IRAS 01356–1307	...	...	...	...	...
2MASX J03084352+4051419	apec+pha(po+pha(po)) <sup>c</sup>	6.4f	0.025 (< 0.14)	50 (< 250)	0.1
IRAS 03152–4427	apec+zpha(zpo+zpha(zpo))	6.4f	0.026 (< 0.28)	47(< 360)	0.1
UGC 2730	apec+zpha(zpo)	6.4f	0.052 (< 016)	450 (< 1320)	1.2
2MASX J05052442–6734358	zpha(zpo+zpha(zpo+zga))	6.4f	2.1 <sup>+2.0</sup> <sub>-0.13</sub>	240 <sup>+120</sup> <sub>-140</sub>	8.8
2MASX J05430955–0829274	zpha(zpo+zga)	6.4f	0.14 <sup>+0.12</sup> <sub>-0.10</sub>	500 <sup>+480</sup> <sub>-350</sub>	7.2
ESO 205–IG003	apec+zpha(zpo+zpha(zpo+zga))	6.38 ± 0.05	0.49 ± 0.03	80 <sup>+38</sup> <sub>-37</sub>	12.8
NGC 2611	apec+zpha(zpo+zpha(zpo))	6.4f	0.853 (< 790)	200 (< 860)	0.4
SDSS J085312.35+162619.4	apec+zpha(zpo+zpha(zpo))	6.4f	0.110 <sup>+0.155</sup> <sub>-0.103</sub>	270 <sup>+390</sup> <sub>-250</sub>	3.2
CGCG 213–027	apec+zpha(zpo+zph(zpo))	6.4f	0.0 (< 0.130)	0 (< 250)	0.0
NGC 5037	apec+zpha(zpo+zpha(zpo))	6.4f	0.0 (< 0.12)	0 (< 140)	0.0
UGC 8621	apec+zpha(zpo+zpha(zpo))	6.4f	0.10 (< 0.42)	260 (< 570)	1.1
IRAS 13443+0802NE	apec+zpha(zpo+zpha(zpo))	6.4f	0.020 (< 0.055)	440 (< 1130)	2.3
NGC 5689	zpha(zpo+zpha(zpo))	6.4f	0.0580 (< 0.495)	84 (< 750)	0.1
IC 5264	apec+zpha(zpo)	6.4f	< 0.062	< 2290	0.3
NGC 7566	apec+zpha(zpo+zpha(zpo+zga))	6.4f	0.378 (< 1.43)	260 (< 540)	1.2
IRAS 00517+4556	pha(po+pha(po))	6.4f	0.0(< 0.057)	0 (< 420)	0.0
	pha(po+ref)	6.4f	0.0 (< 0.046)	0 (< 280)	0.0
NGC 1402	apec+zpha(zpo+zga)	6.380 <sup>+0.056</sup> <sub>-0.063</sub>	0.116 <sup>+0.091</sup> <sub>-0.064</sub>	4560 <sup>+3650</sup> <sub>-2580</sub>	18.7
2XMMi J052555.5-661038	...	...	...	...	...
2MASX J05391963–0726190	pha(po)	6.4f	0.042 <sup>+0.050</sup> <sub>-0.035</sub>	1370 <sup>+1620</sup> <sub>-1090</sub>	4.8
	pha(ref)	6.4f	0.029 (< 0.078)	460 (< 1250)	2.1
IC 614	apec+zpha(zpo+zpha(zpo+zga))	6.31 ± 0.053	0.51 <sup>+0.46</sup> <sub>-0.29</sub>	1500 <sup>+910</sup> <sub>-890</sub>	12.5
	apec+zpha(ref+zga)	6.31 <sup>+0.055</sup> <sub>-0.051</sub>	0.68 <sup>+0.31</sup> <sub>-0.22</sub>	1070 <sup>+1010</sup> <sub>-660</sub>	11.0
2MASX J11594382-2006579	apec+pha(ref)	6.4f	0 (< 0.051)	0 (< 500)	0.0
	apec+zpha(ref)	6.4f	0.0691 <sup>+0.064</sup> <sub>-0.112</sub>	740 <sup>+1200</sup> <sub>-680</sub>	3.0 <sup>d</sup>
2XMM J184540.6–630522	zpha(zpo+zga)	6.4f	0.24 <sup>+0.29</sup> <sub>-0.18</sub>	2370 <sup>+3080</sup> <sub>-1770</sub>	6.6
	zpha(zpo+ref+zga)	6.4f	0.22 <sup>+0.30</sup> <sub>-0.17</sub>	1660 <sup>+2310</sup> <sub>-1340</sub>	5.3
NGC 6926	apec+zpha(ref+zga)	6.415 <sup>+0.057</sup> <sub>-0.055</sub>	0.168	2690 <sup>+1340</sup> <sub>-1520</sub>	19.5
	apec+zpha(zpo+ref+zga)	6.415 <sup>+0.056</sup> <sub>-0.054</sub>	0.17 <sup>+0.12</sup> <sub>-0.09</sub>	3560 <sup>+3230</sup> <sub>-2030</sub>	21.3
2MASX J23404437-1151178	apec+zpha(zpo+zpha(zpo+zga))	6.4f <sup>d</sup>	0.106 <sup>+0.151</sup> <sub>-0.084</sub>	1410 <sup>+2030</sup> <sub>-1110</sub>	4.7
	apec+zpha(zpo+ref+zga)	6.4f <sup>d</sup>	0.031 <sup>+0.039</sup> <sub>-0.023</sub>	3020 <sup>+3810</sup> <sub>-2210</sub>	6.9
NGC 7738	apec+zpha(zpo+ref+zga)	6.434 ± 0.067	0.119 <sup>+0.134</sup> <sub>-0.080</sub>	3310 <sup>+4350</sup> <sub>-2250</sub>	9.4
NGC 35	apec+zpha(zpo)	6.4f	0.0234 (< 0.111)	2110 (< 10150)	0.9
2XMM J004330.4-180107	pha(po)	6.4f	0.0 (< 0.037)	0 (< 390)	0.0
UGC 587	...	...	...	...	...
2MASX J02253645–0500123	zpha(zpo)	6.4f	0.0014 (< 0.0591)	37 (< 1610)	0.0
A426[BM99]183	...	...	...	...	...
AKARI J0531228+120057	...	...	...	...	...
CXO J053513.5–690013	...	...	...	...	...
CXO J054532.6-001129	pha(po)	6.4f	0 (< 0.0104)	0 (< 300)	0.0
CGCG 009–061A	...	...	...	...	...
ESO 264–G032	...	...	...	...	...
MCG +01–27–029	...	...	...	...	...
UGC 06046	...	...	...	...	...
NGC 3953	...	...	...	...	...
NGC 4559A	...	...	...	...	...
NGC 4696B	...	...	...	...	...

Table 7 — Continued

Name	Model <sup>a</sup>	Line Center <sup>b</sup> (keV)	$A_{\text{Gauss}}$	EW (eV)	$\Delta C$
(1)	(2)	(3)	(4)	(5)	(6)
NGC 4713	apec+zpha(zpo+zga)	6.4f	$0.018^{+0.019}_{-0.014}$	$570^{+620}_{-440}$	5.3
IRAS 12596–1529	apez+zpha(zpo)	6.4f	$0.0359 (< 0.118)$	$810 (< 2710)$	1.6
	apez+zpha(zpo+zga)	6.97f	$0.076^{+0.029}_{-0.061}$	$2080^{+2940}_{-1680}$	5.5
NGC 5132	...	...	...	...	...
NGC 5350	...	...	...	...	...
2MASX J14341353+0209088	...	...	...	...	...
2XMM J222942.7–204607	pha(po)	6.4f	$< 0.053$	$< 6560$	0
NGC 7617	apec+zpha(zpo)	6.4f	$< 0.0279$	$< 2830$	0.9

**Note.** — Column 1: Galaxy Name; Column 2: Spectral Model used to derive the Fe-K line parameters; Column 3: Center energy of the Gaussian line; Column 4: Normalization of the Gaussian in units of  $10^{-5}$  photons  $\text{cm}^{-2} \text{s}^{-1}$  in the line; Column 5: Equivalent width; Column 6: The improvement in fit compared to the model without a Gaussian line.

<sup>a</sup> The description of model components is same as in Table 5. A photon index of 1.8 was assumed for the power-law component. “...” means that X-ray flux around Fe-K line is low and that no meaningful constraint on Fe-K line is obtained.

<sup>b</sup> “f” denotes fixed parameter.

<sup>c</sup> If a redshifted model is used and if the line center energy is assumed to be 6.4 keV, redshift is weakly constrained as  $0.046 \pm 0.066$  and the improvement of the fit is  $\Delta C = 5.6$ .

<sup>d</sup> The peak at 5.8 keV seen in the spectrum was assumed to be Fe-K line at 6.4 keV in the source rest frame and the best-fit redshift of  $z = 0.097$  was obtained.  $\Delta C$  was calculated by assuming the redshift determined from the model containing a Gaussian line.

**Table 8**  
Summary of Number of Objects

Sample	No.	X-ray	Unabsorbed	Thin	Thick	Absorbed Fraction
(1)	(2)	(3)	(4)	(5)	(6)	(7)
18+90	85	79 (93%)	6	44	29	92%
90	84	62 (74%)	31	21	10	50%
18	10	10 (100%)	1	7	2	90%
Total	179	151 (84%)	38	72	41	75%

**Note.** — Column 1: Infrared sample. 18+90 — 18 + 90  $\mu\text{m}$  sample, 18 — 18  $\mu\text{m}$  sample in Table 4; 90 — 90  $\mu\text{m}$  sample in Table 3. Column 2: Number of objects in the sample. Column 3: Number of objects with X-ray measurement of absorption. Fraction of objects with available X-ray absorption data is shown in parenthesis. Column 4: Number of unabsorbed objects with  $N_{\text{H}} < 10^{22} \text{ cm}^{-2}$ . Column 5: Number of objects absorbed by Compton-thin matter. Column 6: Number of objects absorbed by Compton-thick matter. Column 7: The fraction of objects absorbed by Compton-thin or Compton-thick matter in the sample.